A Unified Approach to Finite Element Simulation of Elastoviscoplastic Fluid Flows

Dissertation

zur Erlangung des akademischen Grades eines

Doktors der Naturwissenschaften

(Dr. rer. nat.)

Der Fakultät für Mathematik der

Technischen Universität Dortmund

vorgelegt von

Muhammad Tayyab Bin Saghir

im September 2025

Dissertation

A Unified Approach to Finite Element Simulation of Elastoviscoplastic Fluid Flows

Fakultät für Mathematik

Technische Universität Dortmund

Erstgutachter: Prof. Dr. Stefan Turek

Zweitgutachter: Privatdozent Dr. Andriy Sokolov

Tag der mündlichen Prüfung: 18.12.2025

Abstract

In this study, we present the development of a two-dimensional finite element solver for the simulation of fluids exhibiting both elastic and plastic constitutive properties. We achieve this by combining the constitutive models of the Oldroyd-B model for viscoelastic fluids and the Papanastasiou model for Bingham fluids within a single Eulerian numerical framework. Our aim within this approach is to approximate the given velocity, pressure, and elastic stresses. We employ a higher order finite element method for the velocity-stress approximation and a discontinuous pressure element. This specific element pair has proven highly effective for accurately capturing the behavior of both Oldroyd-B and Bingham fluids, including non-linear viscosity functions. Our study consists of three main steps. Firstly, we validate the numerical results for each module component of the constitutives to ensure the accuracy of the approximations and calculations. This step is crucial for establishing the reliability and robustness of our approach. Subsequently, in the second step, we apply the solver to simulate elastoviscoplastic fluid behavior in a porous medium and flow around a cylinder benchmark. Finally, we compute the drag and lift for the flow around the cylinder simulation to validate our numerical methodology against established benchmark results. Through the analysis of the above mentioned benchmark problems, we highlight the potential of the proposed solver to reliably capture the complex interplay of elastic, viscous, and plastic effects in non-Newtonian fluid dynamics.

Acknowledgements

I would like to extend my sincere gratitude to Prof. Dr. Stefan Turek for his excellent supervision and his encouragement and patience during my doctoral research. His deep understanding, wise advice and ongoing encouragement has provided me with endless inspiration encouragement. I am also thankful for my co-supervisor Dr. Hogenrich Damanik, whose invaluable advice and constant mentorship guided the work to its completion.

My gratitude also goes to Dr. Abderrahim Ouazzi Dr. Shafqat Hussain for his guidance, insightful discussions and kind suggestions that have significantly contributed to the completion and improvement of this thesis.

I am deeply grateful to my colleagues in LS-III for their support during my stay at TU Dortmund.

I would like to thank Deutscher Akademischer Austauschdienst (DAAD) for financially supporting this study. I am also grateful to the staff at TU Dortmund, especially Frau Drees, Frau Lamprecht, and Frau Strauch for their continuous support.

Muhammad Tayyab Bin Saghir
Dortmund, September 2025

Contents

List of Figures

List of Tables

Chapter 1

Introduction

This chapter presents the motivation for studying and numerically simulating non-Newtonian fluids, emphasizing their widespread occurrence and significance across various industries. The following section outlines key application areas of non-Newtonian and elastoviscoplastic fluids, including use as drag reduction agents in pipeline transport, in biomedical contexts such as blood flow modeling, in food processing where complex rheological behavior is common, and in the design of advanced personal protective equipment that incorporates shear thickening materials. These varied examples illustrate the significance and importance of developing efficient and reliable computational methods and simulation techniques for non-Newtonian flows.

1.1 Motivation

Fluids are everywhere, from the coffee we stir to the air we breathe, which makes their study very important. Naturally, they have been the center of research for many years. Newton described how common fluids behave and stated that they have constant viscosity under constant pressure and temperature. Hence, these types of liquids are called Newtonian fluids. Following his work, the behavior of Newtonian fluids has been extensively analyzed, and mathematical models have been developed. However, it has been realized by scientists in the recent decades that numerous materials of industrial importance such as foams, emulsions, suspensions, slurries

and foodstuff do not obey this law of viscosity (Newtonian law of viscosity). These are referred to as non-Newtonian or rheologically complex fluids. Unlike Newtonian fluids, non-Newtonian fluids do not have constant proportionality between the shear stress and the shear rate. Contrary to popular belief, non-Newtonian fluids are generally not unique, they are, in fact, more common than Newtonian fluids in nature and technology. Hence, a detailed knowledge of the behavior of non-Newtonian fluids is essential not only for the development of rheological theory but also to facilitate the design and optimization of new materials.

1.2 Applications

The following examples illustrate key applications of non-Newtonian and elastoviscoplastic fluids across various scientific and engineering domains.

1.2.1 Drag Reduction Agents in Pipeline Transport

One of the most well known and industrially significant applications of non-Newtonian fluids is the use of Drag Reducing Agents (DRAs) in pipeline transportation. DRAs are typically high molecular weight polymers, when introduced in very low concentrations, they can induce substantial reductions in turbulent frictional losses, a phenomenon first systematically studied by Toms in 1948, now commonly referred to as the Toms effect [5]. In crude oil pipelines, for example, the application of DRAs can lead to significant energy savings, reduced pumping costs, and increased pipeline capacity, especially over long distances. Figure 1.3 illustrates the impact of DRAs in reducing turbulent friction within pipelines by transitioning flow from a highly turbulent regime to a more streamlined one. The reduction in pressure drop from 100 bar to 40 bar shows the efficacy of high molecular weight polymers in suppressing turbulence and enhancing flow efficiency.

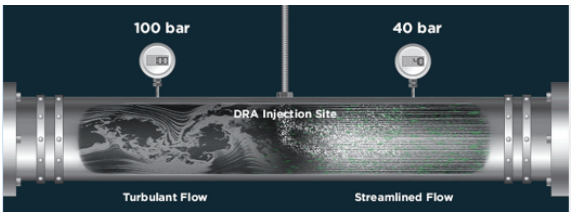

FIGURE 1.1: High molecular weight polymer drag reducing agents (DRAs) help suppress turbulence and improve flow efficiency in oil pipelines [1].

1.2.2 Automobile Transmissions

Automatic transmission fluids (ATFs) are essential for the performance and durability of modern automatic gearboxes, where they serve multiple functions, including lubrication, cooling, and hydraulic actuation. A critical aspect of ATF performance lies in its rheological behavior, especially under varying temperature and shear conditions. Unlike simple Newtonian fluids, many ATFs exhibit non-Newtonian characteristics, particularly shear thinning behavior, which is advantageous for reducing viscous drag at high shear rates while maintaining adequate film thickness at low shear. This shear dependent viscosity behavior contributes significantly to fuel efficiency by minimizing hydrodynamic losses in torque converters and gear assemblies. Furthermore, non-Newtonian behavior enhances the fluid's ability to sustain elastohydrodynamic lubrication (EHL) regimes, which are essential in high pressure contacts. Additive packages, including viscosity index improver and friction modifiers, are often engineered to tailor these non-Newtonian properties, thus enabling the fluid to meet the requirements of modern transmission systems [6]. Furthermore, non-Newtonian fluids improve clutch engagement smoothness by adjusting friction characteristics under dynamic loading, which is critical for drivability and transmission longevity. Temperature dependent non-Newtonian behavior also contributes to the thermal stability and performance consistency of the fluid. Therefore, understanding and controlling the non-Newtonian properties of ATFs is crucial in the design of high performance transmission systems.

1.2.3 Biomedical Science

Beyond engineering applications, non-Newtonian fluids play a pivotal role in the medical and biomedical sciences, where their complex rheological behavior supports critical physiological and technological functions. Blood itself is a classical example of a naturally occurring non-Newtonian fluid, exhibiting shear thinning characteristics that are vital for efficient perfusion in microcirculation [7]. Understanding its flow behavior is essential for accurate hemodynamic modeling, artificial organ design, and the development of cardiovascular devices. Moreover, engineered non-Newtonian fluids such as hydrogels and polymeric solutions are widely used in drug delivery systems, where their shear thinning or thixotropic properties enable injectability and sustained release at the target site [8]. In tissue engineering, viscoelastic bioinks facilitate cell encapsulation and 3D bio printing, supporting structural integrity during deposition [9]. Injectable viscoelastic agents mimicking synovial fluid are also used in treating osteoarthritis, improving joint lubrication and pain management [10]. Such biomedical applications highlight the necessity of understanding and modeling non-Newtonian behavior, as it directly impacts performance, biocompatibility, and therapeutic efficacy.

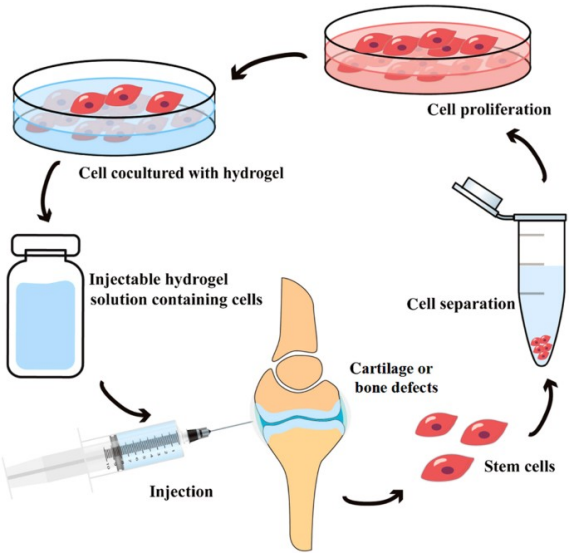

FIGURE 1.2: Schematic illustration of injectable hydrogels for cartilage and bone tissue engineering applications. [2].

1.2.4 Food Industry

Non-Newtonian fluids are of critical importance in the food processing industry, where many products, such as ketchup, mayonnaise, yogurt, and bread dough, exhibit complex rheological behaviors. These substances often exhibit shear thinning or viscoplastic and viscoelastic characteristics, which facilitate flow under stress while maintaining structural stability at rest. For example, the ability of ketchup to remain stable in the bottle and yet flow readily upon squeezing is a direct consequence of its non-Newtonian fluid behavior. From a food engineering perspective, accurate modeling of these non-Newtonian properties is essential for the design of a system that ensures food safety and its nutrients, mixing operations, extrusion processes, and quality control protocols. Effective handling and processing of such materials require a thorough understanding of their flow curves, yield stresses, and time dependent behaviors. Consequently, the knowledge of non-Newtonian rheology supports both the efficiency of manufacturing systems and the consistency of the final consumer product [11].

FIGURE 1.3: Illustration of the significance of elastic and plastic fluids in the food industry. [3].

1.2.5 Personal Protective Equipment

Liquid body armor represents the most advanced application of non-Newtonian fluids, specifically shear thickening fluids (STFs), which exhibit a drastic increase in viscosity when subjected to high strain rates or impact forces. These fluids are typically suspensions of solid particles in a carrier liquid, which remain flexible under normal conditions but rapidly solidify upon impact, providing enhanced protection against ballistic and blunt force trauma. When impregnated into textiles such as Kevlar, STFs significantly improve energy absorption and reduce material deformation without compromising wearability or flexibility. This dynamic stiffening mechanism enables the development of lightweight, flexible protective gear that combines comfort with high performance impact resistance, illustrating the practical exploitation of non-Newtonian rheology in defense technology [4].

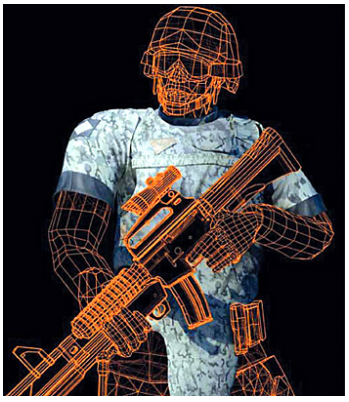

FIGURE 1.4: Liquid body armour contains 10 layers of Kevlar with thick fluid between each layer. When the bullet hits, the fluid solidifies and absorbs the impact over a wider range. [4].

1.2.6 Everyday Applications of Elastoviscoplastic Fluids

Elastoviscoplastic (EVP) materials spread through everyday life in foods, personal care products, household cleaners, coatings and inks, construction materials, energy-sector fluids, biomedical media, and geophysical settings, and they are engineered precisely because they combine an elastic response at small deformations, a finite yield stress that suppresses unwanted motion at rest, and a viscous flow (often shear thinning) once yielded. A compact constitutive description for the yielded regime

is the Herschel Bulkley relation, which is frequently coupled with an elastic contribution to capture pre-yield storage and recovery (e.g., Saramito type EVP laws) [12]. In the context of kitchen, ketchup, mayonnaise, sauces, chocolate, and yogurt are designed so that the Bingham number is large at rest (no drip); on squeezing, shaking, and spreading, the apparent viscosity collapses, elasticity contributes to mouthfeel and shape retention on the plate, while thixotropic rebuilding restores consistency after shear. In paints and coatings, elastoviscoplastic behavior helps in three practical ways. It reduces splashes during rolling or spraying. It keeps fresh paint from sliding down vertical walls. It lets the surface become smooth after you finish. Manufacturers add associative and microgel thickeners to reach this balance. These ingredients give the wet paint a gentle strength when it is not moving, so the film stays where you put it, and the edges of each stroke remain neat. When you move the brush or roller, the paint becomes easier to spread, so brush marks blend and the finish looks even. If the mix is too weak, the paint drips and sags. If it is too stiff, the brush texture stays and the surface looks bumpy. A tuned recipe avoids both problems. EVP rheology is used directly in construction materials, and it guides how we design and place them. Fresh cement, paste, mortar, and concrete behave like soft solids when stresses are small, and they only start to flow once a yield stress is exceeded, which helps the mix hold its shape when it is not being worked. While the mix rests, its internal structure rebuilds, which is thixotropy, and this slow growth of static strength controls how easily the material can be pumped and how smoothly it can be finished. A small elastic response over short times helps a newly placed layer resist deformation and keeps edges from slumping. In sprayed concrete and tile adhesives, the recipe is adjusted to have a higher yield stress, so the material applied to the walls does not slide down. In self-compacting mixes, the recipe is adjusted to have a lower yield stress and a lower apparent viscosity, so the material spreads under its own weight into formwork without vibration. In large format three-dimensional printing, the material is formulated so that it flows easily inside the nozzle, which reduces printing forces and then quickly regains strength and stiffness after deposition, which prevents the printed layers from collapsing.

1.3 Contribution to the Thesis

This thesis presents significant advancements in the numerical modeling and simulation of elastoviscoplastic (EVP) fluid flows by addressing key challenges in solver robustness, constitutive modeling, and benchmark validation. The primary contributions are structured around three major themes.

First, the thesis contributes to the selection and implementation of a suitable material model that accurately captures the complex behavior of EVP fluids. Saramito's [12] work has been influential in providing a clearer framework for studying the behavior of such complex fluids. In modeling such types of equations, the numerical variables depend on the choice of constitutive models. Many of these constitutive models involve different numerical frameworks to handle the transition between the solid and liquid phases, such as the Saramito model. Although these strategies offer improved accuracy, the numerical treatment becomes significantly more complex, primarily due to the challenges of identifying the interface between the two phases [13]. To address these complexities, we propose a similar approach from Chaparian et al [13, 14]. In our work, we combine the constitutive models of the Oldroyd-B, which has been used as a benchmark for many different numerical techniques [15], and the Papanastasiou regularized model [16] for Bingham fluids within a single Eulerian numerical framework. This strategy, which has recently gained attention in elastoviscoplasticity studies, has demonstrated promising qualitative results. The Papanastasiou regularization smooths the discontinuity at the yield surface, facilitating numerical differentiation and convergence in Newton methods. The Oldroyd-B model accounts for the elastic memory effects typical of polymeric fluids. The combination allows for modeling both unyielded zones and elastic phenomena within a unified framework. The model is shown to be physically consistent and numerically stable over a wide range of Bingham and Weissenberg numbers.

Secondly, a robust numerical solver has been developed specifically for EVP simulations. The solver integrates a Newton damped method for non-linear iteration, which is particularly effective in handling strong nonlinearities near yield surfaces and under high Weissenberg numbers. To solve the resulting linearized system, a direct sparse solver based on the Unsymmetric MultiFrontal method, and when there

is a memory constraint, using the Unsymmetric MultiFrontal Package (UMFPACK), we employ a multigrid iterative solver. The specific framework ensures fast convergence and scalability, making it suitable for high resolution simulations in two and three dimensions. This solver offers substantial improvements in terms of numerical stability and computational efficiency compared to standard approaches.

Finally, the developed framework is validated through detailed numerical benchmarking. In particular, the flow around a circular cylinder is investigated as a benchmark problem. Simulations are performed across a range of Bingham and Weissenberg numbers, and results include the computation of drag and lift coefficients, as well as detailed flow analysis. Where available, comparisons are made with results from the literature for Newtonian and viscoelastic cases. Additionally, the thesis establishes new benchmark results for EVP fluids in configurations where prior reference data do not exist, thereby contributing to the field by providing verified computational data for future model validation.

Overall, this work contributes to both the numerical methods and physical modeling communities by providing a unified and validated approach to simulating complex elastoviscoplastic flows with practical relevance in industrial and geophysical applications.

1.4 Structure of the Thesis

The present thesis is organized systematically to address the fundamental aspects, numerical challenges, and solutions for non-Newtonian fluids. Each chapter builds upon the theoretical framework and computational analyses to provide a comprehensive understanding of the subject. The following section outlines the structure of the thesis and summarizes the focus and content of each chapter.

Chapter 2 presents a systematic overview of fundamental rheological models describing viscoelastic, viscoplastic, and elastoviscoplastic (EVP) fluids, emphasizing their mathematical formulations and computational challenges. The discussion begins with viscoelastic fluids, highlighting the importance of frame-indifferent constitutive equations to ensure physical objectivity under rigid body motions. The chapter then

addresses viscoplastic fluids, characterized by a yield stress that separates solid-like and fluid-like behavior. Challenges arising from the singularity at the yield surface are tackled using regularization methods such as the Papanastasiou method. Finally, a unified elastoviscoplastic framework is developed, integrating viscoelastic and viscoplastic effects while maintaining material objectivity.

Chapter 3 presents the finite element methodology used to solve the governing equations. It begins with a review of FEM function spaces and illustrates the method through the advection-diffusion equation, introducing key concepts such as trial and test space selection, discretization, and stabilization. The chapter then covers mesh generation, element shape functions, and numerical integration via Gaussian quadrature for an accurate evaluation of stiffness matrices and load vectors, followed by matrix assembly. The finite element formulation is subsequently applied to the governing equations, with particular focus on the mixed formulation required for incompressible flows. The Babuska–Brezzi (inf-sup) condition is discussed in detail, and finally, stabilization techniques are also discussed.

Chapter 4 develops the numerical solver infrastructure for the non-linear algebraic systems resulting from the finite element discretization of the elastoviscoplastic (EVP) equations. The main non-linear solver employed is the damped Newton method, chosen for its robustness and improved convergence in strongly non-linear regimes, which is discussed in detail. UMFPACK and multigrid techniques are also discussed, and the behavior of the solver is examined by performing numerical simulations for the Newtonian and the non-Newtonian cases.

Chapter 5 presents a comprehensive numerical validation of the elastoviscoplastic (EVP) framework through benchmark problems that cover various rheological behaviors. The validation begins with the classical case of Bingham viscoplastic flow in a channel, where the numerical solution is compared with the exact analytical solution available for fully developed unidirectional flow. This case serves to verify surface capture yield and to evaluate the influence of the Papanastasiou regularization parameter on the accuracy and smoothness of the solution. Next, the viscoelastic flow around a confined cylinder is simulated to assess the solver performance. The complete EVP model is then tested in porous media, examining yield stress, permeability, and viscoelastic hysteresis. Finally, all fluid models are evaluated in

flow around the cylinder to calculate drag and lift for various Reynolds and Weissenberg numbers. These benchmarks demonstrate the accuracy and robustness of the solver.

Chapter 6 concludes the thesis by summarizing the development and validation of a robust finite element framework for simulating elastoviscoplastic (EVP) fluids. The proposed constitutive model successfully integrates viscoelastic and viscoplastic effects within a thermodynamically consistent formulation. Numerical challenges were addressed through regularization techniques and solver strategies. A consistent FEM discretization and Newton non-linear solver ensured stability and convergence. Benchmark validations across Bingham, viscoelastic, and EVP flows showed accuracy and physical fidelity. There is a discussion about the framework presented, which is versatile and extendable to complex geometry flows. Future work may include 3D simulations, and coupling with thermal effects is discussed.

Chapter 2

Mathematical Modeling of Elastic and Plastic Fluids

2.1 Introduction

The primary goal of this section is to illustrate the historical and mathematical background, as well as the difficulties arising in modeling and depicting the true physical behavior of a complex fluid. In this work, by complex fluid, we mean a fluid that exhibits elastic, viscous, and plastic properties. This type of fluid, in computational rheology (CR), is commonly known as elastoviscoplastic (EVP) fluid, which acts as a subset of complex fluids. In the computational rheology (CR) literature, it is also referred to as viscoelastoplastic fluids [13]. The EVP fluids exhibit elastic solid behavior under low stress conditions, reversibly storing energy. Beyond a certain yield stress, they flow like viscous fluids, and in some cases, exhibit irreversible plastic deformation [17, 18]. The most common example is bread dough. To make bread, you first need to knead the dough. The bread dough experiences the flow under your hand as you knead it; however, when you shape it, it maintains its shape. At this stage, if you gently press your fingertip into the dough, it does not spring back, but if you keep kneading the dough for a long time, it will then acquire some elastic properties, and then by doing the poke test, it will spring back quickly, acting more like an elastic material. This dough is not simply a viscoplastic or viscoelastic material but rather elastoviscoplastic material because it

exhibits viscoplasticity as well as a high degree of elasticity due to the elastic recovery upon the removal of deformation stress. This unique combination and behaviors within the EVP fluids make it particularly challenging to model the ideal constitutive equation that exhibits the true properties of such kinds of materials and makes them computationally manageable. The fulfillment of a perfect constitutive model is often impossible. The main components of EVP are viscoelasticity, an important fluid property in the complicated rheological behavior of many synthetic and natural fluids, and yield stress (σ_y), a critical parameter in EVP models, which has been characterized using various criteria, such as von-Mises criteria [19]. These criteria define the stress threshold at which plastic flow begins and are essential for accurately predicting the behavior of EVP fluids under different loading conditions. However, to obtain an estimate of the behavior of yield stress and elasticity in materials, several assumptions have been made in the construction of simple constitutive equations. Mathematical modeling of elastic and plastic fluids involves solving coupled systems of equations that describe the conservation of mass and momentum, along with constitutive equations for stress. These equations are inherently non-linear and often require advanced numerical techniques to solve them. Early models emphasized simplicity and computational efficiency, often at the expense of accuracy. Modern approaches aim to capture the full complexity of EVP behavior by incorporating detailed descriptions of microstructural dynamics [20].

In 1900, Schwedoff [21] introduced a model which is a plastic viscoelastic version (1D) of the Maxwell model while researching a gelatin solution, which marked the beginning of the creation of complex fluid based on yield stress. Similarly, the concept of fluids exhibiting plastic behavior, known as viscoplastic fluids, was also introduced by Bingham in 1922. These fluids are also referred to as Bingham fluids [17]. The so called yield stress, represented by σ_y, which controls the change from a solid-like to a liquid-like response, is evident in the rheology of viscoplastic fluids. Within stagnation areas, the material resists plastic deformation via microstructural elasticity, causing velocity gradients to disappear. In efforts to model such complex fluids, many researchers have presented different constitutive equations. The Herschel Bulkley model [18] extended this concept by incorporating power-law behavior to account for shear-thinning or shear-thickening effects, offering greater flexibility in describing diverse materials. Viscoelastic behavior in complex fluids was first

addressed by Oldroyd [22], who introduced differential constitutive equations to represent the interplay between elastic and viscous responses. The Oldroyd-B model became a backbone in viscoelastic fluid modeling, describing materials that exhibit stress relaxation and normal stress differences under shear. Building on this work, models such as the Maxwell and Kelvin-Voigt models were developed to capture different aspects of viscoelasticity. However, keeping in mind that many complex fluids exhibit elastisity as well as plasticity, these models did not account for all the features present in complex fluids, hence limiting their applicability to EVP fluids.

The development of EVP fluid models has been driven by both theoretical advancements and experimental observations. For example, particle based models describe the interactions between individual particles or polymer chains, providing insights into the mechanisms underlying EVP behavior. These models often leverage experimental data, such as rheological measurements, to validate their predictions and refine their parameters. Recognizing the need to combine viscoelastic and plastic behaviors, some of the researchers developed unified models that incorporate elements of elasticity, viscosity, and plasticity. Saramito [23] in 2007 proposed a constitutive model based on the unification of the Bingham viscoplastic [24] and the Oldroyd viscoelastic models [22]. This model has a strong mathematical base in such a way that it obeys the second law of thermodynamics. The model initially exhibits a Kelvin-Voigt viscoelastic response (equivalent to an ideal Hookean solid) before yielding. When the strain energy exceeds a critical threshold for yield stress, which is defined by the von Mises criterion, the material yields, and the stress field transitions to a non-linear viscoelastic constitutive law. This framework was later improved by the same author in [18] by introducing the Herschel–Bulkley viscoplastic model with power law index n to account for the shear-thinning behavior of the shear viscosity, and also for the smoothness of the plasticity criterion, and it is then combined with the Oldroyd model. This model also obeys the second law of thermodynamics, hence laying the strong foundation for that model. The author claimed that when $0 < n < 1$ the model indicates finite extensional properties and a shear thinning behavior. Beyond predicting the yield stress, this model also predicts the first normal stress difference effects in simple shear flows through its combined viscoelastic viscoplastic formulation.

De Souza Mendes in 2007 [25] proposed a mathematical model for elastoviscoplastic fluids. He worked on the modification of the classical version of the Oldroyd-B model, where the constant parameters,i.e., the relaxation time, retardation time, and viscosity, are replaced with the deformation rate. For unyielded material in the zero-shear-rate limit, the model converges to the classical Oldroyd-B formulation. Benito in 2008 [26] proposed another model based on a fully tensorial and rheological constitutive equation for elastoviscoplastic fluids. This framework describes a pre-yield regime in which the model behaves as a viscoelastic solid with substantial deformability, and a post-yield regime in which the model behaves as a viscoelastic fluid. The formulation also guarantees positive energy dissipation, satisfying the second law of thermodynamics.

In 2010 Park & Liu [27] introduced a model known as "The Park and Liu (PL) regularized model". The focus of the researchers was to introduce an elastoviscoplastic model based on regularization. They did some studies to avoid the singularity of discontinuity arising from viscoplastic models, and as the yield condition arises, a very straightforward approximation has been proposed by introducing the regularized model. The common regularization models in computational rheology are the Papanastasiou [16] and the Bercovier and Engleman [28]. In this work, they coupled a regularized Bingham model with the Maxwell constitutive equation by considering that both the viscosity, η, and the relaxation time, λ, of the material depend on the rate of deformation induced by the imposed flow field. More specifically, they assumed that when the material is unyielded, very small deformation occurs, while when it flows, it behaves as a viscoelastic Maxwell fluid. [29]

In 2010, Fawzi Belblidia et al. [13] presented a model based on the introduction of Papanastasiou regularized model [16] that generates the viscoplastic function with exponential stress growth, helping to remove the discontinuity present in the Bingham model. He introduced this regularized function by modifying the viscous part in the momentum equation. He then combined the regularized model with the Oldroyd B model. In his work, he uses the Papanastasiou model by modifying the viscous part in the momentum equation. He performed the simulations for 4:1:4 contraction expansion flow and claimed that these simulations explore the viscoplastic regime, via the Bingham Papanastasiou model, and extend this into the viscoelastoplastic regime through the Papanastasiou Oldroyd model.

Despite significant progress, several challenges remain in the mathematical modeling of EVP fluids. Accurately representing the yield surface in three-dimensional flows, accounting for temperature dependent properties, and integrating microstructural dynamics into macroscopic models are active areas of research. Advances in computational power and experimental techniques, such as rheometry and imaging, continue to drive innovation in this field. Additionally, the development of robust numerical methods for solving the highly non-linear equations governing EVP behavior remains a critical area of focus. Future research directions include the development of hybrid models that combine phenomenological and microstructural approaches. These efforts aim to improve the accuracy and predictive capability of EVP fluid models, enabling their application to a wider range of scientific and engineering problems. For instance, integrating data driven approaches with traditional modeling frameworks could provide new insights into the behavior of EVP fluids under complex loading conditions. From the literature review, it is evident that the formation of a constitutive model presenting EVP fluids often requires the combination of elastic and plastic models, and understanding these models is key to the rheology of complex fluids. The following section presents a detailed overview of elastic and plastic models.

2.2 Viscoelastic Models

2.2.1 Maxwell and Kelvin Voigt Element

In the rheology of complex fluids, springs and dashpots are often used as mechanical analogs to represent how real materials respond to stress and deformation over time. These elements help capture the combined elastic and viscous behavior of complex materials and many non-Newtonian fluids like elastoviscoplastic fluids. These are known as rheological models or mechanical models. A model of linear viscoelasticity can be built by considering the combinations of a linear elastic spring and a linear viscous dashpot. A spring and dashpot in series is called a Maxwell element (see Figure 2.2). E is the spring constant, γ_1 is the displacement of the spring and the force ($\boldsymbol{\sigma}_1$) in the spring is represented by the expression $\boldsymbol{\sigma}_1 = E\gamma_1$. The force $\boldsymbol{\sigma}_2$ in the dashpot is given by $\boldsymbol{\sigma}_2 = \eta\dot{\gamma}_2$, where η is the viscosity and $\dot{\gamma}_2$ is the rate of change

in displacement. Since they are in series, we have $\boldsymbol{\sigma}_1 = \boldsymbol{\sigma}_2 = \boldsymbol{\sigma}$. Alternatively, we can also claim that

$$\gamma = \gamma_1 + \gamma_2. \tag{2.1}$$

By eliminating γ_1 and γ_2 the maxwell model reads:

$$\boldsymbol{\sigma} + \frac{\eta}{E}\dot{\boldsymbol{\sigma}} = \eta\dot{\gamma}. \tag{2.2}$$

A Kelvin Voigt model is represented with a dashpot and a spring in a parallel arrangement, as shown in Figure 2.1. The forces in the elastic and viscous elements are represented by $\boldsymbol{\sigma}_1 = E\gamma$ and $\boldsymbol{\sigma}_2 = \eta\dot{\gamma}$ respectively, and mathematically, by parallel arrangement, the forces are summed up

$$\boldsymbol{\sigma} = E\gamma + \eta\dot{\gamma}. \tag{2.3}$$

This element is instantaneously viscous because, by design, the deformation γ and the rate of deformation $\dot{\gamma}$ of the spring and dashpot occur simultaneously. The dashpot must work in every deformation. If a constant force is applied, the deformation will be damped by viscosity, and the system will come to equilibrium with $\boldsymbol{\sigma} = E\gamma$, as in an elastic body. The Voigt model is suitable for viscoelastic solids and not for fluids. Visually, we can convince ourselves that the Maxwell element cannot withstand applied stresses without deforming. However, the Kelvin-Voigt model can do so. The Maxwell model thus describes a fluid, while the Kelvin–Voigt model describes a solid [30].

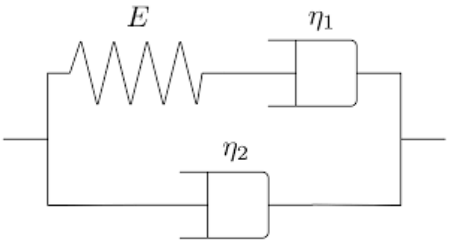

FIGURE 2.1: Kelvin-Voigt element.

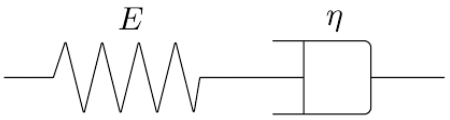

FIGURE 2.2: Maxwell element.

2.2.2 Material Objectivity and Oldroyd Model

Material objectivity, or the principle of material frame indifference, states that the constitutive equations that represent the behavior of a material must remain invariant under changes of the observer. This idea applies to any moving frames, not just Galilean frames, that is, frames that move with a constant translation. In the sense that we do not expect stresses to occur in a body just by running around it [12]. The constitutive equation is then considered objective as it remains constant. This concept is important to draw a meaningful result from the constitutive equation [31]. In 1950, Oldroyd [22] presented a model for fluids exhibiting elastic and viscous properties, which adheres to the principle of material frame indifference. Oldroyd [22] argued that time derivatives must be evaluated in a frame moving (translation, rotation, deformation) with the material, and by moving, he included translation, rotation, and (unusually) deformation. This leads to the upper and lower convected time derivatives. According to this theory, stresses in a continuous medium should only result from deformations and shouldn't alter when the material is merely rotated. Consider a given motion where a particle initially at point ξ has a position represented by Equation (2.4) and another where the same particle at the position represented by Equation (2.5) [32].

$$\boldsymbol{x}(\xi, t), \tag{2.4}$$

$$\boldsymbol{x}^*(\xi, t) = \boldsymbol{Q}(t)\boldsymbol{x}(\xi, t). \tag{2.5}$$

In Equation (2.5) $\boldsymbol{Q}$ represents a rotation. The stress tensor in the first case and second motion can be seen in Equation (2.6) and Equation (2.7) respectively.

$$\boldsymbol{T}(\boldsymbol{x}, t), \tag{2.6}$$

$$\boldsymbol{T}^*(\boldsymbol{x}^*, t) = \boldsymbol{Q}(t)\boldsymbol{T}(\boldsymbol{x}, t)\boldsymbol{Q}^{-1}(t). \tag{2.7}$$

Oldroyd extends the classical linear Jeffreys model [33] to the non-linear case. The Jeffreys model establishes a constitutive relation between the stress tensor and the velocity gradient of the fluid. Mathematically, the linear Jefferey model can be written as

$$\boldsymbol{T} + \lambda_1 \frac{\partial \boldsymbol{T}}{\partial t} = 2\eta \left(\boldsymbol{D} + \lambda_2 \frac{\partial \boldsymbol{D}}{\partial t} \right), \tag{2.8}$$

where η is the viscosity, λ_1 and λ_2 are the relaxation time and the retardation time, respectively. $\boldsymbol{D}(\boldsymbol{u}) = 1/2(\nabla \boldsymbol{u} + (\nabla \boldsymbol{u})^T)$, where $\boldsymbol{u}$ represents the velocity. Here, an easy approach is to replace the time derivative term $\partial/\partial t$ with the material time derivative $d/dt = \partial/\partial t + (\boldsymbol{u} \cdot \nabla)$, which represents the rate of change following a fluid particle. However, this substitution is wrong. To witness this, let us consider how the various terms in Equation (2.8) change under a superimposed rotation. We have

$$\frac{\partial \boldsymbol{x}(\xi, t)}{\partial t} = \boldsymbol{u}(\boldsymbol{x}, t), \tag{2.9}$$

$$\begin{aligned} \frac{\partial \boldsymbol{x}^*(\xi, t)}{\partial t} &= \boldsymbol{u}^*(\boldsymbol{x}^*, t) = \mathbf{Q}(t)\boldsymbol{u}(\boldsymbol{x}, t) + \dot{\mathbf{Q}}(t)\boldsymbol{x} \\ &= \mathbf{Q}(t)\boldsymbol{u}(\mathbf{Q}^{-1}(t)\boldsymbol{x}^*, t) + \dot{\mathbf{Q}}(t)\mathbf{Q}^{-1}(t)\boldsymbol{x}^*, \end{aligned} \tag{2.10}$$

as a result, we obtain

$$\nabla^* \boldsymbol{u}(\boldsymbol{x}^*, t) = \boldsymbol{Q}(t)\nabla \boldsymbol{u}(\boldsymbol{x}, t)\boldsymbol{Q}^{-1}(t) + \dot{\boldsymbol{Q}}(t)\mathbf{Q}^{-1}(t), \tag{2.11}$$

the second term on the right-hand side is antisymmetric, it follows that the symmetric part of the velocity gradient satisfies

$$\boldsymbol{D}^*(\boldsymbol{x}^*, t) = \boldsymbol{Q}(t)\boldsymbol{D}(\boldsymbol{x}, t)\boldsymbol{Q}^{-1}(t). \tag{2.12}$$

This property shows that the constitutive equation for a Newtonian fluid is consistent with the principle of material frame indifference. Now, however, consider the behavior of a material time derivative. If

$$\boldsymbol{T}^*(\boldsymbol{x}^*, t) = \boldsymbol{Q}(t)\boldsymbol{T}(\boldsymbol{x}, t)\boldsymbol{Q}^{-1}(t), \tag{2.13}$$

we find

$$\frac{d}{dt}\boldsymbol{T}^*(\boldsymbol{x}^*,t) = \mathbf{Q}(t)\frac{d\boldsymbol{T}(\boldsymbol{x},t)}{dt}\mathbf{Q}^{-1}(t) + \dot{\mathbf{Q}}(t)\mathbf{Q}^{-1}(t)\boldsymbol{T}^*(\boldsymbol{x}^*,t) - \boldsymbol{T}^*(\boldsymbol{x}^*,t)\dot{\mathbf{Q}}(t)\mathbf{Q}^{-1}(t), \tag{2.14}$$

which is not $\mathbf{Q}\frac{d\boldsymbol{T}}{dt}\mathbf{Q}^{-1}$. Oldroyd's, in his paper, suggested fixing this. We can replace Equation (2.8) by

$$\boldsymbol{T} + \lambda_1\frac{\mathcal{D}\boldsymbol{T}}{\mathcal{D}t} = 2\eta\left(\mathbf{D} + \lambda_2\frac{\mathcal{D}\mathbf{D}}{\mathcal{D}t}\right), \tag{2.15}$$

where either

$$\frac{\mathcal{D}\boldsymbol{T}}{\mathcal{D}t} = \frac{\partial\boldsymbol{T}}{\partial t} + (\boldsymbol{u}\cdot\nabla)\boldsymbol{T} + (\nabla\boldsymbol{u})^T\boldsymbol{T} + \boldsymbol{T}(\nabla\boldsymbol{u}), \tag{2.16}$$

or

$$\frac{\mathcal{D}\boldsymbol{T}}{\mathcal{D}t} = \frac{\partial\boldsymbol{T}}{\partial t} + (\boldsymbol{u}\cdot\nabla)\boldsymbol{T} - (\nabla\boldsymbol{u})\boldsymbol{T} - \boldsymbol{T}(\nabla\boldsymbol{u})^T. \tag{2.17}$$

The above two models are know as A and B model respectively. However, the question arises of how to make a selection between the Oldroyd A and Oldroyd B models. Oldroyd commented that it depends on the physics of the flow. At the end of his paper, Oldroyd calculated the flow around a rotating rod, where he found the Oldroyd B model would climb the rod, as Weissenberg had observed, whereas the Oldroyd A model would descend, which had not been observed. Hence the Oldroyd B is to be favored [34, 35].

Observe that, Equation (2.15) can be written as

$$\boldsymbol{T} = \boldsymbol{T}_p + \boldsymbol{T}_s, \tag{2.18}$$

where

$$\boldsymbol{T}_p + \lambda_1\frac{\mathcal{D}\boldsymbol{T}_p}{\mathcal{D}t} = 2\eta_p\mathbf{D}, \quad \eta_p = \left(1 - \frac{\lambda_2}{\lambda_1}\right)\eta, \tag{2.19}$$

and

$$\boldsymbol{T}_s = 2\eta_s\mathbf{D}, \quad \eta_s = \left(\frac{\lambda_2}{\lambda_1}\right)\eta. \tag{2.20}$$

The model is physically valid only if $\lambda_2 \leq \lambda_1$. η_p and η_s present polymer and solvent viscosity respectively. In the practical application of the model, however, η_s is often much larger than the viscosity of the solvent, except for very viscous

solvents (polymeric fluids typically have more than one relaxation time, and the contribution of shorter relaxation times to the viscosity usually exceeds that of the solvent). The limiting case $\lambda_2 = 0$ (i.e., $\eta_s = 0$) of the Oldroyd B model is called the upper convected Maxwell model. In the language of tensor analysis, the derivative appearing in the Oldroyd A model is called covariant or lower convected, while that in the Oldroyd B model is called contravariant or upper convected [32].

2.2.3 FENE-P and Giesekus Model

The FENE-P model is based on the finitely extensible non–linear elastic dumbbell for polymeric materials. The equation is derived from a kinetic theory, where a polymer chain is represented as a dumbbell consisting of two beads connected by an entropic spring. Other basic rheological models, such as the Maxwell model and Oldroyd-B model, take the elastic force between the beads to be proportional to the separation between the beads. The main disadvantage of such models is that the dumbbell can be stretched indefinitely, leading to divergent behavior and associated numerical instabilities in strong extensional flows. These problems are prevented by using a finitely extensible spring [36]. The Giesekus model is a phenomenological model based on the idea that polymer segments experience anisotropic friction. It includes a mobility factor that introduces nonlinearity, allowing the model to describe shear thinning and elastic behavior more realistically in viscoelastic fluids. The mathematical representation of both models can be seen in Section 2.4.1. Both models are widely used in computational fluid dynamics to simulate complex flow phenomena such as elastic instabilities and drag reduction in polymeric fluids.

2.2.4 The Deborah and Weissenberg Numbers

The behavior of viscoelastic fluids is governed by the interplay between elastic and viscous effects. Two dimensionless numbers, the Deborah number (Di) and the Weissenberg number (Wi), are fundamental in characterizing these effects. These numbers provide a quantitative measure of the relative importance of elasticity and viscosity in a given flow, enabling researchers to predict and analyze complex fluid behavior. The Deborah number is defined as the ratio of the material's relaxation

time (λ) to the characteristic timescale of the flow (T)

$$Di = \frac{\lambda}{T}. \tag{2.21}$$

Here, λ represents the time it takes for the material to relax toward its equilibrium state after a deformation, while T is the timescale over which the flow conditions change. The Deborah number distinguishes between fluid-like and solid-like behavior. When $Di \ll 1$, the material behaves as a viscous fluid, as the flow timescale is much longer than the relaxation time, and elastic effects are negligible. When $Di \gg 1$, the material behaves as an elastic solid, as the flow timescale is much shorter than the relaxation time, allowing elastic effects to dominate. When $Di \approx 1$, both elastic and viscous effects are significant, and the material exhibits viscoelastic behavior.

In steady or slowly varying flows, such as fully developed duct flows, the characteristic timescale T is effectively infinite, resulting in $Di = 0$. This implies that the Deborah number alone is insufficient to fully characterize viscoelastic effects in such flows [37].

The Weissenberg number, named after Karl Weissenberg, who pioneered the study of viscoelastic fluids, is defined as the ratio of elastic forces to viscous forces in a flow. It is given by

$$Wi = \frac{\lambda U}{L}, \tag{2.22}$$

where U is a characteristic velocity of the flow, and L is a characteristic length scale. While both the Deborah and Weissenberg numbers characterize the relative importance of elastic effects, they emphasize different aspects of the flow. The Deborah number focuses on the timescales of the material response and the flow, making it particularly useful for understanding transient or time-dependent behavior. The Weissenberg number focuses on the stresses generated in the flow, making it particularly useful for understanding steady-state or spatially varying flows. In many flows, the two numbers are related. For example, in a flow with a characteristic velocity U and length scale L, the characteristic timescale T can be approximated as $T = L/U$. Substituting this into the definition of De gives:

$$Di = \frac{\lambda}{T} = \frac{\lambda U}{L} = Wi. \tag{2.23}$$

Thus, in flows where $T = L/U$, the Deborah and Weissenberg numbers are equivalent. However, this is not always the case, and the choice of which number to use depends on the specific flow and the aspect of viscoelasticity being studied [38]. The Deborah and Weissenberg numbers have significant practical implications for the design and analysis of viscoelastic flows.

Low Di and Wi: In the regime of small values of both Di and Wi, the viscous effects become dominant, and the material acts like a Newtonian fluid. Elastic effects are assumed to be small, and the flow is treated by classical fluid mechanics.

Intermediate Di and Wi: In sufficiently large flows (, where Di and Wi are of order unity), elastic and viscous effects both become important and the material behaves as a complex viscoelastic material (shear thinning, normal stresses), and the flow of the fluid is going to be more complex than that of a simple Newtonian fluid.

High Di and Wi: In the limit of high values of both Di and Wi, we have elastic effects as the dominating ones, and the material shows a strong viscoelastic behavior, in which rod climbing (Weissenberg effect) is one of the examples. This frequently resulted in the creation of boundary layers, stress concentrations, and numerical issues in simulations. These effects are more tricky when poking close to geometry singularities and solid walls, and simulation may destabilise or not converge in such cases. [39]

2.3 Viscoplastic Model

As discussed, our study employs a model to simulate elastoviscoplastic fluids, which combines the Papanastasiou regularized model for Bingham fluids [16] with the Oldroyd-B model [40]. To gain insight from the Papanastasiou model, it's worth examining its fundamentals. Bingham originally introduced the constitutive equation that characterizes viscoplasticity [17]. The Bingham fluid states that below a certain yield stress, there will be no flow, and once that shear yield stress has been exceeded, you observe a flow. Mathematically, a Bingham viscoplastic fluid can be

defined as follows:

$$\begin{cases} \boldsymbol{D}(\boldsymbol{u}) = \mathbf{0}, & \sigma \leq \sigma_y \\ \boldsymbol{\sigma} = \left(\dfrac{\sigma_y}{\mathbf{II}(\boldsymbol{D})} + \eta_p \right) \boldsymbol{D}(\boldsymbol{u}), & \sigma > \sigma_y, \end{cases} \tag{2.24}$$

where η_p represents the plastic viscosity. The second invariant of the deformation tensor is defined as

$$\mathbf{II}(\boldsymbol{D}) = \sqrt{\boldsymbol{D} : \boldsymbol{D}}. \tag{2.25}$$

The deviatoric part of $\boldsymbol{\sigma}$ is defined as

$$\boldsymbol{\sigma}_d = \boldsymbol{\sigma} - \frac{1}{N} \operatorname{tr}(\boldsymbol{\sigma})\, \mathbf{I}, \tag{2.26}$$

N is the spatial dimesnion and $\boldsymbol{I}$ is the identity matrix. The abrupt transition in Equation (2.24) creates two distinct zones discussed below. Unyielded (Dead) Zones: Regions where $\sigma \leq \sigma_y$ and $\boldsymbol{D}(\boldsymbol{u}) = \mathbf{0}$. These zones remain rigid, forming stagnant (dead) areas (e.g., toothpaste at rest in a tube [41]). The unyielded region ($\boldsymbol{D}(\boldsymbol{u}) = \mathbf{0}$) shrinks or expands based on σ_y and applied stresses. For example, in pipe flow, dead zones persist near the centerline if driving forces are weak [42].

Yielded Zones: Regions where $\sigma > \sigma_y$, allowing material to flow. Within yielded zones, a plug zone often emerges, a subregion where shear rate $\mathbf{II}(\boldsymbol{D})$ is negligible, causing the fluid to move as a solid plug (e.g., the core of a lava flow [43]). Even in yielded regions, low shear rates mimic solid-like plug flow.

It is always a challenging task to simulate viscoplastic models. The reason is very obvious by looking into the above presented mathematical model Equation (2.24) which is divided into two distinct regions. One region is concerned with the no deformation, i.e., $\boldsymbol{D}(\boldsymbol{u}) = \mathbf{0}$, and the fluid is not produced, the other region is concerned with deformation, that is, $\boldsymbol{D}(\boldsymbol{u}) \neq \mathbf{0}$, and the fluid is produced. This results in an obvious discontinuity between the two solutions. From the numerical perspective, there is a jump that numerical solvers do not handle, resulting either in slowing a simulation down or causing a divergence. To overcome this difficulty, a regularization technique should be implemented. In our work, we are going to implement the Papanastasiou approach [16]. The Papanastasiou model captures this by smoothly varying η_p, avoiding sharp interfaces. In terms of stress, it can be

written as

$$\boldsymbol{\sigma} = \left[\frac{\sigma_y}{\mathbf{II}(\boldsymbol{D})}(1 - e^{-m\mathbf{II}(\boldsymbol{D})}) + \eta_p)\right] \boldsymbol{D}(\boldsymbol{u}). \tag{2.27}$$

This regularized Papanastasiou model is a widely used framework for modeling Bingham fluids, offering a regularization technique to handle the discontinuous viscosity behavior in the mathematical model. The idea of the regularization technique is that if the stress goes above or below the yield stress, we expect a smooth function, which is ideal for the numerical solver, as there is no discontinuity present in the numerical model. In terms of viscosity, it can be written as

$$\eta(\mathbf{II}(\boldsymbol{D})) = \frac{\sigma_y}{\mathbf{II}(\boldsymbol{D})}\left(1 - e^{-m\mathbf{II}(\boldsymbol{D})}\right) + \eta_p. \tag{2.28}$$

In Equation (2.35), m denotes the stress growth parameter, also known as the regularization parameter, which needs to be sufficiently large. The advantage of the expression in Equation (2.35) is that it can be used over the whole flow domain, i.e. both yielded and unyielded regions. If the regularization parameter m is large enough, the viscosity tends towards η_p [44]. The lower values of m can be used at higher values of yield stress and vice versa [45, 46]. The Papanastasiou model is a popular choice for regularizing Bingham fluids due to its ability to balance accuracy and numerical stability. While it requires careful selection of the regularization parameter, it offers a more realistic representation of the material behavior than some other regularization methods and allows for the use of standard numerical techniques.

2.3.1 Bingham Number

The Bingham number (Bi) is a fundamental dimensionless parameter used to characterize the flow behavior of viscoplastic fluids, particularly those following the Bingham plastic model. It is defined as the ratio of yield stress to viscous stress, typically expressed as

$$Bi = \frac{\sigma_y L}{\eta U}, \tag{2.29}$$

where σ_y is the yield stress, L a characteristic length, η the total viscosity, and U a characteristic velocity. This ratio provides a quantitative measure of the relative

influence of a fluid's resistance to yield versus its internal viscous resistance. Physically, the Bingham number serves as an indicator of how strongly a material resists deformation before yielding. When the Bingham number is small, the material behaves similarly to a Newtonian fluid, with viscous forces dominating. Conversely, high Bingham numbers indicate the presence of significant unyielded (plug) regions and flow localization, which are indicators of yield stress fluids. In this regime, the fluid behaves more like a solid until the applied stress exceeds the yield threshold. This makes the Bingham number particularly important in applications where flow has a significant unyielded region. In practical terms, the Bingham number is pivotal in the modeling and simulation of industrial and natural processes involving complex fluids. It finds relevance in designing pipeline transport systems for slurries, pastes, drilling muds, and cementitious materials, where unyielded zones may lead to increased pressure drop or clogging. In geophysical applications, it is used to predict the mobility of lava or debris flows. In addition, it plays a key role in the processing of consumer products, such as foodstuffs and cosmetics, where controlled flow under stress is desirable.

As far as computational implementations are concerned, the Bingham number has implications in the convergence and stability of numerical solvers. Large values of Bi correspond to strong (sharp) transitions between yielded and unyielded regions of the domain, which are hard to reproduce numerically. Therefore, regularized models, such as the Papanastasiou ones, are frequently used to mimic the ideal Bingham behavior and yet allow numerical manipulation [as already mentioned above].

In summary, the Bingham number is a key parameter describing the interplay between yield stress and viscosity of a viscoplastic fluid. Not confined only to theoretical fluid dynamics, it has widespread applications in engineering and science, where understanding and predicting complex flow patterns is often essential.

2.4 Elastoviscoplastic Model

So far we have discussed the elastic and plastic behavior of fluids, and their combined effect results in elastoviscoplastic fluids. This section deals with the understanding of elastoviscoplastic fluids and later helps develop an understanding of the model that

we will employ in our simulations. Elastoviscoplastic fluids represent a class of materials that exhibit both viscous and plastic behavior, transitioning from a solid-like to a fluid-like state under certain stress conditions. This behavior is characterized by yield stress, which is crucial for understanding material flow, particularly in applications such as food processing, petroleum engineering, and various industrial processes. The Saramito model is a widely recognized constitutive model that captures the complex interplay of viscoelastic and viscoplastic behaviors, making it a focal point of recent research in this domain. To describe this kind of complex behavior of fluids, recent elastoviscoplastic models have played a vital role. The constitutive properties of such complex fluids usually involve a combination of elastic and plastic behaviors, leading to the development of elastoviscoplastic or viscoelastoplastic fluid models [47, 12]. Numerous models have been proposed to observe such complex fluid behavior [17, 40, 12]. In 2007, Saramito [23] introduced an elastoviscoplastic model, which is a combination of the viscoplastic Bingham and the Oldroyd models, offering an in-depth framework for understanding these materials. In his work, by introducting the one-dimensional version of the model by combing viscoplastic and viscoelastic fluids, he elaborates his model by claiming before yielding, the whole system predicts only recoverable Kelvin–Voigt viscoelastic deformation and ss soon as the strain energy exceeds the level required by the von Mises criterion, the stress in the friction element attains the yield value and the element breaks allowing deformation of all the other elements. After yielding, the deformation of these elements describes the Oldroyd-type viscoelastic behavior. The time-independent Saramito model, combined with the conservation of momentum and mass, reads

$$\begin{cases} \lambda\,\dot{\boldsymbol{\sigma}} + \max\left(0, \dfrac{|\boldsymbol{\sigma}_d| - \sigma_y}{|\boldsymbol{\sigma}_d|}\right)\boldsymbol{\sigma} = 2\eta_m \boldsymbol{D}(\boldsymbol{u}), \\ \rho\,(\boldsymbol{u}\cdot\nabla\boldsymbol{u}) - \nabla\,(-p\boldsymbol{I} + 2\eta\boldsymbol{D}(\boldsymbol{u}) + \boldsymbol{\sigma}) = \mathbf{f}, \\ \nabla\cdot\boldsymbol{u} = 0, \\ \boldsymbol{u} = \boldsymbol{u}_\Gamma \quad \text{on } \partial\Omega, \\ \boldsymbol{\sigma} = \boldsymbol{\sigma}_\Gamma \quad \text{on } \partial\Omega. \end{cases} \tag{2.30a}$$

In Equation (2.30) $\dot{\boldsymbol{\sigma}}$ reads:

$$\dot{\boldsymbol{\sigma}} = \boldsymbol{u}\cdot\nabla\boldsymbol{\sigma} + \boldsymbol{\sigma}\cdot\boldsymbol{W}(\boldsymbol{u}) - \boldsymbol{W}(\boldsymbol{u})\cdot\boldsymbol{\sigma} - a(\boldsymbol{\sigma}\cdot\boldsymbol{D}(\boldsymbol{u}) + \boldsymbol{D}(\boldsymbol{u})\cdot\boldsymbol{\sigma}), \tag{2.31}$$

where λ denotes the relaxation parameter, ρ the density, $\boldsymbol{u}$ the velocity. The solvent and the polymer viscosities are represented by η and η_m respectively. The total viscosity is $\eta_0 = \eta_m + \eta$, $\boldsymbol{f}$ represents the external force, p the pressure. The rate of deformation is $\boldsymbol{D}(\boldsymbol{u}) = (\nabla \boldsymbol{u} + \nabla \boldsymbol{u}^T)/2$ and the vorticity tensor is represented as $\boldsymbol{W}(\boldsymbol{u}) = (\nabla \boldsymbol{u} - \nabla \boldsymbol{u}^T)/2$, $\boldsymbol{\sigma}$ represents the stress, σ_y the yield stress and $\boldsymbol{\sigma}_d$ the deviatoric part of the stress $\boldsymbol{\sigma}$ which is represented as:

$$\boldsymbol{\sigma}_d = \boldsymbol{\sigma} - (\mathrm{tr}(\boldsymbol{\sigma})/N)\boldsymbol{I}, \tag{2.32}$$

with N as a spatial dimension, $|\boldsymbol{\sigma}_d| = \sqrt{\mathrm{tr}(\boldsymbol{\sigma}_d \cdot \boldsymbol{\sigma}_d)}$ is the second invariant of deviatoric stress. In Equation (2.31), a is the material parameter that is associated to the Gordon–Schowalter's derivative [48, 49], $a = 1$ represents the upper convected derivative and $a = -1$ represents the lower convected derivatives. The model represented in Equation (2.30) behaves as a Kelvin-Voigt viscoelastic solid before yielding, and after yielding, it behaves as an Oldroyd viscoelastic fluid. Additionally, the model acts as viscoplastic when $\lambda = 0$, while it exhibits viscoelastic properties when $\sigma_y = 0$. In 2008, Saramito presented an improved version of this model [50]. Saramito's work has been influential in offering a clearer framework for studying the behavior of such complex fluids. In the modeling of such types of equations, the numerical variables depend on the choice of various constitutive models. Many of these constitutive models involve different numerical frameworks to handle the transition between the solid and liquid phases, such as the Saramito model. Although these strategies offer improved accuracy, the numerical treatment becomes significantly more complex, primarily due to the challenges of identifying the interface between the two phases [13]. To address these complexities, we propose a similar approach from Chaparian et al [13, 14]. In our work, we combine the constitutive models of the Oldroyd-B, which has been used as a benchmark for many different numerical techniques [15], and the Papanastasiou regularized model [16] for Bingham fluids within a single Eulerian numerical framework. This strategy, which has recently gained attention in elastoviscoplasticity studies, has demonstrated promising qualitative results.

2.4.1 Papanastasiou Regularized Elastoviscoplastic Model

By incorporating the model presented in Equation (2.35) into the momentum equation and combining it with the Oldroyd-B model, which captures viscoelastic effects, our approach provides a comprehensive simulation platform for elastoviscoplastic fluids. The steady state elastoviscoplastic fluid model combines with the conservation of momentum and mass equations reads:

$$\begin{cases} \lambda\left(\boldsymbol{u}\cdot\nabla\boldsymbol{\sigma}-\nabla\boldsymbol{u}\cdot\boldsymbol{\sigma}-\boldsymbol{\sigma}\cdot\nabla\boldsymbol{u}^{T}\right)+f(\boldsymbol{\sigma})\boldsymbol{\sigma}=2\eta_m\boldsymbol{D}(\boldsymbol{u}), \\ \rho\left(\boldsymbol{u}\cdot\nabla\boldsymbol{u}\right)-\nabla\cdot\left(-p\boldsymbol{I}+2\eta(\mathbf{II}(\boldsymbol{D}))\boldsymbol{D}(\boldsymbol{u})+\boldsymbol{\sigma}\right)=0, \\ \nabla\cdot\boldsymbol{u}=0, \\ \boldsymbol{u}=\boldsymbol{u}_\Gamma \quad \text{on } \partial\Omega, \\ \boldsymbol{\sigma}=\boldsymbol{\sigma}_\Gamma \quad \text{on } \partial\Omega. \end{cases} \tag{2.33}$$

In our work the parameter a in Equation (2.31) is set to $a=1$ to obtain the Oldroyd-B model, i.e the upper convective derivative and our $\dot{\boldsymbol{\sigma}}$ reads as

$$\dot{\boldsymbol{\sigma}}=\left(\boldsymbol{u}\cdot\nabla\boldsymbol{\sigma}-\nabla\boldsymbol{u}\cdot\boldsymbol{\sigma}-\boldsymbol{\sigma}\cdot\nabla\boldsymbol{u}^{T}\right), \tag{2.34}$$

$\eta(\mathrm{II}(D))$ can be written as

$$\eta(\mathbf{II}(\boldsymbol{D}))=\frac{\sigma_y}{\mathbf{II}(\boldsymbol{D})}\left(1-e^{-m\mathbf{II}(\boldsymbol{D})}\right)+\eta_p. \tag{2.35}$$

The parameter $f(\boldsymbol{\sigma})$ can be choosen in a way that the model can be choosen as Oldroyd-B, FENE-P or Giesekus.

$$\begin{cases} f(\boldsymbol{\sigma})=1 & \text{(Oldroyd-B model)}, \\ f(\boldsymbol{\sigma})=1+\dfrac{3a+(\lambda/\eta_m)\mathrm{tr}(\boldsymbol{\sigma})}{L^2} & \text{(FENE-P model)}, \\ f(\boldsymbol{\sigma})=\boldsymbol{\sigma}+\alpha\lambda\eta_p^{-1}\boldsymbol{\sigma}\cdot\boldsymbol{\sigma} & \text{(Giesekus model)}. \end{cases} \tag{2.36a}$$

In Equation (2.36), the coefficient a in the FENE-P model is defined as

$$a = \frac{L^2}{L^2 - 3}, \tag{2.37}$$

where L characterizes the finite extensibility of the polymer molecules. The choice of $f(\boldsymbol{\sigma})$ governs how stress growth and relaxation are modulated by the configuration of the fluid's microstructure. This unified framework allows for the simulation and analysis of various fluid behaviors under different assumptions on microstructural elasticity and anisotropy, providing a robust base for the computational studies undertaken in the subsequent chapters.

Chapter 3

Finite Element Method

The finite element method (FEM) has received widespread acceptance as one of the most general and applicable numerical approaches for partial differential equations (PDEs) describing diverse physical phenomena, and most notably solid and fluid mechanics. The success of FEM is due to its ability to deal with complex geometries, adaptive mesh refinements and high order approximations, which are essential these days for scientific computation. Finite element method (FEM) represents a strong computational approach for non-Newtonian fluid mechanics and can be utilized for the simulation of non-linear constitutive flows including viscoelastic, yield stress and thixotropic response.

One of the main advantages of FEM with respect to other numerical procedures (e.g. finite difference and finite volume method) is its natural settlement of unstructured meshes, particularly in problems with the involvement of complex domains and/or moving boundaries [51]. In addition, the variational foundation of the method allows for a systematic treatment of different boundary conditions and coupling mechanisms, which are often encountered in multiphysics problems. For elastoviscoplastic materials that exhibit elastic and viscous behaviors, the FEM must be carefully tailored to address the related challenges, including high Weissenberg number problem also known as HWNP, yield stress phenomena, and the need for mixed formulations to ensure stability.

This chapter presents a comprehensive discussion of FEM as applied to the simulation of elastoviscoplastic fluids. We begin with an overview of the fundamental

principles of FEM, including weak formulations, Galerkin approximations, and numerical integration. Subsequently, we discuss specialized techniques for handling the constitutive complexity of elastoviscoplastic materials, focusing on stability and efficiency.

3.1 Advection Diffusion Equation

To provide a general overview of the finite element method, we consider the two-dimensional advection–diffusion equation. Let $\Omega \subset \mathbb{R}^2$ denote a bounded domain with Lipschitz boundary $\partial\Omega$, and let $(0, T] \subset \mathbb{R}$ represent the time interval of interest. The governing problem is given by the following system:

$$\frac{\partial u}{\partial t} + \boldsymbol{\alpha} \cdot \nabla u = \nabla \cdot (D \nabla u) + f \qquad \text{in } \Omega \times (0, T], \tag{3.1a}$$

$$u = g \qquad \text{on } \partial\Omega \times (0, T], \tag{3.1b}$$

$$u(\boldsymbol{x}, 0) = u_0 \qquad \text{in } \Omega, \tag{3.1c}$$

where $\boldsymbol{\alpha} \in \mathbb{R}^2$ is the prescribed advection (velocity) vector, D denotes the diffusion coefficient, and $f = f(\boldsymbol{x}, t)$ represents a source or sink term influencing the scalar field $u = u(\boldsymbol{x}, t)$ [52]. For the purposes of exposition, we assume $D > 0$ is a scalar constant corresponding to isotropic diffusion; in the more general case, $D = D(\boldsymbol{x})$ may be a symmetric positive definite tensor accounting for anisotropic effects.

Equation (3.1a) constitutes the strong form of the advection–diffusion problem. The boundary condition (3.1b) prescribes the concentration field on the boundary $\partial\Omega$, while (3.1c) specifies the initial state at time $t = 0$. Before deriving the corresponding weak formulation, we briefly review several key definitions that will be required in the finite element setting.

- The set of all functions that are continuous within the domain Ω is represented by $C(\Omega)$ or $C^0(\Omega)$. If a function has a continuous first order partial derivative, it lies in the space $C^1(\Omega)$. More generally, if a function possesses continuous partial derivatives up to order $k \in \mathbb{N}$, it belongs to the $C^k(\Omega)$ space.

- The L^2 space (Lebesgue space) consists of all measurable functions $u : \Omega \to \mathbb{R}$ such that the square of the absolute value of u is integrable over the domain Ω. Mathematically, this is expressed as

$$L^2(\Omega) = \left\{ u : \Omega \to \mathbb{R} \;\middle|\; \int_\Omega |u(\boldsymbol{x})|^2 \, d\boldsymbol{x} < \infty \right\}. \tag{3.2}$$

- The H^1 space (Sobolev space) is defined as

$$H^1(\Omega) = \left\{ u \in L^2(\Omega) \;\middle|\; \frac{\partial u}{\partial x_i} \in L^2(\Omega),\ i = 1, 2 \right\}. \tag{3.3}$$

- The special Sobolev space $H_0^1(\Omega)$ is defined as the set of all $u \in H^1(\Omega)$ such that $u = 0$ on $\partial\Omega$. Mathematically it can be expressed as:

$$H_0^1(\Omega) = \left\{ u \in H^1(\Omega) : u = 0 \text{ on } \partial\Omega \right\}. \tag{3.4}$$

- One of the most important theorems from vector calculus to reformulate the strong form is Green's theorem or Green's first theorem. It is useful in the simplification of the weak form. The theorem states mathematically:

$$\int_\Omega (\nabla^2 u) v \, d\boldsymbol{x} = -\int_\Omega \nabla u \cdot \nabla v \, d\boldsymbol{x} + \int_{\partial\Omega} (\nabla u \cdot \mathbf{n}) v \, dS. \tag{3.5}$$

In Equation (3.9) there are two types of integrals. The integral on the extreme right hand is the line integral over the boundary and $\mathbf{n}$ is the unit outward normal vector to the boundary $\partial\Omega$ of the domain, the remaining two integrals are on the domainΩ. In Equation (3.9) the dot between the gradients denotes the Euclidean product of vectors and mathematically it can be expressed as:

$$\nabla u \cdot \nabla v = \frac{\partial u}{\partial x}\frac{\partial v}{\partial x} + \frac{\partial u}{\partial y}\frac{\partial v}{\partial y} + \cdots \tag{3.6}$$

3.1.1 Variational Formulation

For the variational form of the given model problem in Equations (3.1a)-(3.1c), the trail and test functions are:

$$V = H^1(\Omega), \quad W = \left\{ w \in H^1(\Omega) : w = 0 \text{ on } \partial\Omega \right\}, \tag{3.7}$$

multiplying Equation (3.1a) by an arbitrary test function $w \in W$ and integrating the expression over the domain Ω

$$\int_\Omega \frac{\partial u}{\partial t} w \, d\Omega + \int_\Omega (\boldsymbol{\alpha} \cdot \nabla u) w \, d\Omega = \int_\Omega \nabla \cdot (D \nabla u) w \, d\Omega + \int_\Omega f w \, d\Omega. \tag{3.8}$$

Applying Green theorem on the diffusive term yields

$$\int_\Omega (D \Delta u) w \, d\boldsymbol{x} = - \int_\Omega D \nabla u \cdot \nabla w \, d\boldsymbol{x} + \underbrace{\int_{\partial\Omega} (D \nabla u \cdot \mathbf{n}) w \, dS}_{=0 \text{ (since } w|_{\partial\Omega}=0)}. \tag{3.9}$$

Let us introduce the bilinear forms and functionals:

$$(u, w) = \int_\Omega uw \, d\boldsymbol{x}, \tag{3.10}$$

$$a(u, w) = \int_\Omega D \nabla u \cdot \nabla w \, d\boldsymbol{x} = D \int_\Omega \left(\frac{\partial u}{\partial x} \frac{\partial w}{\partial x} + \frac{\partial u}{\partial y} \frac{\partial w}{\partial y} \right) d\boldsymbol{x}, \tag{3.11}$$

$$b(u, w) = \int_\Omega (\boldsymbol{\alpha} \cdot \nabla u) w \, d\boldsymbol{x} = \boldsymbol{\alpha} \int_\Omega \left(\frac{\partial u}{\partial x} w + \frac{\partial u}{\partial y} w \right) d\boldsymbol{x}. \tag{3.12}$$

The weak formulation of (3.1a) is to find $u \in V$ such that

$$\left(\frac{\partial u}{\partial t}, w \right) + b(u, w) = a(u, w) + f(w), \quad \forall \quad w \in W. \tag{3.13}$$

3.1.2 Finite Element Discretization

Let V_h be a finite dimensional subspace of V, spanned by the basis functions $\{\varphi_1, \varphi_2, \ldots, \varphi_N\}$. The approximate solution $u_h \in V_h$ is expressed as a linear combination of these basis functions:

$$u_h(\boldsymbol{x}, t) = \sum_{j=1}^{N} u_j(t) \varphi_j(x), \tag{3.14}$$

where $u_j(t)$ are the time-dependent coefficients to be determined.

The semi discrete Galerkin formulation reads: find $u_h(t) \in V_h$ such that

$$\left(\frac{\partial u_h}{\partial t}, w_h\right) + b(u_h, w_h) + a(u_h, w_h) = f(w_h), \quad \forall w_h \in V_h, \tag{3.15}$$

where the bilinear forms are defined as:

$$a(u_h, w_h) = \int_\Omega D\nabla u_h \cdot \nabla w_h \, d\boldsymbol{x}, \tag{3.16}$$

$$b(u_h, w_h) = \int_\Omega (\boldsymbol{\alpha} \cdot \nabla u_h) w_h \, d\boldsymbol{x}. \tag{3.17}$$

Substituting the expansion (3.14) into the weak form and choosing $w_h = \varphi_i$ for $i = 1, \ldots, N$, we obtain the following system of equations:

$$\sum_{j=1}^{N} \left(\int_\Omega \varphi_j \varphi_i \, d\boldsymbol{x} \right) \frac{\partial u_j}{\partial t} + \sum_{j=1}^{N} \left(\int_\Omega (\boldsymbol{\alpha} \cdot \nabla \varphi_j) \varphi_i \, d\boldsymbol{x} \right) u_j + \sum_{j=1}^{N} \left(\int_\Omega D\nabla \varphi_j \cdot \nabla \varphi_i \, d\boldsymbol{x} \right) u_j = \int_\Omega f \varphi_i \, d\boldsymbol{x}. \tag{3.18}$$

This leads to the matrix form:

$$M \frac{\partial u}{\partial t} + (A + B)u = F, \tag{3.19}$$

where

$$M = m_{ij} = \int_\Omega \varphi_j \varphi_i \, d\boldsymbol{x}, \quad \text{(mass matrix)} \tag{3.20}$$

$$A = a_{ij} = \int_\Omega D\nabla \varphi_j \cdot \nabla \varphi_i \, d\boldsymbol{x}, \quad \text{(stiffness matrix)} \tag{3.21}$$

$$B = b_{ij} = \int_\Omega (\boldsymbol{\alpha} \cdot \nabla \varphi_j) \varphi_i \, d\boldsymbol{x}, \quad \text{(convection matrix)} \tag{3.22}$$

$$F = f_i = \int_\Omega f \varphi_i \, d\boldsymbol{x}. \quad \text{(load vector)} \tag{3.23}$$

3.1.3 Time Discretization: θ-Method

To discretize in time, we apply the θ-method. For a time step Δt, we define:

$$u^n \approx u(t_n), \quad u^{n+1} \approx u(t_{n+1}), \quad t^{n+1} = t^n + \Delta t. \tag{3.24}$$

The θ-method gives the following update scheme

$$[M + \theta h(A + B)]u^{n+1} = [M - (1 - \theta)h(A + B)]u^n + h[\theta F^{n+1} + (1 - \theta)F^n]. \tag{3.25}$$

Special cases:

- $\theta = 0$: Forward Euler (explicit),
- $\theta = 1$: Backward Euler (fully implicit),
- $\theta = \dfrac{1}{2}$: Crank–Nicolson (semi implicit, second order accurate).

3.1.4 Stabilization

The discretization of the convective term $\boldsymbol{\alpha} \cdot \nabla u$ results in a non symmetric system matrix B, which may give rise to spurious oscillations and numerical instabilities, particularly for large values of the mesh Péclet number

$$Pe = \frac{|\boldsymbol{\alpha}|\, h}{2D} \gg 1, \tag{3.26}$$

where h denotes the local mesh size and D is the diffusion coefficient. One way to stabilize this convective term is by adding anisotropic balancing dissipation of the form

$$-\nabla \cdot (\tau \boldsymbol{\alpha} \otimes \boldsymbol{\alpha} \nabla u)\,, \tag{3.27}$$

where τ is a suitably chosen stabilization parameter. Another approach is to modify the test functions in the weak formulation.

$$\tilde{\varphi}_i := \varphi_i + \tau \boldsymbol{\alpha} \cdot \nabla \varphi_i, \tag{3.28}$$

inserting this modified test function into the variational form leads to a stabilized discrete convection operator $\tilde{B}$ with entries:

$$\tilde{b}_{ij} = b_{ij} + \int_{\Omega} \tau(\boldsymbol{\alpha} \cdot \nabla\varphi_i)(\boldsymbol{\alpha} \cdot \nabla\varphi_j)\, d\boldsymbol{x}, \quad i,j = 1,\ldots,N. \tag{3.29}$$

This formulation yields the Streamline Upwind Petrov Galerkin (SUPG) method [53], which is one of the most prominent stabilized finite element methods for convection dominated transport problems. The artificial diffusion stabilization and EOFEM is discussed in detail in the later sections.

3.1.5 Shape Functions

Consider a rectangular domain $\Omega = (0,c) \times (0,d)$. In 2D finite element analysis, the meshes are made up of triangular and/or quadrilateral elements. Figure 3.1 presents the bilinear quadrilateral master element, which consists of four nodes. The coordinates of the reference element, denoted as η and ξ, are defined within the standard domain ranging from -1 to 1. The shape functions associated with this element can be derived either by employing the general functional form and enforcing the Kronecker delta property or by systematically constructing them through the combination of appropriate linear one-dimensional shape functions.

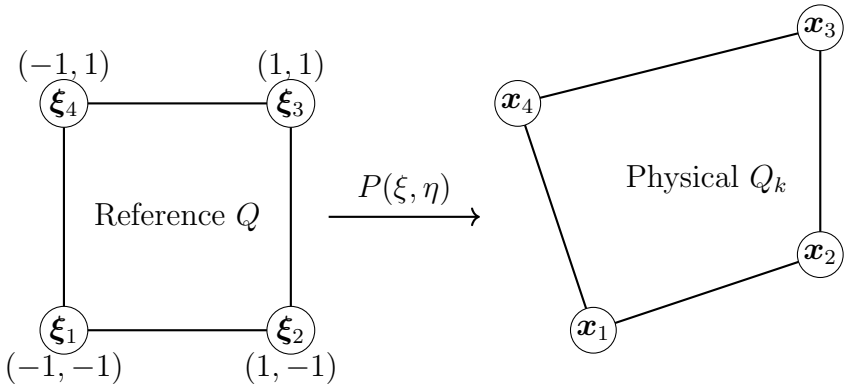

FIGURE 3.1: Mapping from reference coordinates (ξ,η) to physical coordinates (x,y).Each vertex is defined as $\boldsymbol{x}_1 = (x_1,y_1)$, $\boldsymbol{x}_2 = (x_2,y_2)$, $\boldsymbol{x}_3 = (x_3,y_3)$, $\boldsymbol{x}_4 = (x_4,y_4)$, and $\boldsymbol{\xi}_i = (\xi_i,\eta_i)$, $i = 1,\ldots,4$. . Left: Master/reference element. Right: Arbitrary physical quadrilateral element.

By transforming the actual element into a master element (the reference element), integration and computational implementation become easier.

TABLE 3.1: Shape Functions for $\mathbb{Q}_1$ Element

General Form of Shape Functions	**Shape Functions for $\mathbb{Q}_1$ (in terms of ξ and η)**
$\psi = A + B\xi + C\eta + D\xi\eta$	$\psi_1^e = \frac{1}{4}(1-\xi)(1-\eta)$ $\psi_2^e = \frac{1}{4}(1+\xi)(1-\eta)$ $\psi_3^e = \frac{1}{4}(1+\xi)(1+\eta)$ $\psi_4^e = \frac{1}{4}(1-\xi)(1+\eta)$

3.1.6 Gauss Quadrature

In the context of finite element method, the evaluation of stiffness matrices and load vectors through numerical integration techniques is fundamental to developing a general purpose finite element solver. This approach enables the solution of any differential equation without requiring modifications in the core implementation. To perform the integration of the definite integral, usually two methods are used, Newton Cotes and the Gauss quadrature method. In this study, we used the Gauss quadrature (GQ) technique, which is known for its most accurate numerical approximations. In this technique, the master element contributes as a reference for the computation of integrals. The coordinates of the element are transformed to a normalized space where all elements, regardless of their specific shape, can use the same set of Gaussian quadrature points and weights. The fundamental assumption of the Gauss method is that the weight coefficients depend on the number of base points, or Gauss integration points, and that the polynomial function is evaluated between -1 and $+1$. This transformation allows for the application of the same set of quadrature points and weights regardless of the actual element's size, shape, or orientation. This standardization significantly reduces the complexity of the numerical integration process. The basic assumption in Gauss numerical integration is that the polynomial function is evaluated in the interval -1 to $+1$, and the weight

coefficients depend on the number of base points known as Gauss integration points.

$$\int_{-1}^{1} f(\xi)\, d\xi = w_1 f(\xi_1) + w_2 f(\xi_2) + \cdots + w_n f(\xi_n) \tag{3.30}$$

where w_i are the weight coefficients and $\xi_1, \ldots, \xi_n$ are the base points. This can be generalized as

$$\int_{-1}^{1} f(\xi)\, d\xi = \sum_{i=1}^{n} w_i f(\xi_i) \tag{3.31}$$

The order of Gauss integration depends on the number of Gauss points selected. By increasing the number of Gauss points, the accuracy of the solution increases but the computational cost also increases. Hence, in the Gauss quadrature method, we select Gauss points and weights such that the integration formula provides an exact solution for polynomials of degree $2n - 1$.

3.1.7 GQ Points and Weights for 2D Quadrilateral Elements

For 2D quadrilateral elements, the Gaussian quadrature is applied in both the ξ direction and the η direction. Gaussian quadrature allows for efficient numerical integration of element matrices. The integral over the element is computed as

$$\begin{aligned} \int_{\Omega^e} f(x, y)\, dA &= \int_{-1}^{1} \int_{-1}^{1} f(\xi, \eta)\, |\det \boldsymbol{J}^e(\xi, \eta)|\; d\xi\, d\eta \\ &\approx \sum_{i=1}^{n} \sum_{j=1}^{n} w_i w_j\, f(\xi_i, \eta_j)\; |\det \boldsymbol{J}^e(\xi_i, \eta_j)| \end{aligned} \tag{3.32}$$

where w_{ξ_i} and w_{η_j} are the weights corresponding to the Gaussian quadrature points in the ξ-direction and the η-direction, and $f(\xi_i, \eta_j)$ is the integrand evaluated at the Gauss points.

Below is a table of the GQ points and weights for NGP = 1, NGP = 4, and NGP = 9, which are commonly used for quadrilateral elements.

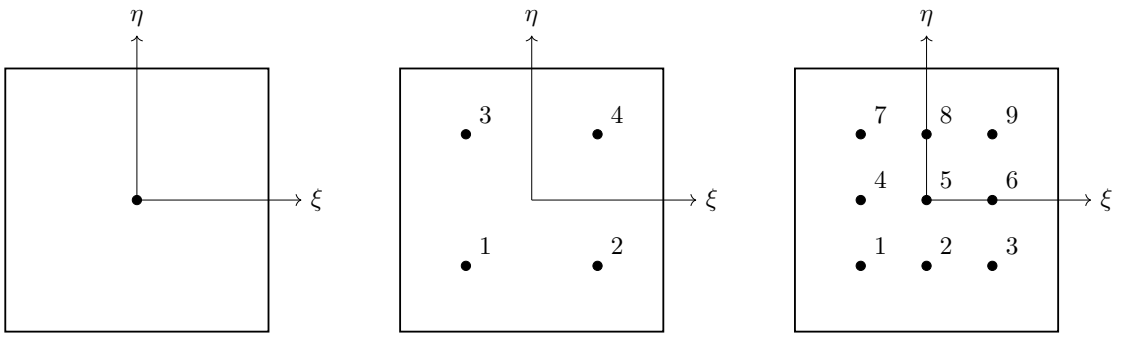

FIGURE 3.2: Schematics of Gauss quadrature points in the reference element: (a) 1×1, (b) 2×2, and (c) 3×3 Gauss point rules

TABLE 3.2: Gauss quadrature points and weights for quadrilateral elements.

Scheme	Point	ξ	η	Weight
1-point	1	0	0	2
4-point	1	$-1/\sqrt{3}$	$-1/\sqrt{3}$	1
	2	$1/\sqrt{3}$	$-1/\sqrt{3}$	1
	3	$-1/\sqrt{3}$	$1/\sqrt{3}$	1
	4	$1/\sqrt{3}$	$1/\sqrt{3}$	1
9-point	1	$-\sqrt{3/5}$	$-\sqrt{3/5}$	25/81
	2	0	$-\sqrt{3/5}$	40/81
	3	$\sqrt{3/5}$	$-\sqrt{3/5}$	25/81
	4	$-\sqrt{3/5}$	0	40/81
	5	0	0	64/81
	6	$\sqrt{3/5}$	0	40/81
	7	$-\sqrt{3/5}$	$\sqrt{3/5}$	25/81
	8	0	$\sqrt{3/5}$	40/81
	9	$\sqrt{3/5}$	$\sqrt{3/5}$	25/81

3.1.8 Reference Element Mapping and Basis Functions

We consider a two dimensional domain $\Omega = (0,1) \times (0,1)$, discretized using a structured quadrilateral mesh $\mathcal{T}_h$. The mesh consists of quadrilateral elements $\mathcal{T}_e \in \mathcal{T}_h$, each defined by four vertices $\boldsymbol{x}_1 = (x_1, y_1)$, $\boldsymbol{x}_2 = (x_2, y_2)$, $\boldsymbol{x}_3 = (x_3, y_3)$, $\boldsymbol{x}_4 = (x_4, y_4)$. The element size is uniform and denoted by $h = \frac{1}{N}$, where N is the number of intervals along each spatial direction. Each element $\mathcal{T}_e$ uses local bilinear basis

functions $\psi_i^e(\boldsymbol{x}),\ i = 1, 2, 3, 4$, which satisfy the Kronecker delta property:

$$\psi_i^e(\boldsymbol{x}_j) = \begin{cases} 1 & \text{if } i = j \\ 0 & \text{if } i \neq j \end{cases} \quad \text{for } i, j = 1, 2, 3, 4. \tag{3.33}$$

These local functions are the restriction of global basis functions φ_i to the element $\mathcal{T}_e$, and are employed for interpolation and assembly of the finite element system. To facilitate integration and differentiation on arbitrary quadrilaterals, we define an isoparametric bilinear mapping from a reference square $\hat{\mathcal{T}} \subset \mathbb{R}^2$ with vertices

$$\hat{\boldsymbol{x}}_1 = (-1, -1), \quad \hat{\boldsymbol{x}}_2 = (1, -1), \quad \hat{\boldsymbol{x}}_3 = (1, 1), \quad \hat{\boldsymbol{x}}_4 = (-1, 1), \tag{3.34}$$

to any physical element $\mathcal{T}_e$. The mapping is given by

$$P : \hat{\mathcal{T}} \to \mathcal{T}_e, \quad (\xi, \eta) \mapsto P(\xi, \eta) = \sum_{i=1}^{4} \psi_i^e(\xi, \eta)\boldsymbol{x}_i = (x, y), \tag{3.35}$$

where the basis functions $\psi_i^e(\xi, \eta) \in \mathbb{Q}_1(\hat{\mathcal{T}})$ on the reference element are defined as

$$\psi_1^e(\xi, \eta) = \frac{1}{4}(1 - \xi)(1 - \eta), \tag{3.36}$$

$$\psi_2^e(\xi, \eta) = \frac{1}{4}(1 + \xi)(1 - \eta), \tag{3.37}$$

$$\psi_3^e(\xi, \eta) = \frac{1}{4}(1 + \xi)(1 + \eta), \tag{3.38}$$

$$\psi_4^e(\xi, \eta) = \frac{1}{4}(1 - \xi)(1 + \eta). \tag{3.39}$$

Any function $f_e \in \mathbb{Q}_1(\mathcal{T}_e)$ can be expressed in reference coordinates as

$$f_e(\xi, \eta) = \sum_{i=1}^{4} f_i \psi_i^e(\xi, \eta) = c_1 + c_2\xi + c_3\eta + c_4\xi\eta, \tag{3.40}$$

where f_i are the nodal values at the vertices of $\mathcal{T}_e$, and $c_1, \ldots, c_4 \in \mathbb{R}$ are constants determined by these nodal values.

3.1.9 Matrix Assembly

Using the reference mapping, the element stiffness matrix contribution from quadrilateral T_e is expressed as

$$A_{ij}^{(e)} = a_e(\varphi_j, \varphi_i) = \int_{T_e} \nabla\varphi_j \cdot \nabla\varphi_i \, dx\, dy = \int_{\hat{T}} \nabla\psi_j^e \cdot \nabla\psi_i^e \, |\det(\boldsymbol{J})| \, d\xi \, d\eta. \tag{3.41}$$

The gradient product in reference coordinates expands to

$$\begin{aligned} \nabla\psi_j^e \cdot \nabla\psi_i^e = (\xi_x^2 + \xi_y^2)\frac{\partial\psi_j^e}{\partial\xi}\frac{\partial\psi_i^e}{\partial\xi} + (\eta_x^2 + \eta_y^2)\frac{\partial\psi_j^e}{\partial\eta}\frac{\partial\psi_i^e}{\partial\eta} \\ + (\xi_x\eta_x + \xi_y\eta_y)\left(\frac{\partial\psi_j^e}{\partial\xi}\frac{\partial\psi_i^e}{\partial\eta} + \frac{\partial\psi_j^e}{\partial\eta}\frac{\partial\psi_i^e}{\partial\xi}\right). \end{aligned} \tag{3.42}$$

where we define

$$X_1 = \xi_x^2 + \xi_y^2, \quad X_2 = \eta_x^2 + \eta_y^2, \quad X_3 = \xi_x\eta_x + \xi_y\eta_y. \tag{3.43}$$

The stiffness matrix integrand becomes

$$\begin{aligned} A_{ij}^{(e)} = \int_{-1}^{1}\int_{-1}^{1} \Big[X_1 \frac{\partial\psi_j^e}{\partial\xi}\frac{\partial\psi_i^e}{\partial\xi} + X_2 \frac{\partial\psi_j^e}{\partial\eta}\frac{\partial\psi_i^e}{\partial\eta} \\ + X_3\left(\frac{\partial\psi_j^e}{\partial\xi}\frac{\partial\psi_i^e}{\partial\eta} + \frac{\partial\psi_j^e}{\partial\eta}\frac{\partial\psi_i^e}{\partial\xi}\right)\Big] |\det(\boldsymbol{J})| \, \mathrm{d}\xi \, \mathrm{d}\eta. \end{aligned} \tag{3.44}$$

The bilinear mapping from the reference square $\hat{\mathcal{T}} = [-1, 1]^2$ to a physical element $\mathcal{T}_e$ is given by

$$x(\xi, \eta) = \sum_{k=1}^{4} x_k \psi_k(\xi, \eta), \qquad y(\xi, \eta) = \sum_{k=1}^{4} y_k \psi_k(\xi, \eta), \tag{3.45}$$

The Jacobian matrix $\boldsymbol{J}$ is

$$\boldsymbol{J} = \begin{pmatrix} \dfrac{\partial x}{\partial\xi} & \dfrac{\partial x}{\partial\eta} \\ \dfrac{\partial y}{\partial\xi} & \dfrac{\partial y}{\partial\eta} \end{pmatrix} = \begin{pmatrix} J_{11} & J_{12} \\ J_{21} & J_{22} \end{pmatrix}, \tag{3.46}$$

$$\det(\boldsymbol{J}) = J_{11}J_{22} - J_{12}J_{21}, \quad \boldsymbol{J}^{-1} = \frac{1}{\det(\boldsymbol{J})}\begin{pmatrix} J_{22} & -J_{12} \\ -J_{21} & J_{11} \end{pmatrix} = \begin{pmatrix} \xi_x & \xi_y \\ \eta_x & \eta_y \end{pmatrix}. \tag{3.47}$$

$$\mathcal{K}_{ij} = X_1\psi_{i,\xi}\psi_{j,\xi} + X_2\psi_{i,\eta}\psi_{j,\eta} + X_3(\psi_{i,\xi}\psi_{j,\eta} + \psi_{i,\eta}\psi_{j,\xi}). \tag{3.48}$$

For numerical integration, we use 2×2 Gauss quadrature with points

$$(\xi_q, \eta_q) \in \left\{ \left(\pm\frac{1}{\sqrt{3}}, \pm\frac{1}{\sqrt{3}} \right) \right\}, \quad w_q = 1. \tag{3.49}$$

The following expression leads to the matrix A,

$$A_{ij}^{(e)} \approx \sum_{q=1}^{4} \mathcal{K}_{ij}(\xi_q, \eta_q) \cdot \det(\boldsymbol{J})\Big|_{(\xi_q,\eta_q)}, \tag{3.50}$$

$$A^{(e)} = \frac{1}{6}\begin{pmatrix} 4 & -1 & -2 & -1 \\ -1 & 4 & -1 & -2 \\ -2 & -1 & 4 & -1 \\ -1 & -2 & -1 & 4 \end{pmatrix}. \tag{3.51}$$

For a velocity field $\boldsymbol{\alpha} = (1, 0)$, the convection matrix entry becomes

$$B_{ij}^{(e)} = \int_{\hat{\mathcal{T}}} (\boldsymbol{\alpha} \cdot \nabla\psi_j^e)\psi_i^e \cdot |\det(\boldsymbol{J})|\, d\xi\, d\eta = \int_{\hat{\mathcal{T}}} \frac{\partial\psi_j^e}{\partial x}\psi_i^e \cdot |\det(\boldsymbol{J})|\, d\xi\, d\eta, \tag{3.52}$$

using the Jacobian inverse,

$$\frac{\partial\psi_j^e}{\partial x} = \xi_x\frac{\partial\psi_j^e}{\partial\xi} + \eta_x\frac{\partial\psi_j^e}{\partial\eta}. \tag{3.53}$$

$\xi_x = 2, \eta_x = 0$, so

$$\frac{\partial\psi_j^e}{\partial x} = 2\frac{\partial\psi_j^e}{\partial\xi}, \tag{3.54}$$

$$B_{ij}^{(e)} = \frac{1}{4}\int_{-1}^{1}\int_{-1}^{1}\left(2\frac{\partial\psi_j^e}{\partial\xi}\right)\psi_i^e\, d\xi\, d\eta = \frac{1}{2}\int_{-1}^{1}\int_{-1}^{1}\frac{\partial\psi_j^e}{\partial\xi}\psi_i^e\, d\xi\, d\eta, \tag{3.55}$$

this yields the matrix

$$B^{(e)} = \frac{1}{12}\begin{pmatrix} -2 & 2 & 1 & -1 \\ -2 & 2 & 1 & -1 \\ -1 & 1 & 2 & -2 \\ -1 & 1 & 2 & -2 \end{pmatrix}. \tag{3.56}$$

The local mass matrix is

$$M_{ij}^{(e)} = \int_{T_e} \varphi_j \varphi_i \, dx \, dy = \int_{\hat{\mathcal{T}}} \psi_j^e \psi_i^e \cdot |\det(\boldsymbol{J})| \, d\xi \, d\eta, \tag{3.57}$$

with constant $\det(\boldsymbol{J}) = \frac{1}{4}$, and using 2×2 Gauss quadrature:

$$M_{ij}^{(e)} \approx \frac{1}{4} \sum_{q=1}^{4} \psi_j^e(\xi_q, \eta_q) \psi_i^e(\xi_q, \eta_q), \tag{3.58}$$

$$M^{(e)} = \frac{1}{36} \begin{pmatrix} 4 & 2 & 1 & 2 \\ 2 & 4 & 2 & 1 \\ 1 & 2 & 4 & 2 \\ 2 & 1 & 2 & 4 \end{pmatrix}. \tag{3.59}$$

For a source term $f(x, y) = 1$, the local load vector is

$$F_i = \int_{T_e} f(x, y) \varphi_i(x, y) \, dx \, dy = \int_{\hat{\mathcal{T}}} \psi_i^e(\xi, \eta) \cdot |\det(\boldsymbol{J})| \, d\xi \, d\eta, \tag{3.60}$$

using 2×2 quadrature:

$$F_i \approx \det(\boldsymbol{J}) \sum_{q=1}^{4} \psi_i^e(\xi_q, \eta_q), \tag{3.61}$$

$$F = \frac{1}{4} \begin{pmatrix} 1 \\ 1 \\ 1 \\ 1 \end{pmatrix}. \tag{3.62}$$

3.2 Local to Global Matrix Assembly

Consider a structured 2×2 mesh consisting of 4 quadrilateral elements as shown in Figure below, and denoted by $\mathcal{T}_e$, and 9 globally numbered nodes. Each element contains 4 local degrees of freedom corresponding to bilinear basis functions $\{\psi_1^e, \psi_2^e, \psi_3^e, \psi_4^e\}$ defined on the reference square $\hat{\mathcal{T}}$. To facilitate global assembly, we

define a local to global mapping matrix $LG \in \mathbb{N}^{4\times 4}$ as:

$$LG = \begin{pmatrix} 1 & 2 & 5 & 4 \\ 2 & 3 & 6 & 5 \\ 4 & 5 & 8 & 7 \\ 5 & 6 & 9 & 8 \end{pmatrix}, \tag{3.63}$$

this mapping identifies, for each local node index $i \in \{1, 2, 3, 4\}$, the corresponding global node index for every element $e \in \{1, 2, 3, 4\}$. The local element matrix $A^{(e)} \in \mathbb{R}^{4\times 4}$ is inserted into the global stiffness matrix $A \in \mathbb{R}^{9\times 9}$ using the relation

$$A_{LG(e,i),\,LG(e,j)} \mathrel{+}= A^{(e)}_{ij} \quad \text{for } i, j = 1, \ldots, 4, \ \forall\, e. \tag{3.64}$$

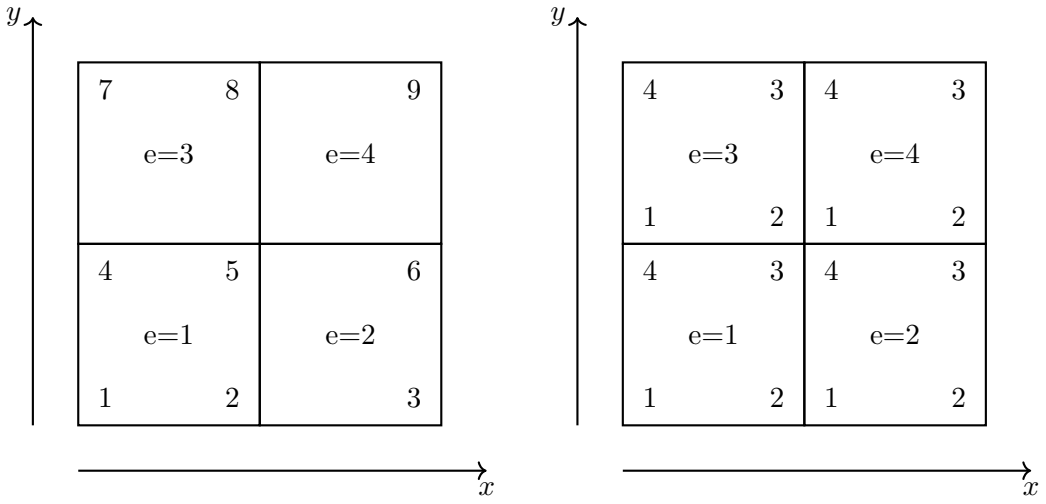

FIGURE 3.3: Element and global numbering (left), and local node numbering (right) for a sample 2D mesh

The matrix A can be read as

$$A = \begin{pmatrix}
A_{11}^{(1)} & A_{12}^{(1)} & 0 & A_{14}^{(1)} & A_{13}^{(1)} & 0 & 0 & 0 & 0 \\
A_{21}^{(1)} & A_{22}^{(1)} + A_{11}^{(2)} & A_{12}^{(2)} & A_{24}^{(1)} & A_{23}^{(1)} + A_{14}^{(2)} & A_{13}^{(2)} & 0 & 0 & 0 \\
0 & A_{21}^{(2)} & A_{22}^{(2)} & 0 & A_{24}^{(2)} & A_{23}^{(2)} & 0 & 0 & 0 \\
A_{41}^{(1)} & A_{42}^{(1)} & 0 & A_{44}^{(1)} + A_{11}^{(3)} & A_{43}^{(1)} + A_{12}^{(3)} & 0 & A_{14}^{(3)} & A_{13}^{(3)} & 0 \\
A_{31}^{(1)} & A_{32}^{(1)} + A_{41}^{(2)} & A_{42}^{(2)} & A_{34}^{(1)} + A_{21}^{(3)} & A_{33}^{(1)} + A_{44}^{(2)} + A_{22}^{(3)} + A_{11}^{(4)} & A_{12}^{(4)} + A_{43}^{(2)} & A_{24}^{(3)} & A_{14}^{(4)} + A_{23}^{(3)} & A_{13}^{(4)} \\
0 & A_{31}^{(2)} & A_{32}^{(2)} & 0 & A_{34}^{(2)} + A_{21}^{(4)} & A_{33}^{(2)} + A_{22}^{(4)} & 0 & A_{24}^{(4)} & A_{23}^{(4)} \\
0 & 0 & 0 & A_{41}^{(3)} & A_{42}^{(3)} & 0 & A_{44}^{(3)} & A_{43}^{(3)} & 0 \\
0 & 0 & 0 & A_{31}^{(3)} & A_{32}^{(3)} + A_{41}^{(4)} & A_{42}^{(4)} & A_{34}^{(3)} & A_{33}^{(3)} + A_{44}^{(4)} & A_{43}^{(4)} \\
0 & 0 & 0 & 0 & A_{31}^{(4)} & A_{32}^{(4)} & 0 & A_{34}^{(4)} & A_{33}^{(4)}
\end{pmatrix}.$$

In the similar way we can construct the other matrices. The preceding two dimensional finite element formulation of the advection-diffusion problem has served as a concrete example, illustrating the essential steps involved in weak formulation, isoparametric mapping, numerical integration, and matrix assembly.

3.3 FEM: Elastoviscoplastic Fluids

Having reviewed the finite element method in detail, including the derivation and assembly of the local element matrices (mass, stiffness, and advection) and their contribution to the global system, we are now in a position to apply this methodology to our specific governing equation. In the finite element analysis of elastoviscoplastic (EVP) fluids described by the Oldroyd-B constitutive law coupled with Bingham plasticity through the Papanastasiou regularization, several major challenges arise. First, the discretization must respect the classical inf–sup condition for velocity–pressure pairs while also accommodating the extra stress as an additional unknown in a three-field formulation, which introduces stability issues [54]. The yield stress introduces a non smooth variational inequality, which in practice is replaced by the Papanastasiou exponential regularization, but the choice of the regularization parameter creates a compromise: too small a parameter over smooths the yield surface, while too large a parameter leads to stiff non-linear systems that are difficult for Newton-type solvers to handle [16]. On the viscoelastic side, the high Weissenberg number problem persists, leading to numerical instabilities that must be mitigated by stabilization strategies such as the log-conformation formulation [55] or stress-diffusion regularization [56]. The EVP constitutive law also couples

elastic stresses, which must remain symmetric positive definite, with plastic stresses governed by a yield criterion, and enforcing both conditions within a finite element setting is delicate and can require projection or energy-stable reformulations. Moreover, EVP flows naturally involve moving yield surfaces, which act as free boundaries between yielded and unyielded regions; capturing these interfaces requires refined meshes and often adaptive refinement, significantly increasing computational cost. The fully coupled FEM systems are large, ill-conditioned non-linear saddle point problems where robust preconditioners are still lacking, and iterative methods must often combine Newton–Krylov or semi-smooth Newton strategies with augmented Lagrangian approaches. Finally, the EVP model is thermodynamically consistent, dissipating energy through viscous and plastic effects, but numerical schemes may violate this structure unless care is taken to design energy-dissipative time-stepping schemes [57]. Altogether, FEM for Oldroyd-B and Bingham EVP fluids is challenging because it combines the two hardest aspects of viscoelastic and viscoplastic flows: high Weissenberg number instabilities and yield-surface localization, demanding stabilization, robust solvers, and carefully chosen approximation spaces. Our objective within this framework is to approximate the velocity, pressure, and elastic stresses in space where we utilize a higher order finite element method for the velocity-stress approximation and incorporate a discontinuous pressure element. This specific combination of elements has demonstrated exceptional effectiveness in accurately capturing the behavior of both Oldroyd-B and Bingham fluids, including nonlinear viscosity functions [58]. Before presenting the weak form of the problem, let us introduce the Lebesgue and Sobolev spaces:

$$L^2(\Omega) = \left\{ u : \Omega \to \mathbb{R} \;\middle|\; \int_\Omega |u(x)|^2 \, dx < \infty \right\}, \tag{3.65}$$

$$H^1(\Omega) = \left\{ u \in L^2(\Omega) \;\middle|\; \frac{\partial u}{\partial x_i} \in L^2(\Omega),\ i = 1, \ldots, 2 \right\}, \tag{3.66}$$

$$H_0^1(\Omega) = \left\{ u \in H^1(\Omega) \;\middle|\; u = 0 \text{ on } \partial\Omega \right\}. \tag{3.67}$$

We introduce the functional spaces $\boldsymbol{S} := L^2(\Omega)^{d\times d}_{\mathbf{sym}}$, $\boldsymbol{V} := [H_0^1(\Omega)]^d$, and $Q := L_0^2(\Omega)$ in which the stress velocity and pressure reside respectively [59]. Here, $[H_0^1(\Omega)]^2$ denotes the space of square-integrable velocities defined on the domain Ω, vanishing on the boundary and with first derivatives also square-integrable, $L_0^2(\Omega)$ denotes the space of square integrable functions with zero average, and $(L^2(\Omega))^{2\times 2}_{\text{sym}}$ representing

the space of 2×2 symmetric tensors whose components are square integrable. The variational form is then derived using the test functions $\boldsymbol{s} \in \boldsymbol{S}$, $\boldsymbol{v} \in \boldsymbol{V}$ and $q \in Q$ and then multiply them with equation (2.33) over the domain Ω with respect to the spatial coordinates $\boldsymbol{x} = (x_1, x_2)$ and do the integration. The weak form is then read as: Find $(\boldsymbol{u}, \boldsymbol{\sigma}, p) \in \boldsymbol{X} = \boldsymbol{S} \times \boldsymbol{V} \times Q$ such that:

$$\begin{cases} \displaystyle\int_\Omega \left[\lambda\left(\boldsymbol{u}\cdot\nabla\boldsymbol{\sigma} - \nabla u\cdot\boldsymbol{\sigma} - \boldsymbol{\sigma}\cdot\nabla\boldsymbol{u}^T\right) + f(\boldsymbol{\sigma})\boldsymbol{\sigma} - 2\eta_m\boldsymbol{D}(\boldsymbol{u})\right]\boldsymbol{s}\,d\boldsymbol{x} = 0 \quad \forall\,\boldsymbol{s}\in\boldsymbol{S}, \\ \displaystyle\int_\Omega \left[\rho\left(\boldsymbol{u}\cdot\nabla\boldsymbol{u}\right) - \nabla\cdot\left(-p\mathbf{I} + 2\eta(\mathrm{II}(D))\boldsymbol{D}(\boldsymbol{u}) + \boldsymbol{\sigma}\right)\right]\boldsymbol{v}\,d\boldsymbol{x} = 0 \quad \forall\,\boldsymbol{v}\in\boldsymbol{V}, \\ \displaystyle\int_\Omega (\nabla\cdot\boldsymbol{u})\,q\,d\boldsymbol{x} = 0 \quad \forall\,q\in Q, \end{cases} \tag{3.68}$$

further integrating by parts yields:

$$\begin{cases} \displaystyle\int_\Omega \left[\lambda\Big((\boldsymbol{u}\cdot\nabla)\boldsymbol{\sigma} - (\nabla\boldsymbol{u})\cdot\boldsymbol{\sigma} - \boldsymbol{\sigma}\cdot(\nabla\boldsymbol{u})^T\Big) + f(\boldsymbol{\sigma})\boldsymbol{\sigma}\right] : \boldsymbol{s}\,d\boldsymbol{x} \\ \qquad - \ 2\eta_m\displaystyle\int_\Omega \boldsymbol{D}(\boldsymbol{u}) : \boldsymbol{s}\,d\boldsymbol{x} = 0 \qquad\qquad \forall\,\boldsymbol{s}\in\boldsymbol{S}, \\ \displaystyle\int_\Omega \rho(\boldsymbol{u}\cdot\nabla\boldsymbol{u})\cdot\boldsymbol{v}\,d\boldsymbol{x} + 2\int_\Omega \eta\big(\mathrm{II}(D)\big)\,\boldsymbol{D}(\boldsymbol{u}) : \boldsymbol{D}(\boldsymbol{v})\,d\boldsymbol{x} \\ \qquad - \displaystyle\int_\Omega p\,\nabla\cdot\boldsymbol{v}\,d\boldsymbol{x} + \int_\Omega \boldsymbol{\sigma} : \boldsymbol{D}(\boldsymbol{v})\,d\boldsymbol{x} = 0 \qquad\qquad \forall\,\boldsymbol{v}\in\boldsymbol{V}, \\ \displaystyle\int_\Omega (\nabla\cdot\boldsymbol{u})\,q\,d\boldsymbol{x} = 0 \qquad\qquad \forall\,q\in Q. \end{cases} \tag{3.69}$$

Introducing here a pair of finite dimensional approximation spaces, which are given as $\boldsymbol{S}_h = \mathrm{span}\{\chi_1, \ldots, \chi_Z\}$, $\boldsymbol{V}_h = \mathrm{span}\{\psi_1, \ldots, \psi_N\}$ and $Q_h = \mathrm{span}\{\varphi_1, \ldots, \varphi_M\}$. The discretized solution is decomposed as follows:

$$\boldsymbol{u}_h = \sum_{i=1}^{N} \boldsymbol{u}_i\psi_i, \quad p_h = \sum_{j=1}^{M} p_j\varphi_j, \quad \boldsymbol{\sigma}_h = \sum_{k=1}^{Z} \boldsymbol{\sigma}_k\chi_k, \tag{3.70}$$

finally, the discrete system of equations to be solved can be expressed as a typical saddle point problem:

$$\underbrace{\begin{pmatrix} \mathcal{F} & \mathcal{M} & \mathcal{B} \\ \mathcal{H} & \mathcal{L} & 0 \\ \mathcal{B}^T & 0 & 0 \end{pmatrix}}_{\boldsymbol{A}} \underbrace{\begin{pmatrix} \boldsymbol{u} \\ \boldsymbol{\sigma} \\ p \end{pmatrix}}_{\boldsymbol{x}} = \underbrace{\begin{pmatrix} r_u \\ r_\sigma \\ r_p \end{pmatrix}}_{\mathbf{b}}, \tag{3.71}$$

with

$$\begin{aligned}
\mathcal{F} = f_{ij} &= \rho \int_\Omega \big((\boldsymbol{\psi}_j \cdot \nabla)\boldsymbol{\psi}_i\big) \cdot \boldsymbol{\psi}_i \, d\boldsymbol{x} \\
&\quad + 2 \int_\Omega \eta\big(\mathrm{II}(D)\big)\, \boldsymbol{D}(\boldsymbol{\psi}_j) : \boldsymbol{D}(\boldsymbol{\psi}_i) \, d\boldsymbol{x}, \quad \forall\, i,j = 1,\dots,N, \\
\mathcal{M} = m_{ij} &= \int_\Omega \boldsymbol{\chi}_j : \boldsymbol{D}(\boldsymbol{\psi}_i) \, d\boldsymbol{x} \quad \forall\, i = 1,\dots,N,\ j = 1,\dots,Z, \\
\mathcal{B} = b_{ij} &= -\int_\Omega \varphi_j \, \nabla \cdot \boldsymbol{\psi}_i \, d\boldsymbol{x} \quad \forall\, i = 1,\dots,N,\ j = 1,\dots,M, \\
\mathcal{H} = h_{ij} &= -2\eta_m \int_\Omega \boldsymbol{D}(\boldsymbol{\psi}_j) : \boldsymbol{\chi}_i \, d\boldsymbol{x} \quad \forall\, i = 1,\dots,Z,\ j = 1,\dots,N, \\
\mathcal{L} = l_{ij} &= \lambda \int_\Omega \Big((\boldsymbol{u} \cdot \nabla)\boldsymbol{\chi}_j - (\nabla \boldsymbol{u}) \cdot \boldsymbol{\chi}_j - \boldsymbol{\chi}_j \cdot (\nabla \boldsymbol{u})^T\Big) : \boldsymbol{\chi}_i \, d\boldsymbol{x} \\
&\quad + \int_\Omega f(\boldsymbol{\sigma})\, \boldsymbol{\chi}_j : \boldsymbol{\chi}_i \, d\boldsymbol{x}, \quad \forall\, i,j = 1,\dots,Z.
\end{aligned}$$

In the context of the finite element method (FEM) applied to Equation (2.33), the choice of spaces for velocity, pressure, and stress variables is crucial for achieving accurate and stable numerical solutions. The selection of these spaces is motivated by various considerations, including the mathematical properties of the problem, the desired accuracy of the approximation, and computational efficiency. In particular, the choice of the above finite-dimensional spaces for velocity and pressure is subjected to the LBB condition [60], where its discrete version reads:

$$\sup_{0 \neq \boldsymbol{u} \in \boldsymbol{V}_h} \frac{\int_\Omega (\nabla \cdot \boldsymbol{u}) q \, d\boldsymbol{x}}{\|\boldsymbol{u}\|_{1,\Omega}} \geq \alpha \|q\|_{0,\Omega} \quad \forall \quad q \in Q_h, \tag{3.72}$$

concerning the approximated spaces $\boldsymbol{V}_h$ and $\boldsymbol{S}_h$ a similar kind of condition has been studied in [15] and this is subjected to more complex analysis (applied only if solvent viscosity is zero)

$$\sup_{0\neq\boldsymbol{\sigma}\in\boldsymbol{S}_h} \frac{\int_\Omega (\nabla\cdot\boldsymbol{\sigma})\boldsymbol{u}\, d\boldsymbol{x}}{\|\boldsymbol{\sigma}\|_{0,\Omega}} \geq \gamma\|\boldsymbol{u}\|_{1,\Omega} \quad \forall \quad \boldsymbol{u}\in\boldsymbol{V}_h. \tag{3.73}$$

On a reference quadrilateral element $T \subset \mathbb{R}^2$, the bi-quadratic polynomial space is

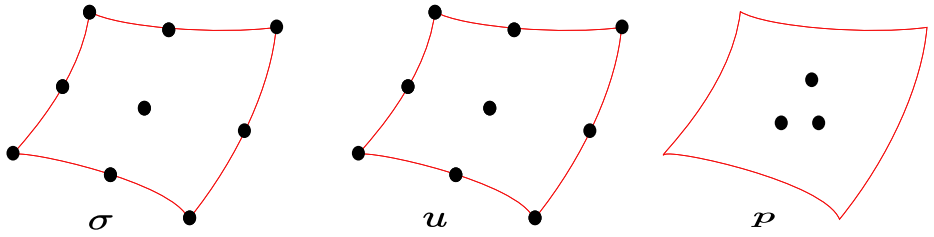

FIGURE 3.4: $\mathbb{Q}_2/\mathbb{P}_1$ element for velocity/stress and pressure.

defined as

$$\mathbb{Q}_2(\mathcal{T}) = \left\{ q(x,y) \ : \ q(x,y) = \sum_{i=0}^{2}\sum_{j=0}^{2} a_{ij}x^i y^j, \ a_{ij}\in\mathbb{R} \right\}. \tag{3.74}$$

When assembled over the mesh, the corresponding global finite element space is taken to be continuous across element interfaces, i.e., Q_2 refers to the space of continuous bi-quadratic polynomials on quadrilaterals. Similarly, on a triangular (or quadrilateral) element T, the linear polynomial space is defined as

$$\mathbb{P}_1(\mathcal{T}) = \{ q(x,y) \ : \ q(x,y) = a + bx + cy, \ a,b,c\in\mathbb{R} \}. \tag{3.75}$$

In the present formulation, $\mathbb{P}_1$ is considered in its discontinuous form, i.e., piecewise linear polynomials that are not enforced to be continuous across element boundaries. Hence, the pair $\mathbb{Q}_2/\mathbb{P}_1$ corresponds to the use of continuous bi-quadratic basis functions for velocity/stress and discontinuous piecewise linear basis functions for pressure, which is a classical stable mixed finite element pair for incompressible flow problems [15]. To achieve high accuracy and efficiency in approximating $(\boldsymbol{\sigma}, \boldsymbol{u}, p)$,

we discretize the solutions in the following discrete spaces:

$$\boldsymbol{S}_h = \{\boldsymbol{s}_h \in \boldsymbol{S} \mid \boldsymbol{s}_{h|\mathcal{T}} \in (\mathbb{Q}_2(\mathcal{T}))^{2\times 2} \text{ for all } \mathcal{T} \in \mathcal{T}_h\}, \tag{3.76}$$

$$\boldsymbol{V}_h = \{\boldsymbol{v}_h \in \boldsymbol{V} \mid \boldsymbol{v}_{h|T} \in (\mathbb{Q}_2(\mathcal{T}))^2 \text{ for all } T \in \mathcal{T}_h, \boldsymbol{v}_{h|\partial\Omega_h} = 0\}, \tag{3.77}$$

$$Q_h = \{q_h \in Q \mid q_{h|\mathcal{T}} \in \mathbb{P}_1(\mathcal{T}) \text{ for all } \mathcal{T} \in \mathcal{T}_h\}. \tag{3.78}$$

This pair satisfies the LBB condition, making it a robust choice for elastoviscoplastic flow simulations. Further

$$\|\boldsymbol{u} - \boldsymbol{u}_h\|_{1,\Omega} = \mathcal{O}(h^2), \qquad \|p - p_h\|_{0,\Omega} = \mathcal{O}(h), \tag{3.79}$$

demonstrating quadratic convergence for the velocity in the H^1-norm and linear convergence for the pressure in the L^2-norm, which matches the expected order of the polynomial degrees.

3.4 Stabilization Tecchniques

3.4.1 Artificial Diffusion Stabilization

The non-linear system introduced earlier in Equation (3.71) contains a dominant non-linear behavior stemming from the operator block $\mathcal{L}$. This block includes the advective term $(\boldsymbol{u} \cdot \nabla)\boldsymbol{\sigma}$ and lacks a diffusive regularization mechanism, unlike the velocity equation (represented by block $\mathcal{F}$), which includes a symmetric, coercive differential operator. To improve numerical stability, particularly in convection dominated scenarios, it is beneficial to augment the $\mathcal{L}$ block with an artificial diffusion term modeled by the Laplacian operator. This results in the modified block system:

$$\underbrace{\begin{pmatrix} \mathcal{F} & \mathcal{M} & \mathcal{B} \\ \mathcal{H} & \mathcal{L} + \mathcal{L}_{\boldsymbol{\sigma}} & 0 \\ \mathcal{B}^T & 0 & 0 \end{pmatrix}}_{\mathcal{A}_{\text{stab}}} \begin{pmatrix} \boldsymbol{u} \\ \boldsymbol{\sigma} \\ p \end{pmatrix} = \begin{pmatrix} r_{\boldsymbol{u}} \\ r_{\boldsymbol{\sigma}} \\ r_p \end{pmatrix}. \tag{3.80}$$

Here, $\mathcal{L}_{\boldsymbol{\sigma}}$ denotes the artificial diffusion operator introduced to regularize the $\boldsymbol{\sigma}$-equation. It is defined as:

$$\mathcal{L}_{\boldsymbol{\sigma}}(\boldsymbol{\sigma}) := -h_\gamma \Delta \boldsymbol{\sigma}, \tag{3.81}$$

where h_γ is a stabilization parameter that controls the amount of added diffusion. To preserve consistency with the original system in the limit of mesh refinement, this parameter is chosen such that

$$\lim_{h \to 0} h_\gamma = 0. \tag{3.82}$$

This diffusion serves to suppress numerical instabilities caused by the hyperbolic nature of the advection term in $\mathcal{L}$, particularly under coarse discretizations or high Weissenberg number regimes. However, it does not constitute a variationally consistent stabilization. Hence, although $\mathcal{L}_{\boldsymbol{\sigma}}$ improves robustness, especially for moderate mesh resolutions, it must eventually be complemented by edge-based stabilization techniques such as those introduced in the previous section.

3.4.2 EO-FEM stabilization

To enhance stability, especially in convection dominated regimes and to satisfy the inf-sup condition, a consistent edge-based stabilization technique is applied. Following the approach of Bonito and Burman [61], a jump penalty term is added over inter-element edges E, defined as

$$J_u = \sum_E \max(\gamma_h h_E, \gamma^* h_E^2) \int_E |\nabla \boldsymbol{u}| : |\nabla \boldsymbol{v}| \, ds, \tag{3.83}$$

which penalizes the discontinuity in the solution gradient. A similar term is added to the stress equation to ensure the robustness of the stress approximation space:

$$J_{\boldsymbol{\sigma}} = \sum_E \gamma \, h_E^2 \int_E \left[\nabla \boldsymbol{\sigma}\right] : \left[\nabla \chi\right] \mathrm{d}s, \tag{3.84}$$

where $[\nabla \boldsymbol{\chi}] = \nabla \chi^+ - \nabla \chi^-$ denotes the jump across adjacent elements, and γ is a mesh-independent stabilization parameter. Incorporating these stabilizations into

the discretized finite element system yields the modified block matrix formulation:

$$\underbrace{\begin{pmatrix} \mathcal{F} + \boldsymbol{J_u} & \mathcal{M} & \mathcal{B} \\ \mathcal{H} & \mathcal{L} + \boldsymbol{J_\sigma} & 0 \\ \mathcal{B}^T & 0 & 0 \end{pmatrix}}_{\mathcal{A}_{\text{stab}}} \begin{pmatrix} \boldsymbol{u} \\ \boldsymbol{\sigma} \\ p \end{pmatrix} = \begin{pmatrix} r_{\boldsymbol{u}} \\ r_{\boldsymbol{\sigma}} \\ r_p \end{pmatrix}. \tag{3.85}$$

Here, $\boldsymbol{J_u}$ and $\boldsymbol{J_\sigma}$ are the jump stabilization matrices applied respectively to the velocity and stress equations. These ensure consistency and stability without altering the solution in the limit of mesh refinement. The edge-based structure of $\boldsymbol{J}_\sigma$ introduces additional couplings between degrees of freedom across adjacent elements, requiring an extended finite element stencil. This technique, referred to as the Edge-Oriented Finite Element Method (EO-FEM).

Remark 3.1. Although none of the stabilization techniques discussed above were utilized in this study, the two mentioned methods could be considered for future implementation.

Chapter 4

Numerical Solver

This chapter discusses the computational framework for solving the non-linear algebraic system generated by discretization of finite elements of elastoviscoplastic flow equations. The resulting formulation captures the material's complex rheological behavior exhibiting mixed parabolic and hyperbolic characteristics arising from the interplay between viscous dissipation, elastic stress evolution, and yielding phenomena. Unlike conventional Newtonian fluids, the numerical treatment must simultaneously address a few fundamental challenges: the hyperbolic nature of stress transport equations, the parabolic character of momentum diffusion, and the non-linear threshold condition governing the yield transition. The solution to these challenges is discussed in the following sections.

4.1 Introduction

The non-linear systems of equations introduced in Chapter 3 present strong computational issues, in particular with respect to very non-linear constitutive laws and the yield stress effects. Solving such systems requires robust and efficient iterative methods to ensure convergence and numerical stability. There are several classical methods for solving non-linear algebraic systems of the form $\boldsymbol{A}\boldsymbol{x} = \boldsymbol{b}$, including the fixed-point iteration and the Newton–Raphson method. Fixed-point (or Picard-type) iterative methods are widely employed in the numerical solution of non-linear

systems due to the simplicity and ease of implementation present in the mentioned methods. One of their principal advantages lies in the fact that they rely solely on the evaluation of the non-linear function, without the need to compute its Jacobian or other derivative information, which is particularly beneficial in large scale or complex systems [62, 63]. However, they suffer from slow convergence and are typically conditionally convergent depending on the Lipschitz continuity of the non-linear operator. As such, they often require fine time stepping or relaxation, especially for problems with strong non-linearities or near-yield surfaces [64, 65]. On the other hand, the Newton–Raphson method offers local quadratic convergence under the assumption that the Jacobian is non singular and the initial guess is sufficiently close to the true solution [66]. This makes Newton's method particularly appealing for time-independent steady-state problems or quasi-steady simulations, where high accuracy and convergence efficiency are crucial. The primary computational cost in Newton's method lies in assembling and solving the linearized system involving the Jacobian, which we address through sparse direct solvers and consistent Jacobian approximations. However, Newton's method also requires caution. For high Reynolds number flows or strongly non-linear regimes, such as those involving Bingham type fluids, the Newton iteration may not converge globally and can become unstable if the solution update steps are too large. To mitigate this, we incorporate a damping strategy based on line search method, which dynamically adjusts the update step size by minimizing a merit function associated with the residual norm. This approach guarantees the global convergence of the Newton iteration even in the presence of sharp yield surfaces or discontinuities in the stress field [67, 68]. Therefore, despite the existence of other methods, the Newton–Raphson approach is preferred in this study due to its superior convergence properties and its suitability for the nonlinearities encountered in regularized elastoviscoplastic flows. The efficiency and the stability of the method are further reinforced by the use of an inexact Jacobian, optimal damping factors, and robust linear solvers, making it a reliable choice for the present simulations.

4.2 Newton Method

Let $\boldsymbol{r}(\boldsymbol{x})$ denote the residual vector resulting from the discretized momentum, continuity, and constitutive equations. The non-linear discretized system to be solved takes the form:

$$\boldsymbol{r}(\boldsymbol{x}^\ell) := \boldsymbol{A}\boldsymbol{x}^\ell - \boldsymbol{b} = \boldsymbol{0}, \tag{4.1}$$

where the operator $\boldsymbol{A}$ encapsulates all non-linear contributions due to inertia, pressure-velocity coupling, and the regularized constitutive law. To solve this system, we employ the damped Newton Raphson method with line search. The Newton iteration is based on approximating the Jacobian matrix $J(\boldsymbol{x}^l) = \dfrac{\partial \boldsymbol{r}}{\partial \boldsymbol{x}}\boldsymbol{x}^l$ using analytical divided differences, allowing for efficient yet consistent evaluation of non-linear sensitivities. Each Newton step requires solving a linearized system of the form:

$$\boldsymbol{J}(\boldsymbol{x}^\ell)\delta\boldsymbol{x}^\ell = \boldsymbol{r}(\boldsymbol{x}^\ell), \tag{4.2}$$

where $\delta\boldsymbol{x}^\ell$ is the Newton update and $\boldsymbol{x}^\ell$ is the current iterate. The jacobian is represented as

$$\boldsymbol{J}_{ij} \approx \frac{r_i(\boldsymbol{x} + h\boldsymbol{e}_j) - r_i(\boldsymbol{x} - h\boldsymbol{e}_j)}{2h}, \tag{4.3}$$

where $\boldsymbol{e}_j$ is the unit vector in the j-th direction, h is a small perturbation parameter (step size), and $r_i(\boldsymbol{x})$ is the i-th component of the residual vector $\boldsymbol{r}(\boldsymbol{x})$ and h is the step size. Due to strong non-linearities (particularly the stress transport and the viscosity regularization near the yield surface), the undamped Newton iteration may diverge if the initial guess is not sufficiently close to the solution. To stabilize convergence, we employ a damping (line search) strategy, The updated solution is computed as:

$$\boldsymbol{x}^{\ell+1} = \boldsymbol{x}^\ell - \omega^\ell \delta\boldsymbol{x}^\ell, \tag{4.4}$$

where $\omega^\ell \in (-1, 0]$ [69] is an optimal damping parameter chosen via a line search strategy to ensure convergence, especially in regions of high non-linearity near the yield surface.

Algorithm 1 Newton Method

Input: Initial guess $\boldsymbol{x}^0$, tolerance ε
Set $\ell = 0$
while $\|\boldsymbol{r}(\boldsymbol{x}^\ell)\| > \varepsilon$ **do**
    Evaluate residual: $\boldsymbol{r}(\boldsymbol{x}^\ell)$
    Assemble approximate Jacobian $\boldsymbol{J}(\boldsymbol{x}^\ell)$ via divided differences
    Solve: $\boldsymbol{J}(\boldsymbol{x}^\ell)\delta\boldsymbol{x}^\ell = \boldsymbol{r}(\boldsymbol{x}^\ell)$
    Perform line search to compute damping factor $\omega^\ell \in (-1, 0]$
    Update: $\boldsymbol{x}^{\ell+1} = \boldsymbol{x}^\ell - \omega^\ell \delta\boldsymbol{x}^\ell$
    $\ell \leftarrow \ell + 1$
end while

Newton's method is very popular in numerical analysis community because it usually converges fast. It can be shown that

$$\|x^{(k+1)} - \bar{x}\| \leq C\|x^{(k)} - \bar{x}\|^2$$

when $x^{(k)}$ is quite close to $\bar{x}$. From the above relation we see that the asymptotic rate of convergence is quadratic, which is very fast for any numerical method.

4.3 Linear Solver in Newton Framework

The most computationally intensive component within each Newton iteration for solving the non-linear system is the linear subproblem involving the Jacobian matrix.

$$\boldsymbol{J}(\boldsymbol{x})\,\delta\boldsymbol{x} = \boldsymbol{r}(\boldsymbol{x}) \tag{4.5}$$

The Jacobian $\boldsymbol{J}$, typically sparse due to the finite element discretization of the coupled elastoviscoplastic and Navier-Stokes equations, must be solved repeatedly, choosing a linear solver critical for computational efficiency and scalability. When memory permits, sparse direct solvers are preferred for their robustness and accuracy. In this work, we employ the UMFPACK (Unsymmetric MultiFrontal Package)

library, which performs LU factorization with minimal fill-in and is optimized for unsymmetric sparse systems [70, 69]. This ensures reliable and efficient linear solves in memory-rich environments.

For large scale problems or platforms with limited memory, iterative solvers provide a more scalable alternative. Krylov subspace methods such as BiCG, BiCGSTAB, and GMRES, along with classical ILU-preconditioned schemes and ADI splitting methods, are widely used. However, their performance may be hindered by slow convergence in stiff systems and a strong dependence on effective preconditioning.

To address these challenges, multigrid methods offer an optimal and scalable solution. It belongs to a class of fastest linear iterations, as the convergence rate is bounded indeopndently of the step size [71]. In a multigrid approach, the solution process alternates between grids of different resolutions. High-frequency errors are smoothed out on fine grids using simple iterative methods, while low-frequency errors are transferred to coarser grids where they can be corrected more efficiently. After correction on the coarse grid, the solution is interpolated back to the fine grid, and additional smoothing is applied. In our implementation, we employ a geometric multigrid strategy based on successive grid coarsening. A standard V-cycle or F-cycle governs the inter level traversal, facilitating efficient error reduction across both fine and coarse grids. A key feature of the multigrid implementation is the use of a block based Vanka type smoother. This smoother operates by solving small, coupled systems locally on each element or control volume. Specifically, the update formula for the local system for each element is given by

$$\begin{pmatrix} \boldsymbol{u}^{l+1} \\ \boldsymbol{\sigma}^{l+1} \\ p^{l+1} \end{pmatrix} = \begin{pmatrix} \boldsymbol{u}^{l} \\ \boldsymbol{\sigma}^{l} \\ p^{l} \end{pmatrix} + \omega^{l} \sum_{\mathcal{T} \in \mathcal{T}_h} [\boldsymbol{J}]^{-1}_{|\mathbf{T}} \begin{pmatrix} r_{\boldsymbol{u}} \\ r_{\boldsymbol{\sigma}} \\ r_{p} \end{pmatrix}_{|\mathbf{T}} , \tag{4.6}$$

where the summation signifies an element-wise assembly procedure. The local inverse of the Jacobian restricted to each element is efficiently computed using a direct solver (e.g., LAPACK), particularly for 2D blocks of moderate size (e.g., 48×48). This localized smoothing ensures strong coupling between velocity, pressure, and stress variables, while maintaining computational tractability. Following pre-smoothing, the smoothed error is transferred to the next coarser level using a

restriction operator. There, the error equation $\boldsymbol{J}(\boldsymbol{x}^n)\boldsymbol{e}_{2h} = \boldsymbol{r}(\boldsymbol{x}^n)$ is solved recursively until the coarsest level is reached. On this coarsest grid, the residual equation is solved using UMFPACK to minimize memory consumption while maintaining solver robustness. The prolongation operation subsequently interpolates the error correction back to finer grids, followed by post-smoothing to damp high-frequency error components introduced during interpolation [69].

In conclusion, by integrating UMFPACK as a coarse grid solver within a multigrid framework and utilizing localized Vanka type smoothing, we achieve an effective and scalable linear solver strategy tailored for the Newton-based solution of non-linear systems with elastoviscoplastic behavior. This hybrid strategy effectively balances memory usage, convergence speed, and implementation complexity. Below are the algorithms for geometric V W and F multigrid cycles.

Terms used in algorithm.

- R: fine to coarse transfer operator for residuals (restriction).
- P: coarse to fine transfer operator for corrections (prolongation/interpolation).
- Smooth$(\cdot)$: a local relaxation scheme applied at each grid level.
- ν_1, ν_2: counts of smoothing sweeps before and after the coarse grid correction.
- L: index of the coarsest level in the hierarchy.

Algorithm 2 V-cycle (visit the coarse grid once)

procedure V-Cycle($\ell, A_\ell, u_\ell, f_\ell$) ▷ ℓ=0 finest, L coarsest
  if $\ell = L$ **then**
    $u_\ell \leftarrow$ CoarseSolve(A_ℓ, f_ℓ) ▷ solve the smallest problem
    return u_ℓ
  end if
  for $i = 1$ **to** ν_1 **do**
    $u_\ell \leftarrow$ Smooth(A_ℓ, u_ℓ, f_ℓ) ▷ reduce fast/oscillatory error
  end for
  $r_\ell \leftarrow f_\ell - A_\ell u_\ell$ ▷ how wrong we still are
  $f_{\ell+1} \leftarrow R_\ell^{\ell+1} r_\ell$ ▷ send that error to coarse level
  $e_{\ell+1} \leftarrow 0$
  $e_{\ell+1} \leftarrow$ V-Cycle(ℓ+1, $A_{\ell+1}, e_{\ell+1}, f_{\ell+1}$) ▷ solve for coarse error
  $u_\ell \leftarrow u_\ell + P_{\ell+1}^\ell e_{\ell+1}$ ▷ bring correction back
  for $i = 1$ **to** ν_2 **do**
    $u_\ell \leftarrow$ Smooth(A_ℓ, u_ℓ, f_ℓ) ▷ clean up new oscillations
  end for
  return u_ℓ
end procedure

(V-cycle): First step is to improve the guess a little, also known as pre-smooth. Measure the residual occurring and use the coarse grid to fix it, this step is known as restrict. Now the next step is prolongation, solve that coarse problem once, bring the fix back, after this a post smooth step helps improve more. This is fast and usually enough for well behaved cases.

Algorithm 3 W-cycle (visit the coarse grid twice for a stronger correction)

procedure W-CYCLE($\ell, A_\ell, u_\ell, f_\ell$)
  if $\ell = L$ **then**
    $u_\ell \leftarrow \text{CoarseSolve}(A_\ell, f_\ell)$
    return u_ℓ
  end if
  for $i = 1$ **to** ν_1 **do**
    $u_\ell \leftarrow \text{Smooth}(A_\ell, u_\ell, f_\ell)$
  end for
  $r_\ell \leftarrow f_\ell - A_\ell u_\ell, \quad f_{\ell+1} \leftarrow R_\ell^{\ell+1} r_\ell$
  $e_{\ell+1}^{(1)} \leftarrow 0; \quad e_{\ell+1}^{(1)} \leftarrow \text{W-Cycle}(\ell{+}1, A_{\ell+1}, e_{\ell+1}^{(1)}, f_{\ell+1})$
  $e_{\ell+1}^{(2)} \leftarrow 0; \quad e_{\ell+1}^{(2)} \leftarrow \text{W-Cycle}(\ell{+}1, A_{\ell+1}, e_{\ell+1}^{(2)}, f_{\ell+1})$
  $u_\ell \leftarrow u_\ell + P_{\ell+1}^{\ell}\big(e_{\ell+1}^{(1)} + e_{\ell+1}^{(2)}\big)$
  for $i = 1$ **to** ν_2 **do**
    $u_\ell \leftarrow \text{Smooth}(A_\ell, u_\ell, f_\ell)$
  end for
  return u_ℓ
end procedure

(W-cycle): Same as the above mentioned V-cycle, but the coarse grid is called twice before coming back. Obviously the cost will be high but is safer when the problem is complex (e.g., strong coupling, high Reynolds number).

Algorithm 4 F-cycle (full multigrid / FMG: build a good initial solution from coarse to fine)

procedure FMG($\{A_\ell\}_{\ell=0}^{L},\ \{f_\ell\}_{\ell=0}^{L}$)
  $u_L \leftarrow \text{CoarseSolve}(A_L, f_L)$ ▷ solve the coarsest grid first
  for $\ell = L-1$ **down to** 0 **do**
    $u_\ell \leftarrow P_{\ell+1}^{\ell}\, u_{\ell+1}$ ▷ interpolate solution up one level
    for $j = 1$ **to** k **do** ▷ $k = 1$ or 2 V-cycles to polish
      $u_\ell \leftarrow \text{V-Cycle}(\ell, A_\ell, u_\ell, f_\ell)$
    end for
  end for
  return u_0
end procedure

(F-cycle): Start at the very coarse grid and helps getting a cheap but global solution. Move one level finer, interpolate that solution, and run one or two quick V-cycles to polish it. Repeat until the finest grid. F-cycle gives a high quality starting guess and often reaches the final accuracy in very few cycles.

4.4 Solver Behaviour

4.4.1 Flow Around Cylinder

Case I: Navier Stokes

$$\begin{cases} \rho\,(\boldsymbol{u}\cdot\nabla\boldsymbol{u}) - \nabla\cdot(-p\boldsymbol{I} + 2\eta\boldsymbol{D}(\boldsymbol{u})) = 0, \\ \nabla\cdot\boldsymbol{u} = 0. \end{cases} \tag{4.7}$$

We consider a two-dimensional incompressible flow in a channel with a circular obstacle. It can be seen in Figure 5.14 The computational domain is defined as

$$\Omega = [0, 2.2] \times [0, 0.41] \setminus B_r(0.2, 0.2), \tag{4.8}$$

where $B_r(0.2, 0.2)$ is a circular disc of radius $r = 0.05$, centered at $(0.2, 0.2)$. The no-slip condition is enforced on the top and bottom channel walls and along the surface of the circular obstacle:

$$\boldsymbol{u} = 0 \quad \text{on } \Gamma_{\text{walls}} = ([0, 2.2] \times \{0, 0.41\}) \cup \partial B_r(0.2, 0.2). \tag{4.9}$$

A parabolic inflow profile is imposed on the left boundary $\Gamma_{\text{in}} = \{0\} \times [0, 0.41]$:

$$\boldsymbol{u}(0, y) = \left(\frac{4Uy(0.41 - y)}{0.41^2}, 0 \right), \quad U = 0.3. \tag{4.10}$$

At the outlet $\Gamma_{\text{out}} = \{2.2\} \times [0, 0.41]$, we apply a do nothing outflow condition:

$$\nu \frac{\partial \boldsymbol{u}}{\partial \eta} - p\eta = 0, \tag{4.11}$$

with η denoting the outward normal. The mean velocity corresponding to the parabolic inflow is computed as

$$U_{\text{mean}} = \frac{2}{3} U = 0.2, \tag{4.12}$$

and the characteristic length is taken as the obstacle diameter $L = 2r = 0.1$. Thus, the Reynolds number is given by

$$Re = \frac{U_{\text{mean}} L}{\nu} = \frac{0.2 \cdot 0.1}{0.001} = 20, \tag{4.13}$$

which indicates a low Reynolds number regime, appropriate for laminar incompressible flow studies.

TABLE 4.1: Drag and Lift Coefficients (C_D and C_L) for Flow Around a Cylinder at Re = 20. NOE represents the number of elements, and DOF represents the degrees of freedom.

Level	NOE	DOF	C_D	C_L	N/L
1	520	5,928	5.55503	0.00950	9/3
2	2,080	23,296	5.57224	0.01060	3/1
3	8,320	92,352	5.57762	0.01063	2/1
4	33,280	367,744	5.57906	0.01061	2/1
5	133,220	1,467,648	5.57945	0.01062	1/2

From Table 4.1, it can be seen that the drag coefficient C_D decreases monotonically with increasing grid-refinement level from Level 1 to 5. In the coarsest refined level, the drag coefficient is $C_D = 5.55503$, and it goes up to $C_D = 5.57945$ for the five-level resolution. This behavior validates the grid independence of the numeric solution. The reduction rate of C_D decreases with mesh refinement, which means discretization error can be ignored in the higher resolution. A similar pattern is observed for the lift coefficient C_L, which remains consistently small (as expected for symmetric geometries at low Reynolds numbers), further verifying the physical accuracy of the solution.The number of non-linear (Newton) iterations per level is reported along with the average number of linear (multigrid) iterations per Newton iteration in the last column (N/L). On the coarsest level, convergence is rather slow with 7 Newton iterations, and each of them involves a single multigrid cycle. When the resolution is better, the non-linear solver becomes more favorable, with only 2–3 Newton iterations on intermediate meshes. However, we notice that in the finest mesh, the number of iterations of the Newton method grows slightly (6), which confirms the stifness of the discretized system of equations and the necessity of solving it with higher accuracy. The multigrid solver performs well on all levels, needing just one multigrid cycle per Newton step. This implies the stability of the multigrid preconditioner and also confirms its applicability for solving large systems of linear equations originating from incompressible flow computations. In summary, the presented simulation shows good and physically reasonable results, with satisfying convergence behavior of both the non-linear Newton solver and the linear multigrid solver. The drag coefficient levels off at a value $C_D \approx 5.57945$, perfectly compatible with published reference values of the literature for $Re = 20$ like the ones from Schäfer and Turek [72]. The lift coefficient remains close to zero, as dictated by flow symmetry. The overall solver performance is deemed efficient and reliable for steady-state incompressible flows at moderate Reynolds numbers.

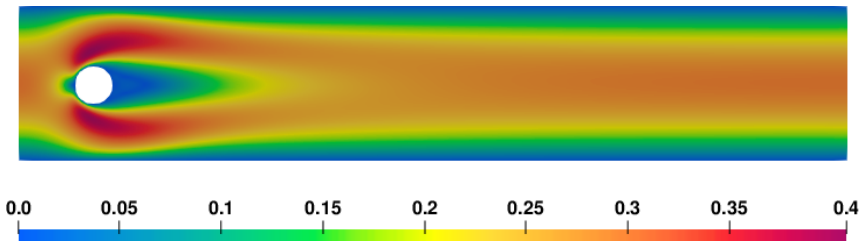

FIGURE 4.1: Newtonian case: Velocity magnitude field at $Re = 20$.

Case II: Viscoelastic

$$\begin{cases} \lambda\left(\boldsymbol{u}\cdot\nabla\boldsymbol{\sigma}-\nabla\boldsymbol{u}\cdot\boldsymbol{\sigma}-\boldsymbol{\sigma}\cdot\nabla\boldsymbol{u}^{T}\right)+\boldsymbol{\sigma}=2\eta_m\boldsymbol{D}(\boldsymbol{u}), \\ \rho\left(\boldsymbol{u}\cdot\nabla\boldsymbol{u}\right)-\operatorname{div}\left(-p\boldsymbol{I}+2\eta_p\boldsymbol{D}(\boldsymbol{u})+\boldsymbol{\sigma}\right)=0, \\ \nabla\cdot\boldsymbol{u}=0. \end{cases} \tag{4.14}$$

TABLE 4.2: Computed drag, lift, non-linear and linear iterations (N/L) at different refinement levels for two Weissenberg numbers.

Level	NOE	DOF	$Wi = 0.002$			$Wi = 0.02$		
			Drag	Lift	N/L	Drag	Lift	N/L
1	520	12480	5.54787	0.00896	7/2	5.58221	0.00822	3/1
2	2080	48880	5.57146	0.01030	3/1	5.60743	0.00955	3/1
3	8320	193440	5.58033	0.01046	2/1	5.61642	0.00970	3/1
4	33280	769600	5.58284	0.01051	3/2	5.61885	0.00974	5/1

Table 4.2 presents the computed drag and lift coefficients for two-dimensional viscoelastic flow around a circular cylinder using the Oldroyd-B model at a fixed Reynolds number of $Re = 20$. Simulations are carried out for two Weissenberg numbers, $Wi = 0.002$ and $Wi = 0.02$, where the Weissenberg number is defined as $Wi = \lambda U/D$, with λ denoting the relaxation time, U the characteristic inflow velocity, and D the diameter of the cylinder. The numerical results are obtained using a Newton-Multigrid solver, and the discretization is done from Level 1 to Level 4. Here, NOE refers to the number of elements, and DOF indicates the total degrees of freedom. The column labeled N/L represents the ratio of the number of Newton iterations (N) to the average number of multigrid cycles per Newton step (L). At low elasticity ($Wi = 0.002$), the drag coefficient shows convergence behavior, increasing slightly from 5.54787 at Level 1 to 5.58284 at Level 4. Similarly, the lift coefficient increases from 0.00896 to 0.01051. These variations are attributed to better resolution of stress boundary layers with mesh refinement. Solver performance remains efficient across refinement levels, with consistent Newton convergence and low average non-linear iterations. As the elasticity is increased to $Wi = 0.02$, both drag and

lift values rise a little, with drag increasing from 5.58221 to 5.61885 and lift from 0.00822 to 0.00974 across the mesh levels. This reflects the greater influence of viscoelastic stress. The solver continues to demonstrate robust convergence, although slightly more non-linear iterations are required, e.g., $N/L = 5/1$ at Level 4. These numerical findings are in agreement with the results of Damanik et al. [73], where the same monolithic Newton-Multigrid approach was applied to incompressible viscoelastic models. These results validates the use of this solver for high Weissenberg number flows, highlighting both stability and accuracy.Figure 4.2 and Figure 4.3 provide qualitative visualization of velocity fields for the two Weissenberg numbers, illustrating the effect of elastic stresses on the flow structure. As expected, at very low Weissenberg numbers, the flow behavior closely resembles that of a Newtonian fluid.

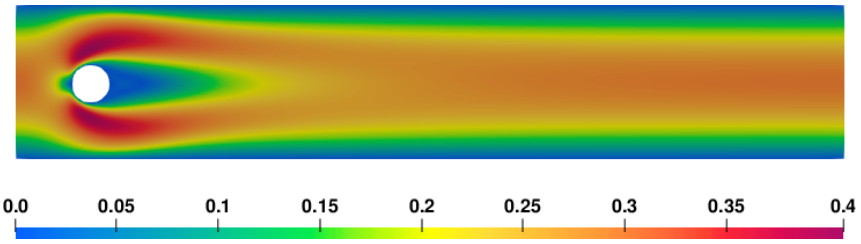

FIGURE 4.2: Viscoelastic case: Velocity magnitude field for $Wi = 0.002$ at $Re = 20$.

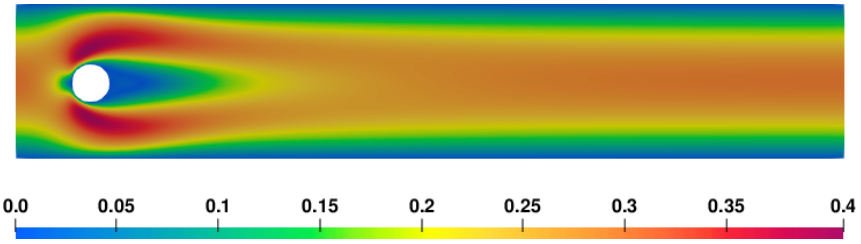

FIGURE 4.3: Viscoelastic case: Velocity magnitude field for $Wi = 0.02$ at $Re = 20$.

Chapter 5

Numerical Results

5.1 Introduction

This chapter presents a series of numerical experiments to validate and observe the performance of the proposed finite element framework and numerical solver for simulating viscoplastic, viscoelastic, and elastoviscoplastic (EVP) fluid flows. The test cases in this chapter cover a range of standard and application oriented problems, increasing in complexity. Each case highlights different physical behaviors and numerical difficulties. We begin with the classical Bingham flow in a two-dimensional channel, which serves to verify the viscoplastic model. Next, we study viscoelastic flow around a confined circular cylinder, where elastic effects dominate and sharp stress variations near boundaries must be handled carefully. We then move on to elastoviscoplastic (EVP) flow through porous media, representing practical situations where elasticity, viscosity, and yield stress all play important roles. Finally, we consider the most advanced case which is the EVP flow around a cylinder, where we compute drag and lift forces under different flow conditions. These numerical experiments confirm that the proposed method is stable, accurate, and capable of capturing key non-linear features such as yield surfaces and stresses.

5.2 Viscoplastic Simulations

5.2.1 Viscoplastic Flow Between Parallel Plates

The initial validation case focuses on the viscoplastic component of the governing system described by equation Equation (2.33). In this setup, the relaxation term and polymer viscosity contributions are ignored to focus on the Bingham viscoplastic behavior. The flow domain is defined as a unit square $\Omega = [0,1] \times [0,1]$, with flow occurring between two parallel plates separated by a distance $h = 1$. The flow is driven by imposing a velocity profile at the left boundary ($x = 0$), while Dirichlet conditions from the analytical solution are applied at the right boundary ($x = 1$). No-slip boundary conditions are enforced on the upper and lower walls, i.e.,

$$u_x(x,0) = u_x(x,1) = 0 \quad \text{for all } x \in [0,1]. \tag{5.1}$$

Assuming steady and unidirectional flow, the velocity field reduces to:

$$\boldsymbol{u} = [u_x(y),\, 0]^T. \tag{5.2}$$

The imposed boundary conditions and unidirectional flow lead to a shear stress distribution varying linearly with y, obtained directly from the momentum balance:

$$\sigma_{xy}(y) = G\left(\frac{1}{2} - y\right), \tag{5.3}$$

where $G = -\partial p/\partial x$ denotes the pressure gradient. The yield stress σ_y partitions the domain into yielded and unyielded regions: shear layers appear near the walls where $|\sigma_{xy}| > \sigma_y$, and a plug region arises around the channel center where $|\sigma_{xy}| < \sigma_y$. The analytical solution for the velocity profile in this configuration is well-established in

the literature [74, 75, 76, 77] and is given by the following piecewise function:

$$u_x(y) = \begin{cases} \frac{1}{8}\left[(1-2\sigma_y)^2 - (1-2\sigma_y-2y)^2\right], & 0 \le y < \frac{1}{2} - \sigma_y, \\ \frac{1}{8}(1-2\sigma_y)^2, & \frac{1}{2} - \sigma_y \le y \le \frac{1}{2} + \sigma_y, \\ \frac{1}{8}\left[(1-2\sigma_y)^2 - (2y-1-2\sigma_y)^2\right], & \frac{1}{2} + \sigma_y < y \le 1. \end{cases} \tag{5.4}$$

The rigid (unyielded) plug region lies within $y \in [\frac{1}{2} - \sigma_y, \frac{1}{2} + \sigma_y]$, where the fluid moves as a solid block with uniform velocity. The total width between the plates is unity. In the numerical simulations, a creeping flow assumption is made by setting $\rho = 0$, and the yield stress is fixed at $\sigma_y = 0.25$.

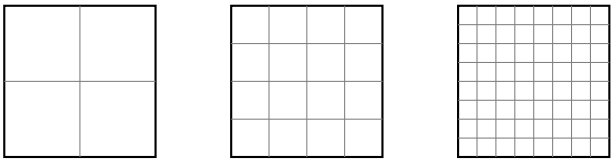

FIGURE 5.1: Mesh refinement hierarchy showing uniform subdivision of a square domain into 4 (left), 16 (center), and 64 (right) congruent rectangular elements. Demonstrates geometric progression of grid resolution for numerical analysis applications.

Figure 5.7 presents the velocity magnitude and pressure visualization for the Bingham flow in a channel with a yield stress of $\sigma_y = 0.25$. The simulation captures the characteristic features of viscoplastic flow (Bingham), including the presence of a central plug region where the material does not yield flow. In the visualization of velocity magnitude, a flat velocity profile is observed in the central region of the domain, indicative of the rigid plug zone, where the shear stress remains below the imposed yield stress σ_y. This region moves as a solid body with constant velocity and separates the high shear zones near the channel walls. Near wall regions exhibit a sharp gradient in velocity due to shear localization, where the stress exceeds σ_y and flow occurs via viscous deformation. The area of the plug region increases with

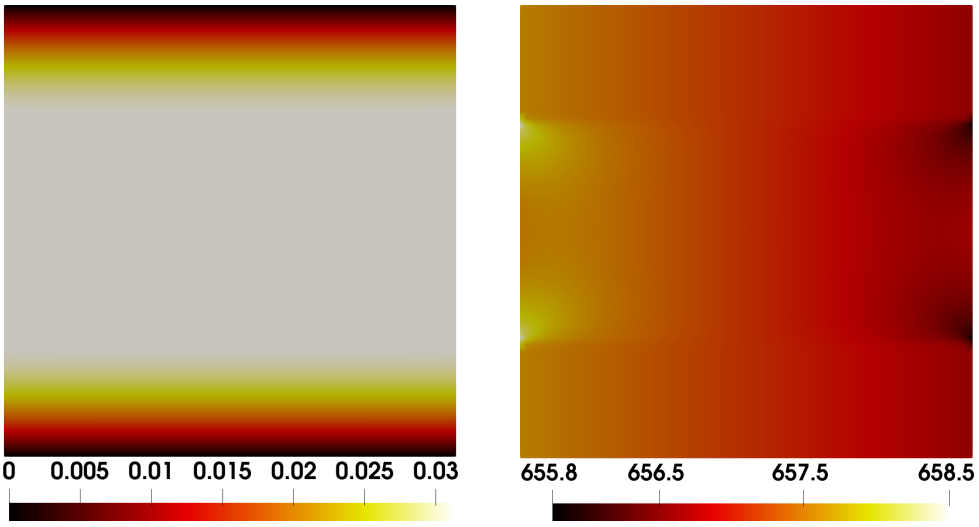

(a) Velocity magnitude (b) Pressure

FIGURE 5.2: Visualization of velocity magnitude and pressure distribution at $\sigma_y = 0.25$.

higher σ_y, reflecting reduced flow in the centre. The pressure field shown in 5.7 indicates a numerical error in the area around the rigid region. This is expected since in the model the stress tensor is undetermined in the rigid region.

The results presented in the Table 5.2 demonstrate the critical interplay between the Papanastasiou regularization parameter m, mesh alignment, and the resulting $\mathcal{L}^2$ norm velocity error in yield stress fluid simulations. For the mesh aligned cases ($\sigma_y = 0.250$), where the yield surface coincides with the boundary of the elements, errors exhibit consistent and predictable behavior across refinement levels. In the aligned configuration, the $\mathcal{L}^2$ error decreases monotonically with mesh refinement, reaching remarkably low magnitudes (e.g., below 10^{-7} for $m = 10^5$ at $\sigma_y = 0.25$), emphasizing the numerical advantage of maintaining alignment between the yield surface and the computational mesh. This alignment eliminates spurious interpolation errors across element edges, allowing the regularization scheme to capture the sharp yield surface transition more accurately. In contrast, the non-aligned cases ($\sigma_y = 0.300$ and 0.450) display erratic error patterns, with occasional increases in error at certain refinement levels (e.g., $\sigma_y = 0.300$ at $m = 10^4$, where the error rises from 5.88659e−4 at Lev 2 to 1.92194e−4 at Lev 3 before decreasing again), highlighting the destabilizing effects of yield surfaces cutting arbitrarily through elements.

TABLE 5.1: The relationship between the $\mathcal{L}^2$ norm velocity error and the regularization parameter m observed at different refinement levels.

	$L = 2$	$L = 3$	$L = 4$	$L = 5$	$L = 6$
$\sigma_y = 0.250$ (aligned case)					
$m = 10^1$	2.83182e−3	2.80536e−3	2.80385e−3	2.80802e−3	2.80380e−3
$m = 10^2$	4.77711e−4	5.54487e−4	5.35859e−4	5.35504e−4	5.35404e−4
$m = 10^3$	7.95147e−5	8.09976e−5	9.17084e−5	8.69674e−5	8.48112e−5
$m = 10^4$	8.67548e−6	8.83069e−6	8.97524e−6	9.33456e−6	9.88019e−6
$m = 10^5$	8.75649e−7	8.98809e−7	9.23477e−7	9.52896e−7	9.71171e−7
$\sigma_y = 0.300$ (non-aligned case)					
$m = 10^1$	2.58440e−3	2.54254e−3	2.53871e−3	1.53858e−3	2.53880e−3
$m = 10^2$	9.90130e−4	6.12491e−4	6.00094e−4	6.96166e−4	5.99610e−4
$m = 10^3$	6.01593e−4	2.22128e−5	8.87366e−5	9.35306e−5	8.97568e−5
$m = 10^4$	5.88659e−4	1.92194e−4	1.06356e−5	1.14795e−6	1.11260e−5
$m = 10^5$	5.89652e−4	1.88670e−4	9.07065e−6	1.15322e−6	2.00326e−6
$\sigma_y = 0.450$ (non-aligned case)					
$m = 10^1$	3.38752e−4	3.55901e−4	3.55360e−4	3.54892e−4	3.54873e−4
$m = 10^2$	3.23678e−4	3.33010e−4	3.29249e−4	3.28436e−4	3.28428e−4
$m = 10^3$	2.49320e−4	1.77443e−4	1.01513e−4	8.50683e−5	8.55395e−5
$m = 10^4$	2.33228e−4	1.37075e−4	2.74480e−5	1.49108e−5	1.16852e−5
$m = 10^5$	2.31380e−4	1.36095e−4	2.35430e−5	6.91479e−6	1.37997e−6

The non-aligned simulations are particularly sensitive to the choice of m, with intermediate values ($10^3 \leq m \leq 10^4$) often providing the best compromise between accuracy and stability, whereas extreme regularization ($m = 10^5$) can make errors worse due to the mismatch between the steep regularized stress gradient and the mesh resolution. The mesh-aligned cases, however, benefit significantly from increased regularization, as the aligned geometry avoids the numerical diffusion that plagues non-aligned interfaces. This distinction is crucial for practical applications: while aligned meshes are ideal for benchmarking and fundamental studies, real-world

simulations often involve complex, non-aligned yield surfaces, necessitating advanced techniques such as adaptive mesh refinement or interface-tracking methods to mitigate errors. The data further reveal that refinement alone cannot fully compensate for non-alignment, as seen in the persistent error fluctuations for $\sigma_y = 0.450$ across all m values, whereas the aligned cases achieve near exponential error reduction with refinement. These findings emphasize that mesh alignment should be prioritized wherever possible in yield-stress fluid simulations, as it not only enhances accuracy but also ensures more reliable convergence behavior.

TABLE 5.2: The table shows the number of iterations required for the solution to converge at different refinement levels.

	$\sigma_y = 0.250$				
	$L = 2$	$L = 3$	$L = 4$	$L = 5$	$L = 6$
$m = 10^1$	6	3	2	2	2
$m = 10^2$	6	5	3	4	3
$m = 10^3$	6	4	6	6	6
$m = 10^4$	9	8	9	7	11
$m = 10^5$	11	14	19	10	21
	$\sigma_y = 0.300$				
$m = 10^1$	3	3	2	2	2
$m = 10^2$	4	10	5	3	3
$m = 10^3$	16	16	6	7	6
$m = 10^4$	20	31	16	9	10
$m = 10^5$	24	27	25	12	28
	$\sigma_y = 0.450$				
$m = 10^1$	4	3	2	2	2
$m = 10^2$	6	10	3	4	3
$m = 10^3$	7	11	27	17	6
$m = 10^3$	5	31	26	19	10
$m = 10^3$	5	27	25	30	28

Table 5.2 presents the number of Newton iterations required to reach convergence for varying values of the regularization parameter m, refinement levels L, and yield stress values $\sigma_y = 0.25, 0.30, 0.45$. As expected, the non-linear convergence behavior is sensitive to both the regularization parameter and by higher yield stress values. For moderate yield stress $\sigma_y = 0.25$, the solver remains stable across all refinement levels. The number of iterations remains relatively low and nearly constant for small m, indicating that the system remains well-conditioned. However, as m increases to 10^5, the iterations increase notably, particularly for finer meshes, reflecting the stiffer nature of the regularized Bingham model as it approaches the ideal plastic limit. At $\sigma_y = 0.30$, a similar trend is observed, but with a sharper rise in Newton iterations, especially at higher values of m. The convergence is more sensitive to mesh refinement, showing a non-monotonic pattern. This indicates that the combination of higher yield stress and strong regularization increases the non-linearity of the problem, particularly near the yield surface. The most challenging case occurs for $\sigma_y = 0.45$, where the yield zone dominates the flow domain. For small m, Newton iteration counts remain modest, but as m increases beyond 10^3, the number of iterations grows substantially. In particular, for $m = 10^4$ and 10^5, the solver requires up to 30 iterations or more for convergence, especially on intermediate to fine grids. This behavior suggests that the solution becomes increasingly stiff and localized due to the expanding plug region, demanding finer resolution and stronger damping in the Newton steps. Overall, the data demonstrate that while the Newton-Raphson method is capable of handling regularized viscoplastic problems, its performance deteriorates as the regularization parameter $m \to \infty$ and σ_y increases. These trends highlight the importance of selecting an appropriate balance between regularization strength and mesh resolution to maintain solver robustness.

5.2.2 Pressure Gradient

A linear pressure is a solution to equations Equation (2.33), with the corresponding Bingham constitutive relation in equation Equation (2.27). However, the pressure field in Figure 5.7 shows a discontinuity in the region around the rigid zone. This lack of smoothness arises because, within the Bingham constitutive model, alternative pressure solutions may exist in the unyielded region, which in this case lies in the central area. The remedy is straightforward: a pressure difference between inflow

and outflow is imposed along the inflow or outflow boundaries, such that $u_y = 0$ and $\boldsymbol{\sigma} \cdot \vec{n} = 0$ in the outward normal direction of the numerical domain. This approach smooths the pressure distribution, as shown in Figure 5.3.

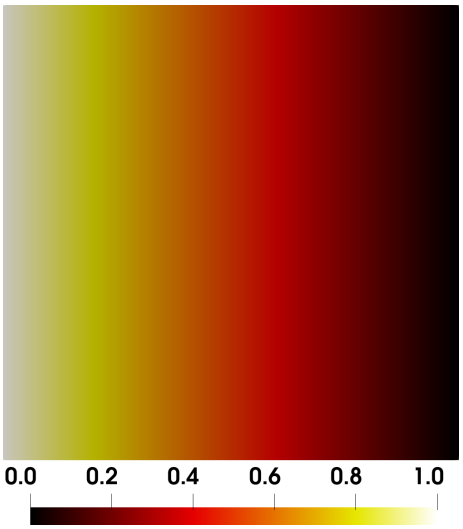

FIGURE 5.3: Visualization of a smooth pressure field.

5.3 Validating Viscoelastic Part

5.3.1 Planar Flow Past a Cylinder

Upon successfully validating the viscoplastic component, our subsequent focus shifts to validating the viscoelastic component by setting the yield stress, σ_y, to zero in Equation (2.33). To validate the viscoelastic component, we selected the flow around a cylinder benchmark to investigate drag across different Weissenberg numbers. Despite having no singularities in the geometry of the flow around a cylinder, achieving convergence at high elasticity is always a challenging task.

5.3.2 Problem Description

The computational domain considered for the present benchmark is a two-dimensional, rectangular channel containing a centrally placed semi-circular cylinder. Owing to

the symmetry of the flow configuration, only the upper half of the domain is simulated, thereby reducing computational cost while preserving accuracy. The domain extends along the streamwise direction $x \in [-20, 20]$, and the vertical extent of the half-domain spans $y \in [0, 2]$. The semi-circular cylinder is centered at the origin and has a radius $r = 1$, yielding a channel height of $H = 2r = 2$. A schematic illustration of the geometry and mesh used in this study is provided in Figure 5.4, which depicts the coarse mesh over the half-domain.

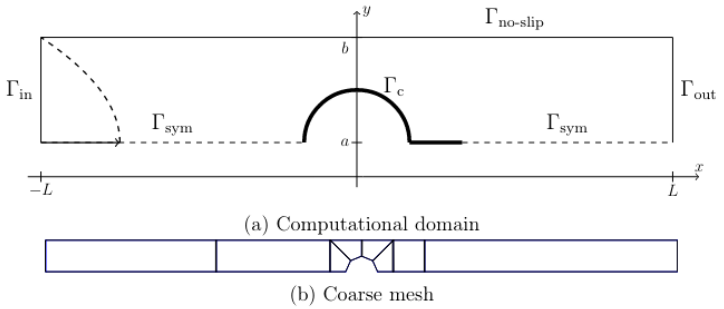

FIGURE 5.4: Coarse mesh for the flow around a cylinder (half-domain configuration).

Inlet and outlet boundary conditions are prescribed using fully developed velocity profiles to ensure physical consistency with analytical expectations in creeping flow conditions. The mean velocity is set to $U_{\text{mean}} = 1.0$. For the Oldroyd-B model, the inflow profile adopts a parabolic form given by:

$$u_x = \frac{3}{2} U_{\text{mean}} \left(1 - \left(\frac{y}{H}\right)^2\right), \qquad u_y = 0, \tag{5.5}$$

where H is the channel height. No-slip boundary conditions are imposed on the upper and lower channel walls. The outlet employs the same parabolic velocity profile as the inlet to minimize artificial reflections. The non-dimensional parameters governing the system are the Weissenberg number, defined as $Wi = \lambda U/r$, and the viscosity ratio $\beta = \eta/\eta_0$, where $\eta_0 = \eta + \eta_m$ is the total viscosity of the viscoelastic fluid. In this study, the mean velocity $U = 1$ is fixed, and the viscosity ratio is chosen as $\beta = 0.59$, which is consistent with standard benchmarks available in the literature [78, 79, 80]. To maintain a creeping flow regime, the fluid density is set to $\rho = 0$, thereby eliminating inertial effects.

The primary quantity of interest is the drag coefficient on the cylinder surface, which serves as a key validation metric. It is computed as:

$$C_{\text{drag}} = 2 \int_s (\boldsymbol{\sigma} \cdot \vec{n})\, ds, \tag{5.6}$$

where $\boldsymbol{\sigma}$ denotes the total stress tensor and $\vec{n}$ is the outward unit normal to the cylinder surface. Simulations are conducted for a range of relaxation times corresponding to $Wi \in [0.1, 0.6]$, and results are compared against established reference values [79]. Excellent agreement is observed across all tested cases, thereby validating the fidelity of the numerical formulation and its implementation. Further improvements in accuracy are evident with increasing mesh refinement. The number of non-linear iterations (denoted as NI in the table below) reflects the performance of the Newton solver and remains stable across all test cases, indicating robust convergence behavior.

TABLE 5.3: Validation of the solver against drag values of the flow over a cylinder in a rectangular channel for different Weissenberg numbers and $\beta = 0.59$.

	$Wi = 0.1$			$Wi = 0.2$		
Level	Drag	NI	Ref. [79]	Drag	NI	Ref. [79]
3	130.063	3	-	126.361	3	-
4	130.283	3	-	126.551	3	-
5	130.342	3	130.366	126.606	3	126.628
	$Wi = 0.3$			$Wi = 0.4$		
Level	Drag	NI	Ref. [79]	Drag	NI	Ref. [79]
3	122.969	3	-	120.416	3	-
4	123.105	3	-	120.527	3	-
5	123.171	3	123.194	120.572	3	120.593
	$Wi = 0.5$			$Wi = 0.6$		
Level	Drag	NI	Ref. [79]	Drag	NI	Ref. [79]
3	118.730	4	-	117.730	4	-
4	118.766	4	-	117.717	4	-
5	118.809	4	118.828	117.758	4	117.779

Across all tested Weissenberg numbers from $Wi = 0.1$ to $Wi = 0.6$, the drag coefficients converge monotonically with increasing mesh resolution levels (denoted as Levels 3 to 5). This monotonic convergence is expected due to increased resolution of stress gradients and wake structures around the cylinder as the mesh is refined. Importantly, the drag values obtained on the finest level (Level 5) show excellent agreement with the reference values reported by Damanik et al. [79], with discrepancies on the order of $\sim 0.02\%$ to 0.03%, thereby validating both the numerical method and its implementation. For example, at $Wi = 0.1$, the computed drag at Level 5 is 130.342, closely matching the reference value of 130.366. Similar behavior is observed at higher Weissenberg numbers, such as $Wi = 0.6$, where the computed drag is 117.758 compared to the reference 117.779. This level of precision demonstrates that the solver captures the viscoelastic effects with high fidelity and confirms the robustness of the discretization and solution strategy, even in elasticity-dominated regimes. Another key indicator of solver performance is the number of non-linear iterations (NI), specifically Newton iterations, required for convergence. Across all Weissenberg numbers and mesh levels, the number of iterations remains consistent, with three iterations at $Wi \leq 0.4$ and four iterations for $Wi \geq 0.5$. This trend reflects the increasing non-linearity introduced by the viscoelastic stress terms at higher Wi, necessitating slightly more iterations for convergence. However, the increase is modest and indicates strong convergence behavior, which is particularly significant given the well-known numerical difficulties (e.g., high Weissenberg number problem) associated with viscoelastic flows. The consistent Newton iteration count across refinement levels for a given Wi also suggests that the initial guess quality and preconditioner effectiveness are not significantly affected by mesh resolution in this context. This is an important observation for large-scale simulations where computational efficiency is a concern. Overall, the results in the above Table confirm the accuracy of the numerical method in reliably predicting the drag force within an acceptable tolerance when compared with benchmark results across all examined Weissenberg numbers. Newton iterations remain low and stable, indicating a well-conditioned non-linear system. Furthermore, systematic refinement leads to convergent results, suggesting proper implementation of the finite element discretization and stabilization schemes. These findings validate the developed solver in the symmetric cylinder benchmark and establish confidence in its applicability for more complex geometries and flow configurations involving viscoelastic fluids.

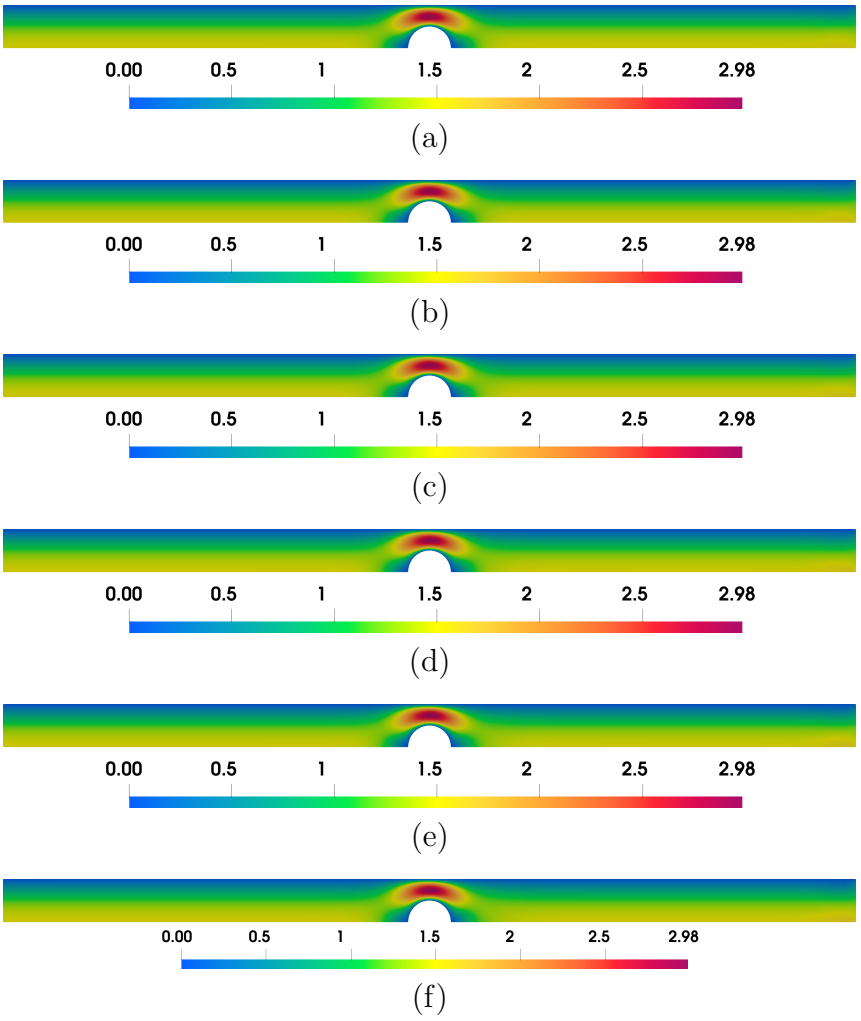

FIGURE 5.5: Velocity magnitude fields for different Weissenberg numbers: (a) $We = 0.1$, (b) $We = 0.2$, (c) $We = 0.3$, (d) $We = 0.4$, (e) $We = 0.5$, (f) $We = 0.6$.

Figure 5.5 presents the normalized velocity magnitude contours for flow past a semi-circular cylinder located at the center of a 2D channel, with increasing Weissenberg numbers, $Wi \in [0.1, 0.6]$. From a qualitative perspective, the velocity fields exhibit a high degree of symmetry about the channel centerline for all values of Wi, consistent with the imposed geometric and boundary symmetries. Across all subfigures (a)-(f), the core features of the flow, namely the stagnation region at the front of the cylinder, the acceleration along the sides, and the velocity recovery in the wake, remain qualitatively preserved. This indicates that the viscoelastic stress effects introduced by increasing Wi do not drastically alter the overall topology of the velocity field within this Weissenberg range. A more detailed observation suggests only modest

variations in the velocity distribution with increasing We. As Wi increases from 0.1 to 0.6, there is a subtle but observable elongation of the velocity gradient near the cylinder surface, especially in the rear wake zone. This behavior can be attributed to the increased elastic stress buildup in the polymeric fluid component, which resists deformation and modifies the local strain rates. However, the magnitude of these effects remains limited in this parameter range, which explains the weak visual sensitivity in the velocity fields. Overall, while the velocity magnitude fields do not display striking visual differences across the range of Weissenberg numbers considered, the underlying viscoelastic effects are still present and measurable through integral quantities like drag. These results serve to validate the implementation of the Oldroyd-B constitutive model in the current computational framework and provide a baseline for further investigations at higher elasticity or under transient conditions.

5.4 Validating Elastoviscoplastic Part

In the final phase of our validation process, we will evaluate the elastoviscoplastic component by examining its behavior. For this, we will perform our simulations in a porous media as a test case [14]. This particular test case serves as a comprehensive benchmark to evaluate the performance and accuracy of our mathematical formulations. Studying the dynamics of the fluid that flows through porous media is of great importance in many fields of engineering, and natural science, including other areas such as soil sciences, hydrology, solid mechanics, and polymer property measurement[81, 82]. The purpose of this study is to investigate the complex fluid possessing elastic, viscous, and plastic properties through the porous media. Flow of complex fluid, in our case elastoviscoplastic, materials through porous media has been the key interest for many researchers. By considering the complex interactions and flow dynamics within a porous medium, we aim to ensure that our model can effectively capture the elastoviscoplastic behavior in a realistic and challenging setting. This rigorous validation approach will further enhance the credibility and robustness of our computational model, providing confidence in its ability to

accurately simulate and analyze elastoviscoplastic fluids in various practical applications. Before diving into the problem description and numerical investigation of fluid through porous media, let's define what porous media is.

5.4.1 Porous Media

A porous medium is defined as a solid structure, often referred to as a porous matrix, that contains interconnected voids known as pores. It is a region consisting of at least two material components, supposed to be homogenous, presenting identifiable interfaces between them, with at least one of the constituents remaining fixed or slightly deformable or simply the solid structure with interconnected voids [81]. The key properties of a porous medium consist of porosity and permeability.

5.4.2 Porosity and Permeability

Porosity is defined as the ratio of the volumes of the void to the total volume of the material. Mathematically, it is written as:

$$\phi = \frac{V_p}{V_t}, \tag{5.7}$$

where ϕ is the porosity. Here $V_t = V_p + V_s$, V_p representing the void volume, V_s as the solid material volume and V_t the total volume. The expression in equation Equation (5.7) can be rewritten as:

$$\phi = \frac{V_t - V_s}{V_t}, \tag{5.8}$$

note that zero porosity means there is no space for flow, while non-zero porosity indicates that a material can flow. The greater the porosity, the more space there is for the material to flow. Porosity usually varies from 0 to 1. After defining the porosity of the porous media the next important term is permeability. Permeability, represented by κ, indicates the ability of the fluid to flow through the porous medium. It depends on the distribution or connectivity of the pores, no pores space leads to non-permeability and in that case, $\kappa = 0$ means the medium is impermeable, whereas if κ is infinite it shows the medium offers no resistance to flow [83, 84, 85, 86]. The

flow through the porous media is numerically treated by Darcy's law [87] which is a linear relationship between the velocity and the gradient of the pressure. This law is only valid for Newtonian fluids with low Reynolds numbers.

5.4.3 Problem Description and Research Objectives

The present work investigates the influence of geometrical symmetry on EVP flow characteristics by considering two carefully constructed porous domains: one symmetric and one unsymmetric, both containing cylindrical inclusions arranged within a square domain of length 2.25 units. In both configurations, the inclusions have a radius of unity and are arranged such that the total porosity remains fixed at 0.38. The symmetric configuration features a uniform distribution of inclusions about the domain center, preserving reflectional symmetry with respect to both the horizontal and vertical axes. In contrast, the unsymmetric configuration is generated by vertically shifting selected inclusions in a way that breaks this mirror symmetry, resulting in anisotropic pore throat widths and nonuniform spatial confinement.

This comparative setup enables a systematic study of how flow topology, yielding, and stress distribution depend on microstructural regularity. In the symmetric configuration, one expects the flow field to be nearly extensional along the centerline, with streamlines symmetrically distributed around the inclusions. Such configurations are useful as benchmarks, as they tend to yield uniform stress fields and facilitate a clearer understanding of yield surface evolution. On the other hand, the unsymmetric configuration introduces variations in local channel widths and bending of streamlines, thereby producing nonuniform shear rates and localized zones of high stress. This arrangement mimics features of natural porous structures, where anisotropy and disorder often dominate.

The simulations are performed under a fixed Reynolds number of $Re = 0.8$ and a Weissenberg number of $Wi = 0.1$. These values are chosen to ensure that the flow remains in a laminar regime while allowing for non-negligible inertial effects and weak elastic memory. At $Wi = 0.1$, the relaxation time of the fluid is short relative to the convective time scale, so the contribution of viscoelasticity to the stress field is moderate. Meanwhile, the Reynolds number is low enough to preclude

turbulence but large enough to permit mild inertial asymmetries, particularly in regions of geometrical constriction or flow separation. This regime is thus ideal for probing the interplay between geometry induced strain localization and the yielding dynamics characteristic of EVP materials.

To further examine the role of plasticity in shaping the flow, the Bingham number $Bi = \sigma_y r/(\eta U)$ is systematically varied across several simulations. The selected values span from weakly yield-dominated flows ($Bi = 0.1$) to strongly plug-like regimes ($Bi = 10$), enabling a multi-regime comparison across both geometrical setups. Throughout these simulations, the elastic weighting parameter $\beta = 0.5$ is held constant to isolate the effects of geometry and yielding. The constitutive behavior of the EVP fluid is modeled using a regularized Saramito type formulation, which incorporates both the yield stress criterion and viscoelastic stress evolution governed by an upper-convected Maxwell model.

The primary objective of this investigation is to quantify and compare how symmetric and unsymmetric microstructures influence key features of EVP flow. Specifically, the study aims to examine the formation and shape of yield surfaces, the spatial distribution of velocity and stress fields, and the emergence of flow heterogeneity and anisotropy. In symmetric domains, yielded regions are expected to grow uniformly with increasing applied stress, and the flow field should reflect the geometric symmetry. Conversely, in the unsymmetric case, sharp gradients in stress and velocity are anticipated due to the variable pore geometry, leading to earlier and more localized yielding. These differences are expected to have significant implications for macroscopic properties such as effective permeability, flow resistance, and pressure drop. Ultimately, this work contributes to a deeper understanding of how geometry rheology coupling governs flow in porous media with EVP fluids. The insights obtained here lay the groundwork for the development of more accurate upscaling models and inform the design of engineered porous materials for applications involving complex rheological fluids. The domain can be seen in Figure 5.6.

In the symmetric case, the domain is subjected to a velocity-driven flow entering from the left pore, while a no-slip boundary condition is enforced on the surface of the cylinder. Conversely, in the unsymmetric geometry, a pressure driven flow is applied at the inlet, and the surface of the solid cylinders adheres to the no-slip

condition. The key parameters considered in this setup include:

$$Re = \frac{\rho U r}{\eta_0}, \quad Wi = \frac{\lambda U}{r} \qquad \text{and} \quad Bi = \frac{\sigma_y r}{\eta_0 U} \tag{5.9}$$

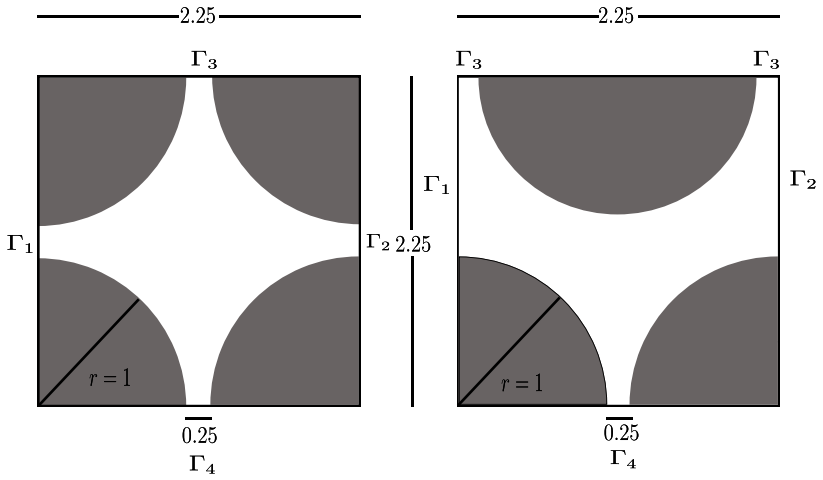

FIGURE 5.6: Computational domain for symmetric and unsymmetric porous media.

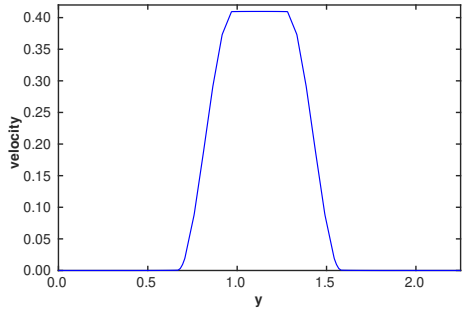

(a) Velocity cutline at the centre of the domain (symmetric).

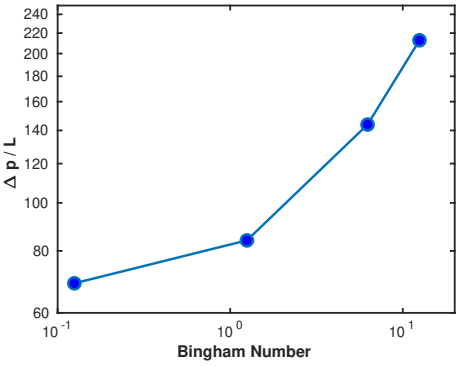

(b) Pressure drops against different Bingham numbers (symmetric).

FIGURE 5.7: Cutline and pressure drops in a symmetric porous configuration.

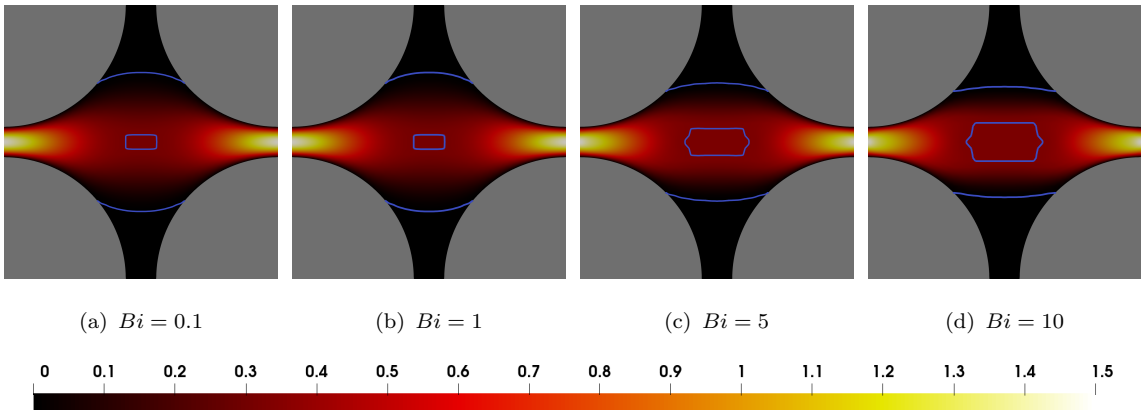

(a) $Bi = 0.1$ (b) $Bi = 1$ (c) $Bi = 5$ (d) $Bi = 10$

FIGURE 5.8: Velocity contours in a viscoplastic fluid through a symmetric porous medium at $Re = 0.8$ for varying Bingham numbers. The blue curves denote dynamic yield surfaces, the top and bottom black zones represent static unyielded regions.

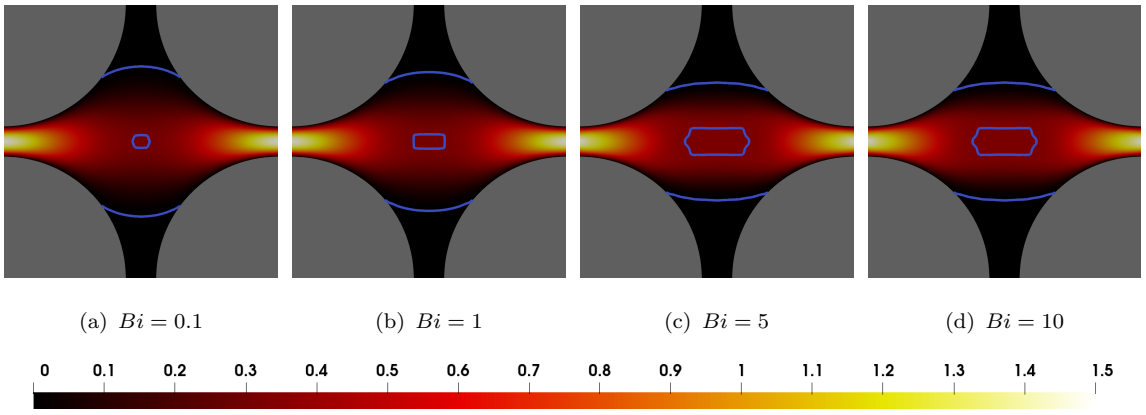

(a) $Bi = 0.1$ (b) $Bi = 1$ (c) $Bi = 5$ (d) $Bi = 10$

FIGURE 5.9: Velocity contours for an elastoviscoplastic (EVP) fluid in the same porous geometry at $Re = 0.8$, $Wi = 0.01$, under varying Bingham numbers. Blue lines mark the dynamic yield surfaces, while static unyielded regions are shown in black.

Figures 5.8 and 5.9 present velocity contours for viscoplastic (VP) and elastoviscoplastic (EVP) fluids flowing through a model porous domain consisting of a symmetric array of cylinders at a fixed Reynolds number $Re = 0.8$. The Bingham number (Bi) is varied from 0.1 to 10 to investigate the influence of yield stress, while the Weissenberg number (Wi) is kept at 0.001 for the VP case (Figure 5.8) and 0.01 for the EVP case (Figure 5.9). These visualizations provide insight into how plasticity and elasticity affect flow structure, yield surface formation, and flow confinement within a periodic porous geometry.

In the VP case 5.8, at low Bingham number ($Bi = 0.1$), the velocity field closely resembles that of a Newtonian fluid with flow concentrated between the cylinders and smooth gradients extending into the wake regions. As the Bingham number increases to 1, 5, and 10, distinct unyielded regions emerge, represented by black contours upstream and downstream of the cylinders. These stagnant zones indicate areas where the stress is insufficient to exceed the yield threshold, resulting in solid-like behavior. Between these static unyielded zones, narrow regions of yielded flow persist, and as Bi increases, the flow becomes increasingly localized and confined to thin channels. The blue lines represent moving yield surfaces, boundaries separating yielded and unyielded regions, and become more complex and elongated with increasing Bi, indicating the increased dominance of yield stress in shaping the flow domain.

In the EVP case 5.8, with a slightly higher elasticity ($Wi = 0.01$), the impact of elasticity on the velocity field becomes apparent. At low $Bi = 0.1$, the flow retains a similar topology to the VP case; however, small deviations are observed in the yield surface geometry and velocity gradient localization. As Bi increases, the flow field exhibits sharper transitions near the yield surfaces and narrower yielded zones. The moving yield surfaces (blue lines) are more tightly wrapped around the cylinders, and the velocity field becomes increasingly confined. Notably, the contours exhibit more angular distortions in the yielded regions, indicating an interaction between elastic stress storage and yield dynamics.

Compared to the VP results, the EVP velocity fields show a more prominent elongation and sharpening of the shear layers adjacent to the cylinder boundaries and in the downstream wake. The presence of elastic stresses, even at moderate We, contributes to a redistribution of mechanical stress in the domain, delaying yielding and enhancing flow localization. This effect is more noticeable at higher Bingham numbers, particularly $Bi = 5$ and $Bi = 10$, where the EVP flow becomes visibly more confined than its VP counterpart. Elastic contributions also affect the shape and size of the moving yield surfaces, which become more curved and asymmetric, especially near the cylinder wake.

Both figures show the emergence of static unyielded regions at the top and bottom of the domain, aligned with the symmetry of the periodic configuration. These regions remain mostly unchanged across cases and act as structural barriers to flow.

However, their relative size and shape are slightly altered in the EVP simulations, where elasticity enhances the rigidity of these stagnant zones by resisting deformation through stored stress.

In summary, increasing the Bingham number suppresses flow across both VP and EVP fluids by enlarging unyielded regions and reducing the effective channel width. The introduction of even mild elasticity in EVP fluids further constrains the flow, sharpens stress gradients, and modifies the geometry of yielded regions. The yield surfaces become more reactive to stress orientation and local deformation history. These results highlight the complex interplay between viscous dissipation, plastic yield-limited behavior, and elastic memory in EVP flows, especially in geometrically constrained domains such as porous media.

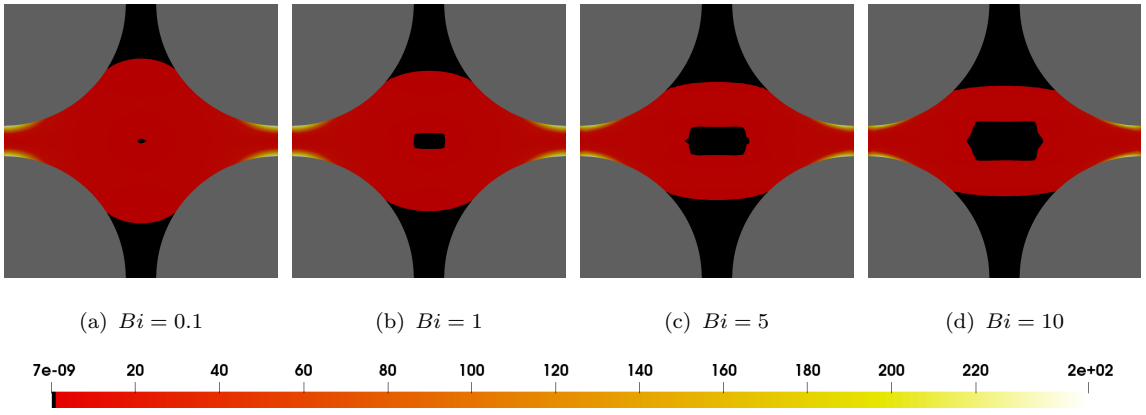

FIGURE 5.10: Visualization of the deformation in the EVP fluid within the model porous medium for the symmetric arrangement of cylinders at $Re = 0.8$, $Wi = 0.01$, with varying Bingham numbers.

The blue line present in the middle in Figure 5.8 represents the moving yielding surface, as expected that the higher Bingham number results in the big unyielded region. The simulation we performed for the symmetric part of the porous media shows a strong agreement with the data available in the literature [14].

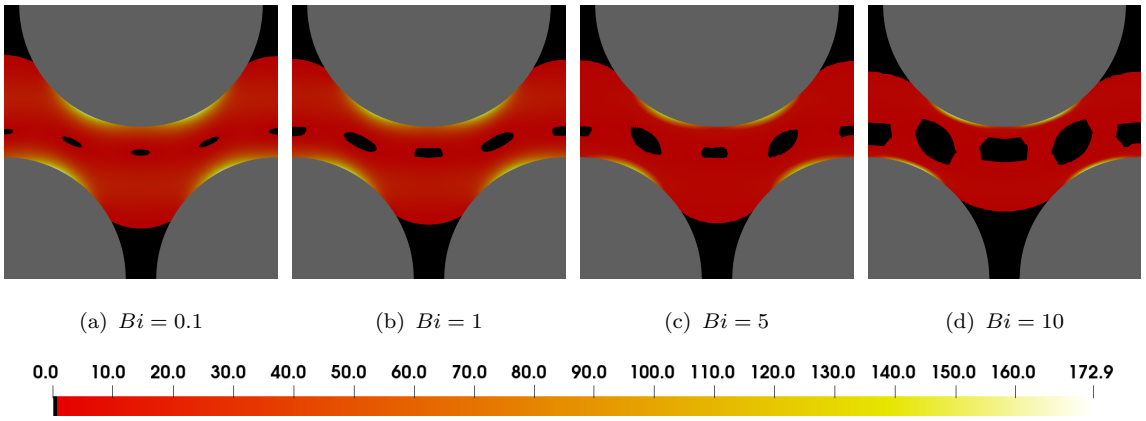

(a) $Bi = 0.1$ (b) $Bi = 1$ (c) $Bi = 5$ (d) $Bi = 10$

FIGURE 5.11: Visualization of the deformation in the EVP fluid within the model porous medium for the unsymmetric arrangement of cylinders at $Re = 0.8$, $Wi = 0.01$, with varying Bingham numbers.

The blue lines in the middle of the geometry in terms of small patterns for the unsymmetric case can be witnessed in Figure 5.11 represent the moving yielding surface. Like in the symmetric case the same pattern is expected for the unsymmetric part i.e., the higher the Bingham number is the bigger the unyielded region is. The top and bottom region is the static unyieldied region. The simulation for the unsymmetric part of the porous media also shows a strong agreement with reference results [14].

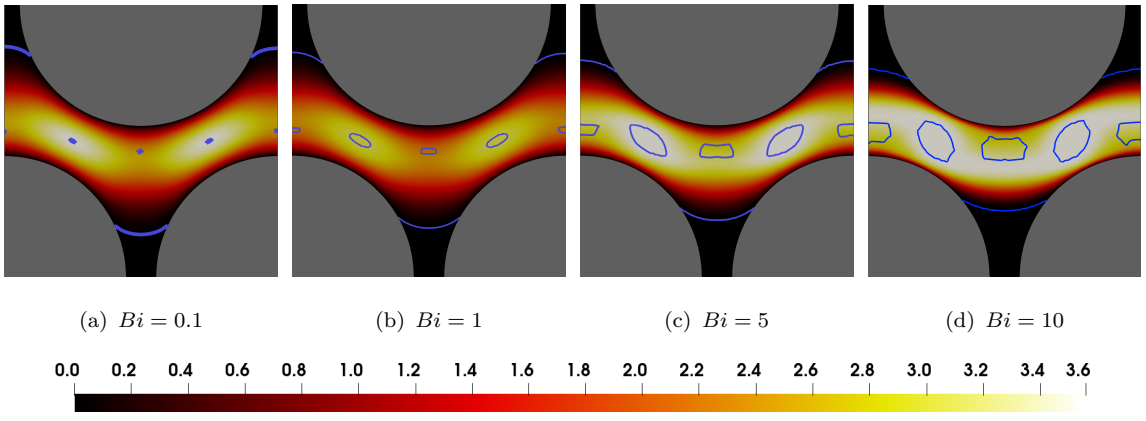

(a) $Bi = 0.1$ (b) $Bi = 1$ (c) $Bi = 5$ (d) $Bi = 10$

FIGURE 5.12: Visualization of the velocity contours in the EVP fluid within the model porous medium for the unsymmetric arrangement of cylinders at $Re = 0.8$, $Wi = 0.01$, with varying Bingham numbers. The blue lines in the middle represent the moving yield surfaces. The top and bottom black region is the static unyieldied region.

5.4.3.1 Flow Topology

We will now shift our focus towards the flow topology. The motivation is to figure out how the shear, rotational, and shear flow has evolved and distributed inside the symmetric and unsymmetric domains. We will achieve this with the help of a parameter Q. This parameter is known as the flow topology parameter and it is defined as:

$$Q = \frac{\mathbf{II}^2(\boldsymbol{D}) - \mathbf{II}^2(\boldsymbol{W})}{\mathbf{II^2}(\boldsymbol{D}) + \mathbf{II}^2(\boldsymbol{W})}, \tag{5.10}$$

where $\mathbf{II}^2(\boldsymbol{D}) = (\boldsymbol{D} : \boldsymbol{D})$ and $\mathbf{II}^2(\boldsymbol{W}) = (\boldsymbol{W} : \boldsymbol{W})$. Here, $Q = -1$ corresponds to pure rotational flow, while $Q = 0$ and $Q = 1$ represent pure shear and pure elongational flow, respectively. From Figure 5.13 one can observe the distribution of shear, rotational, and elongational flows in the symmetric geometry of the porous medium. The figure clearly shows that shear-dominated flow occurs near the cylinder walls, rotational flow is observed at dead ends due to the presence of vortices, and the elongational pattern changes with increasing Bingham number [88].

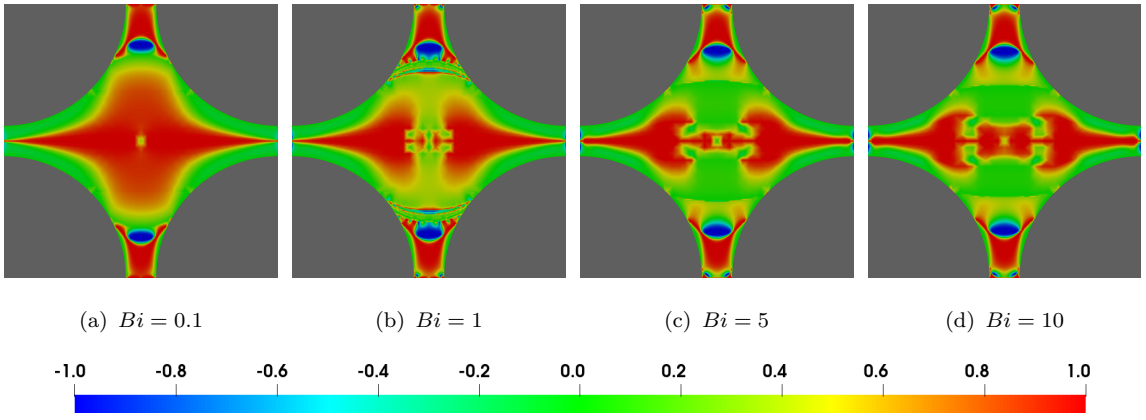

FIGURE 5.13: Visualization of the flow topology in the EVP fluid within the model porous medium for various Bingham numbers.

5.5 Flow Around Cylinder

Benchmark problems in computational fluid dynamics are indispensable for validating numerical methods due to their clearly defined geometry and boundary conditions, and their known fluid dynamic responses. One such extensively employed

benchmark is present in the literature. This benchmark provides a standard configuration with detailed geometric specifications and boundary conditions, suitable for systematically evaluating numerical methods across diverse fluid rheologies.

In this study, we adopt the classical flow around cylinder benchmark, specifically the two-dimensional laminar case with a fixed Reynolds number ($Re = 20$), to investigate elastoviscoplastic (EVP) fluids modeled via the combined Oldroyd-B viscoelastic model and the Papanastasiou regularized Bingham plastic model. This configuration is selected due to its well documented steady state solution characteristics, including clearly defined recirculation zones and symmetrical wake structures, making it ideal for investigating subtle effects induced by viscoelasticity and yield-stress behavior.

The geometry comprises a rectangular computational domain measuring 2.2 units in length and 0.41 units in height, containing a centrally positioned cylinder of diameter $D = 0.1$ units, with its center located at coordinates $(0.2, 0.2)$. The fluid density is set to unity ($\rho = 1$), and the total viscosity (η_0) is defined as 0.001, which together establish the fixed Reynolds number of 20 based on the mean inflow velocity and the cylinder diameter.

Boundary conditions are carefully defined: on the left inlet boundary (Γ_1), a parabolic velocity profile is prescribed, having a maximum inlet velocity of $U = 0.3$, described by

$$u_{\text{in}}(y) = \frac{4Uy(0.41 - y)}{0.41^2}, \tag{5.11}$$

ensuring laminar flow development. On the right outlet boundary (Γ_2), natural outflow conditions are applied. Both the upper and lower horizontal walls, as well as the cylinder surface itself, are subjected to no-slip conditions, thus accurately reflecting typical wall-bounded flow scenarios.

The central interest in this benchmark is quantifying the effect of elastoviscoplastic rheological properties on the drag (C_D) and lift (C_L) coefficients acting upon the cylinder. These coefficients are defined in a conventional manner by

$$C_D = \frac{2F_D}{\rho U^2 D}, \quad C_L = \frac{2F_L}{\rho U^2 D}, \tag{5.12}$$

where F_D and F_L represent the integrated drag and lift forces along the cylinder surface. Due to the unique behavior of EVP fluids, particularly the existence of yielded (flowing) and unyielded (solid-like) zones, significant deviations from standard Newtonian flows are anticipated in both magnitude and spatial distribution of stress, hence altering the drag and lift characteristics.

The simulations focus on systematically varying two critical dimensionless parameters, the Weissenberg number (Wi) and the Bingham number (Bi). The Weissenberg number, representing fluid elasticity, is defined by

$$Wi = \frac{\lambda U}{D}, \tag{5.13}$$

with λ denoting the characteristic relaxation time. Initially, a small elasticity case ($Wi = 0.01$) is investigated to identify subtle viscoelastic influences, followed by a moderate elasticity case ($Wi = 0.1$) to explore more pronounced elastic effects.

The Bingham number, quantifying the yield stress effect, is given by

$$Bi = \frac{\sigma_y D}{\eta U}, \tag{5.14}$$

and is explored across a range of values ($Bi = 0.01, 0.1, 0.5$, and 1.0). This comprehensive parameter range covers nearly Newtonian conditions through strongly yield-dominated scenarios, enabling detailed analysis of how yield stress impacts flow separation, vortex formation, wake dynamics, and resulting forces. Additionally, the Papanastasiou regularization parameter m, a dimensionless stress growth parameter, is introduced to smooth the discontinuous yield stress characteristic. It is defined mathematically as

$$m = \frac{MU}{D}, \tag{5.15}$$

where M is a dimensional parameter controlling the sharpness of the transition between yielded and unyielded regions. Although higher values of m enhance the accuracy of the yield-surface representation by closely approximating the idealized discontinuity, they significantly increase numerical stiffness, making the non-linear iterative solution procedure more challenging and often hindering convergence. Therefore, a moderate value of $m = 200$ is commonly adopted in practice, as it represents a

good balance between computational tractability and the accuracy of the yield-stress approximation, ensuring reliable numerical simulations.

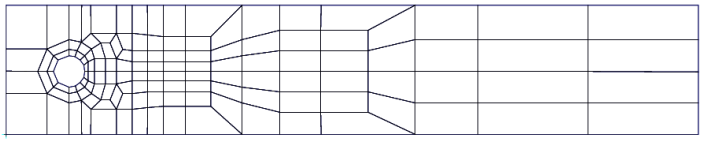

FIGURE 5.14: Coarse mesh for the flow around a cylinder.

TABLE 5.4: Number of Equations (NEQ) per Level for Velocity ($\boldsymbol{u}$), Stress ($\boldsymbol{\sigma}$), and Pressure (p) Discretizations

Lev.	NEQ $\boldsymbol{u}$	NEQ $\boldsymbol{\sigma}$	NEQ p	Total NEQ
L0	1144	1716	390	3250
L1	4368	6552	1560	12480
L2	17056	25584	6240	48880
L3	67392	101088	24960	193440
L4	267904	401856	99840	769600

Notes: NEQ denotes the number of discrete equations for velocity ($\boldsymbol{u}$), stress ($\boldsymbol{\sigma}$), and pressure (p) fields at each refinement level (L0–L5).

TABLE 5.5: Computed drag (C_D), lift (C_L), and number of linear/average non linear iterations (N/L) at fixed $Wi = 0.001$, for various Bingham numbers.

Level	$Bi = 0.01$			$Bi = 0.1$		
	C_D	C_L	N/L	C_D	C_L	N/L
1	5.5587	0.0092	1/2	5.6766	0.0112	1/2
2	5.5809	0.0105	3/1	5.7043	0.0122	6/1
3	5.6151	0.0107	3/1	5.7158	0.0126	7/1
4	5.6384	0.0107	3/1	5.7206	0.0126	4/1
	$Bi = 0.5$			$Bi = 1.0$		
1	6.2538	0.0275	1/2	7.0319	0.0370	1/2
2	6.2891	0.0316	3/1	7.0736	0.0399	6/1
3	6.2994	0.0319	3/1	7.0854	0.0404	7/1
4	6.3013	0.0338	3/1	7.0886	0.0404	4/1

The numerical results reported in Table 5.5 and Table 5.5 correspond to steady state simulations of an elastoviscoplastic (EVP) fluid, described by the Oldroyd-B model augmented with a Papanastasiou-regularized Bingham term, flowing past a

TABLE 5.6: Computed drag (C_D), lift (C_L), and number of linear/average non-linear iterations (N/L) at fixed $Wi = 0.01$, for various Bingham numbers.

Level	$Bi = 0.01$			$Bi = 0.1$		
	C_D	C_L	N/L	C_D	C_L	N/L
1	5.5762	0.0088	7/1	5.6933	0.0109	6/1
2	5.6008	0.0102	6/1	5.7187	0.0121	5/1
3	5.6094	0.0103	4/2	5.7298	0.0123	6/2
4	5.6115	0.0104	2/4	5.7324	0.0123	6/2
	$Bi = 0.5$			$Bi = 1.0$		
1	6.2722	0.0272	6/1	7.0477	0.0366	5/1
2	6.2924	0.0315	2/1	7.0913	0.0394	7/1
3	6.3155	0.0319	7/1	7.0868	0.0405	7/1
4	6.3241	0.0323	2/1	7.1066	0.0399	7/2

stationary circular cylinder. The flow regime is governed by two primary dimensionless numbers: the Bingham number (Bi), characterizing the relative strength of yield stress to viscous stress, and the Weissenberg number (Wi), representing the fluid's elasticity. For each Bi, the computed drag coefficient (C_D), lift coefficient (C_L), and solver performance indicators, namely, the number of Newton iterations and the average number of multigrid linear iterations per Newton step (N/L) are presented at four successive levels of refinement. A consistent increase in C_D is observed with increasing Bingham number for both Weissenberg numbers ($Wi = 0.001$ and 0.01), reflecting the resistance due to the presence of yield stress. For instance, at $Wi = 0.001$ and level 4, C_D increases from approximately 5.6384 for $Bi = 0.01$ to 7.0886 for $Bi = 1.0$, with a similar monotonic trend observed for $Wi = 0.01$. This increase in drag arises due to the formation and growth of unyielded zones around the cylinder, the behavior reported in previous computational studies of viscoplastic flows. Lift coefficients (C_L) also increase with Bi. At $Wi = 0.001$, C_L grows from approximately 0.0092 at $Bi = 0.01$ to 0.0370 at $Bi = 1.0$ on level 1, with a similar trend continuing across refinement levels. The magnitude and sensitivity of C_L to refinement and Weissenberg number reflect the strong coupling between stress and vorticity in elastoviscoplastic regimes. From the observation of solver performance, the non-linear (Newton) and linear (multigrid) iteration counts provide insight into algorithmic efficiency across the EVP parameter space. At $Wi = 0.001$, convergence is robust and consistent: the number of Newton iterations per level remains

low (typically 1-3), and the multigrid linear solver converges rapidly (often within a single iteration). This indicates a favorable conditioning of the Jacobian system and an effective damping of residuals, characteristic of EVP problems in low elasticity regimes. However, at $Wi = 0.01$, Newton iteration counts increase noticeably (e.g., reaching up to 7 at $Bi = 0.5$ and level 3), and the number of linear iterations per Newton step also rises. In particular, high N/L values such as $7/2$ suggest that the multigrid solver's smoothing and coarse-grid correction are challenged by the increased stiffness of the system under higher Wi. Across all Bingham numbers and both We values, the drag and lift coefficients tend to converge with mesh refinement. However, the solver behavior shows mixed trends. At $Wi = 0.001$, both non-linear and linear iteration counts tend to stabilize or improve slightly with refinement, indicating that the smoother velocity and stress fields facilitate convergence. Conversely, at $Wi = 0.01$, no such trend is consistently observed. In some cases, refinement results in increased iteration counts, implying that the solver efficiency is dominated by elasticity-induced stiffness rather than discretization error. Overall, the interplay between Bi, Wi, and grid level elaborates the complex behavior of EVP flows. Higher Bingham numbers significantly increase drag and lift, while higher Weissenberg numbers impair solver performance.

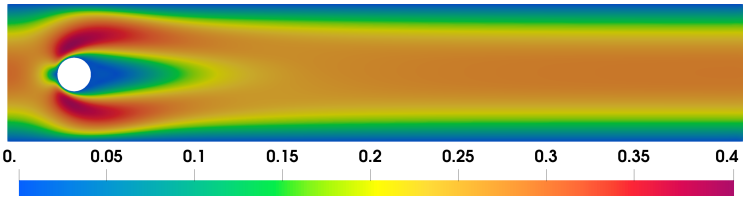

FIGURE 5.15: Velocity field around a cylinder for $Wi = 0.001$ and $Bi = 0.1$.

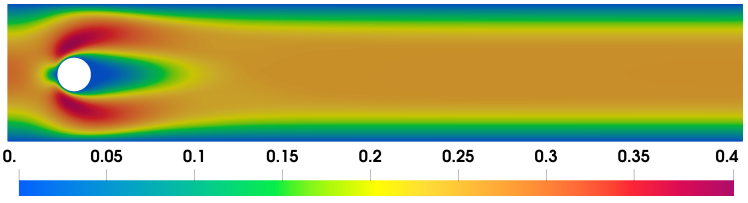

FIGURE 5.16: Velocity field around a cylinder for $Wi = 0.001$ and $Bi = 0.5$.

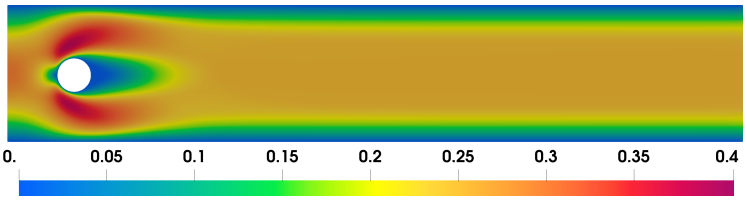

FIGURE 5.17: Velocity field around a cylinder for $Wi = 0.001$ and $Bi = 1$.

Chapter 6

Conclusion

Our current study has provided a comprehensive insight into the mathematical model for the elastoviscoplastic fluid, finite element approximation, and the behavior of fluids within different geometries, including porous media. Initially, a robust mathematical framework was introduced for the elastoviscoplastic fluids, depicting the true rheological behavior of complex fluids such as elastviscoplastic fluid by incorporating the Oldroyd B model and the Papanastasiou regularized model into the momentum equation. The present mathematical model is then approximated using the finite element technique (mixed formulation) that incorporates a $\mathbb{Q}_2$ element for velocity stress and a discontinuous $\mathbb{P}_1$ element for the approximation of pressure. To solve the resulting nonlinear system of equations arising from the finite element discretization, we applied Newton's method. This iterative approach is particularly a perfect tool for dealing with the nonlinearities inherent in elastoviscoplastic fluid behavior. The finite element framework and simulating fluid behavior through different geometries were quite challenging because of the inclusion of viscous, elastic, and plastic terms. To keep things simple and well structured, we divided the numerical simulations into three parts. The first part dealt with the viscoplastic behavior of the fluid by eliminating the elastic effects. The challenge was to examine the effectiveness and convergence behavior of our numerical solver as well as to observe the optimal value of the regularization parameter to capture the viscoplastic model more accurately. The next part was to simulate the viscoelastic effects by eliminating the viscoplastic term from the mathematical model. The simulation was performed for the flow around a cylinder to find the drag on the cylinder. Our

results show good agreement with the reference results. In the last part, the model was tested for viscous, plastic, and elastic terms by simulating it through a porous medium with the symmetric and unsymmetric arrangement of cylinders within a domain and examining the behavior of the fluid, particularly concerning the influence of Bingham numbers. As we look ahead, our future investigations will extend beyond solely increasing the Weissenberg number. We aim to encompass a broader spectrum of Bingham numbers, ranging from small to large values. By incorporating a comprehensive range of Bingham numbers alongside higher Weissenberg numbers, we anticipate gaining a more detailed understanding of how both viscoelastic and yield stress effects interact within porous media. This expanded exploration will offer valuable insights into the complex interplay between material properties and flow dynamics. This will be done by incorporating the Bingham Papanastasiou regularized model with the other viscoelastic models, such as PTT, and FENE-P, to capture the high Weissenberg number.

Bibliography

[1] ENAWT Technologies, "Drag reducing agents," 2025.

[2] M. Liu, X. Zeng, C. Ma, H. Yi, Z. Ali, X. Mou, S. Li, Y. Deng, and N. He, "Injectable hydrogels for cartilage and bone tissue engineering," *Bone Research*, vol. 5, p. 17014, 2017.

[3] National Taiwan Ocean University, Department of Food Science, "Research areas," n.d. Accessed: 2025-07-08.

[4] Atomic Rockets (Project Rho), "Body armor," n.d. Accessed: 2025-07-08.

[5] B. A. Toms, "Some observations on the flow of linear polymer solutions through straight tubes at large Reynolds numbers," 1948.

[6] A. R. Lansdown, *Lubrication and Lubricant Selection: A Practical Guide*. Tribology in Practice Series (PEP), John Wiley & Sons Ltd, 3rd ed., Nov. 2003.

[7] E. W. Merrill, "Rheology of blood," *Physiological Reviews*, vol. 49, no. 4, pp. 863–888, 1969.

[8] R. Langer and N. Peppas, "Advances in biomaterials, drug delivery, and bionanotechnology," *AIChE Journal*, vol. 49, pp. 2990 – 3006, 12 2003.

[9] J. Malda, J. Visser, F. P. Melchels, *et al.*, "25th anniversary article: Engineering hydrogels for biofabrication," *Advanced Materials*, vol. 25, no. 36, pp. 5011–5028, 2013.

[10] E. A. Balazs and J. L. Denlinger, "Viscosupplementation: A new concept in the treatment of osteoarthritis," *Journal of Rheumatology Supplement*, vol. 20, pp. 3–9, 1993.

[11] M. A. Rao, *Rheology of Fluid and Semisolid Foods: Principles and Applications*. Food Engineering Series, Springer, 2nd ed. Series ISSN: 1571-0297; e-ISSN: 2628-8095.

[12] P. Saramito, *Complex fluids, modeling and algorithms*. Springer, 2016.

[13] F. Belblidia, H. Tamaddon-Jahromi, M. Webster, and K. Walters, "Computations with viscoplastic and viscoelastoplastic fluids," *Rheologica Acta*, vol. 50, pp. 343–360, 04 2011.

[14] E. Chaparian, D. Izbassarov, F. L. B. De Vita, and O. Tammisola, "Yield-stress fluids in porous media: a comparison of viscoplastic and elastoviscoplastic flows," *Meccanica*, vol. 55, no. 2, pp. 331–342, 2020.

[15] A. Bonito and E. Burman, "A continuous interior penalty method for viscoelastic flows," *SIAM Journal on Scientific Computing*, vol. 30, no. 3, pp. 1156–1177, 2008.

[16] T. C. Papanastasiou, "Flows of materials with yield," *Journal of Rheology*, vol. 31, no. 5, pp. 385–404, 1987.

[17] E. C. Bingham, *Fluidity and Plasticity*. New York: McGraw–Hill, 1922.

[18] W. Herschel and R. Bulkley, "Konsistenzmessungen von Gummi-Benzollösungen," *Kolloid-Zeitschrift*, vol. 39, no. 4, pp. 291–300, 1926.

[19] D. Drucker and W. Prager, "Soil mechanics and plastic analysis or limit design," *Quarterly of Applied Mathematics*, vol. 10, pp. 157–165, 1952.

[20] R. Larson, *The Structure and Rheology of Complex Fluids*. Oxford University Press, 1999.

[21] T. Schwedoff, "La rigidite des fluids, Rapports du Congrés Intern," *de Physique.*, vol. 1, pp. 478–486, 1900.

[22] J. Oldroyd, "On the formulation of rheological equations of state," *Proceedings of the Royal Society of London. Series A. Mathematical and Physical Sciences*, vol. 200, no. 1063, pp. 523–541, 1950.

[23] P. Saramito, "A new constitutive equation for elastoviscoplastic fluid flows," *J. Non-Newtonian Fluid Mech*, vol. 145(1), pp. 1–14, 2007.

[24] E. Bingham, "Fluidity and plasticity," *Bulletin of the Bureau of Standards*, vol. 19, pp. 1–79, 1922.

[25] P. R. de Souza Mendes, "Dimensionless non-Newtonian fluid mechanics," *Journal of Non-Newtonian Fluid Mechanics*, vol. 147, no. 1, pp. 109–116, 2007.

[26] S. Bénito, C. H. Bruneau, T. Colin, C. Gay, and F. Molino, "An elasto-visco-plastic model for immortal foams or emulsions," *The European Physical Journal E*, vol. 25, p. 225–251, Mar. 2008.

[27] Y. Park and P. Liu, "Oscillatory pipe flows of a yield-stress fluid," *Journal of Fluid Mechanics*, vol. 658, pp. 211–228, Sept. 2010.

[28] M. Bercovier and M. Engelman, "A finite-element method for incompressible non-Newtonian flows," *Journal of Computational Physics*, vol. 36, no. 3, pp. 313–326, 1980.

[29] D. Fraggedakis, Y. Dimakopoulos, and J. Tsamopoulos, "Yielding the yield stress analysis: A thorough comparison of recently proposed elasto-visco-plastic (EVP) fluid models," *Journal of Non-Newtonian Fluid Mechanics*, vol. 285, p. 104385, 2020.

[30] D. D. Joseph, *Fluid Dynamics of Viscoelastic Liquids*, vol. 84 of *Applied Mathematical Sciences*. New York: Springer-Verlag, 1990.

[31] P. Saramito, *Complex Fluids: Modeling and Algorithms*. Cham: Springer, 2016.

[32] M. Renardy and B. Thomases, "A mathematician's perspective on the Oldroyd B model: Progress and future challenges," *Journal of Non-Newtonian Fluid Mechanics*, vol. 293, p. 104573, 05 2021.

[33] H. Jeffreys, *The Earth: Its Origin, History and Physical Constitution*. Cambridge University Press, 1929.

[34] J. Hinch and O. Harlen, "Oldroyd B, and not A?," *Journal of Non-Newtonian Fluid Mechanics*, vol. 299, p. 104668, 2021.

[35] K. Weissenberg, "A continuum theory of rhelogical phenomena," *Nature*, vol. 159, pp. 310–311, Mar 1947.

[36] S. De, J. Kuipers, E. Peters, and J. Padding, "Viscoelastic flow simulations in random porous media," *Journal of Non-Newtonian Fluid Mechanics*, vol. 244, pp. 64–75, 2017.

[37] R. B. Bird, R. C. Armstrong, and O. Hassager, *Dynamics of Polymeric Liquids, Volume 1: Fluid Mechanics*. Wiley, 1987.

[38] F. A. Morrison, *Understanding Rheology*. Oxford University Press, 2001.

[39] S. F. Wittschieber, *Robust Finite Element Methods for Viscoelastic Constitutive Laws in Log-Conformation Form*. Doctoral dissertation, Rheinisch-Westfälische Technische Hochschule Aachen (RWTH Aachen University), Aachen, Germany, March 2023.

[40] J. G. Oldroyd, "On the formulation of rheological equations of state," *Proceedings of the Royal Society of London. Series A*, vol. 200, pp. 523–541, 1950.

[41] N. J. Balmforth, I. A. Frigaard, and G. Ovarlez, "Yielding to stress: Recent developments in viscoplastic fluid mechanics," *Annual Review of Fluid Mechanics*, vol. 46, pp. 121–146, 2014.

[42] I. A. Frigaard and C. Nouar, "On the usage of viscosity regularization methods for visco-plastic fluid flow computation," *Journal of Non-Newtonian Fluid Mechanics*, vol. 127, pp. 1–26, 2005.

[43] P. Coussot, *Yield Stress Fluid Flows: A Review of Experimental Data*. Springer, 2014.

[44] A. Syrakos, G. C. Georgiou, and A. A. Alexandrou, "Theoretical and numerical analysis of the Papanastasiou regularisation for Bingham plastic flows," *Journal of Non-Newtonian Fluid Mechanics*, vol. 261, pp. 104–119, 2018.

[45] G. R. Burgos, A. N. Alexandrou, and V. Entov, "On the determination of yield surfaces in Herschel–Bulkley fluids," *Journal of Rheology*, vol. 43, pp. 463–483, 05 1999.

[46] J. Tsamopoulos, M. Chen, and A. Borkar, "On the spin coating of viscoplastic fluids," *Rheologica Acta*, vol. 35, pp. 597–615, 11 1996.

[47] P. Saramito, "A new constitutive equation for elastoviscoplastic fluid flows," *Journal of Non-Newtonian Fluid Mechanics*, vol. 145, no. 1, pp. 1–14, 2007.

[48] R. J. Gordon and W. R. Schowalter, "Anisotropic fluid theory: A different approach to the dumbbell theory of dilute polymer solutions," *Transactions of The Society of Rheology*, vol. 16, pp. 79–97, 03 1972.

[49] E. D. Martynova, "Lagrangian representation of the family of Gordon–Schowalter objective derivatives at simple shear," *Moscow University Mechanics Bulletin*, vol. 75, no. 6, pp. 176–179, 2020.

[50] P. Saramito, "A new elastoviscoplastic model based on the Herschel–Bulkley viscoplastic model," *Journal of non-Newtonian Fluid Mechanics*, vol. 158, no. 1, pp. 154–161, 2009.

[51] J. Donea and A. Huerta, *Finite Element Methods for Flow Problems*. Wiley, 2003.

[52] W. Doherty, *Finite Element Methods for Viscoelastic Multiphase Flows Using a Conservative Level Set Approach*. Ph.D. thesis, School of Engineering, Cardiff University, Cardiff, United Kingdom, October 2024.

[53] A. Brooks and T. Hughes, "Streamline upwind/Petrov-Galerkin formulations for convection dominated flows with particular emphasis on the incompressible Navier-Stokes equations," *Computer Methods in Applied Mechanics and Engineering*, vol. 32, no. 1-3, pp. 199–259, 1982.

[54] E. Castillo and R. Codina, "Finite element approximation of the viscoelastic flow problem: A non-residual based stabilized formulation," *Computers Fluids*, vol. 142, 07 2016.

[55] R. Fattal and R. Kupferman, "Constitutive laws for the matrix-logarithm of the conformation tensor," *Journal of Non-Newtonian Fluid Mechanics*, vol. 123, no. 2-3, pp. 281–285, 2004.

[56] J. W. Barrett and S. Boyaval, "Existence and approximation of a (regularized) Oldroyd-B model," *Mathematical Models and Methods in Applied Sciences*, vol. 21, no. 9, pp. 1783–1837, 2011.

[57] S. Boyaval, T. Lelièvre, and C. Mangoubi, "Free-energy-dissipative schemes for the Oldroyd-B model," *ESAIM: Mathematical Modelling and Numerical Analysis*, vol. 43, no. 3, pp. 523–561, 2009.

[58] H. Damanik, J. Hron, A. Ouazzi, and S. Turek, "Monolithic Newton-multigrid solution techniques for incompressible nonlinear flow models," *International Journal for Numerical Methods in Fluids*, vol. 71, no. 2, pp. 208–222, 2013.

[59] J. Bonvin, M. Picasso, and R. Stenberg, "GLS and EVSS methods for a three-field Stokes problem arising from viscoelastic flows," *Computer Methods in Applied Mechanics and Engineering*, vol. 190, no. 29, pp. 3893–3914, 2001.

[60] V. Girault and P. A. Raviart, *Finite element methods for Navier-Stokes equations.* Berlin-Heidelberg: Springer, 1986.

[61] A. Bonito and E. Burman, "Edge-oriented finite element stabilization for convection-dominated flows," *Journal of Computational Mathematics*, vol. 30, no. 2, pp. 165–188, 2012.

[62] C. T. Kelley, *Iterative Methods for Linear and Nonlinear Equations.* Society for Industrial and Applied Mathematics, 1995.

[63] J. M. Ortega and W. C. Rheinboldt, *Iterative Solution of Nonlinear Equations in Several Variables.* New York: Academic Press, 1970.

[64] H. C. Elman, D. J. Silvester, and A. J. Wathen, *Finite Elements and Fast Iterative Solvers: with Applications in Incompressible Fluid Dynamics.* Oxford University Press, 2005.

[65] A. Quarteroni, *Numerical Models for Differential Problems.* Springer, 2008.

[66] R. S. Dembo, S. C. Eisenstat, and T. Steihaug, "Inexact Newton methods," *SIAM Journal on Numerical Analysis*, vol. 19, no. 2, pp. 400–408, 1982.

[67] J. M. Ortega and W. C. Rheinboldt, *Iterative Solution of Nonlinear Equations in Several Variables.* SIAM, 2000.

[68] P. H. Kelly, B. F. Smith, and D. E. Keyes, "Efficient solution techniques for fully coupled multiphysics problems with application to flow–structure interaction," *Journal of Computational Physics*, vol. 183, no. 2, pp. 420–445, 2003.

[69] H. Damanik, *FEM simulation of non-isothermal viscoelastic Fluids*. PhD thesis, TU Dortmund, Germany, 2011. PhD Thesis.

[70] T. A. Davis, "Algorithm 832: UMFPACK V4.3, an unsymmetric-pattern multifrontal method," *ACM Transactions on Mathematical Software (TOMS)*, vol. 30, no. 2, pp. 196–199, 2004.

[71] W. Hackbusch, *Iterative Solution of Large Sparse Systems of Equations*. Springer Cham, 2 ed., 2016.

[72] M. Schäfer and S. Turek, "Benchmark computations of laminar flow around a cylinder," in *Flow Simulation with High-Performance Computers II*, pp. 547–566, Springer, 1996.

[73] H. Damanik, J. Hron, A. Ouazzi, and S. Turek, "Monolithic Newton multigrid solution techniques for incompressible nonlinear flow models," *Computers & Fluids*, vol. 59, pp. 110–125, 2012.

[74] N. B. A. Ouazzi and S. Turek, "Newton-multigrid FEM solver for the simulation of quasi-Newtonian modeling of thixotropic flows," in *WCCM-ECCOMAS2020*, vol. 700 of *Numerical Methods and Algorithms in Science and Engineering*, Scipedia, 2021.

[75] A. Aposporidis, E. Haber, M. A. Olshanskii, and A. Veneziani, "A mixed formulation of the Bingham fluid flow problem: Analysis and numerical solution," *Computer Methods in Applied Mechanics and Engineering*, vol. 200, no. 29, pp. 2434–2446, 2011.

[76] A. Fatima, S. Turek, A. Ouazzi, and M. A. Afaq, "An adaptive discrete Newton method for regularization-free Bingham model," 07 2021.

[77] G. C. G. Raja R. Huilgol, *Fluid Mechanics of Viscoplasticity*. Springer Cham, 15 April 2022.

[78] O. M. Coronado, D. Arora, M. Behr, and M. Pasquali, "A simple method for simulating general viscoelastic fluid flows with an alternate log-conformation formulation," *Journal of Non-Newtonian Fluid Mechanics*, vol. 147, no. 3, pp. 189–199, 2007.

[79] H. Damanik, J. Hron, A. Ouazzi, and S. Turek, "A monolithic FEM approach for the log-conformation reformulation (LCR) of viscoelastic flow problems," *Journal of Non-Newtonian Fluid Mechanics*, vol. 165, no. 19, pp. 1105–1113, 2010.

[80] S. Wittschieber, L. Demkowicz, and M. Behr, "Stabilized finite element methods for a fully-implicit logarithmic reformulation of the Oldroyd-B constitutive law," *Journal of Non-Newtonian Fluid Mechanics*, vol. 306, p. 104838, 2022.

[81] Z. Heinemann and G. Mittermeir, *Fluid Flow in Porous Media*. PHDG textbook series, PHDG, 2nd ed., Feb. 2013.

[82] H. J. Seybold, U. Eberhard, E. Secchi, R. L. C. Cisne, J. Jiménez-Martínez, R. F. S. Andrade, A. D. Araújo, M. Holzner, and J. Andrade, "Localization in flow of non-Newtonian fluids through disordered porous media," *Frontiers in Physics*, vol. 9, 2021.

[83] F. De Vita, M. Rosti, D. Izbassarov, L. Duffo, O. Tammisola, S. Hormozi, and L. Brandt, "Elastoviscoplastic flows in porous media," *Journal of Non-Newtonian Fluid Mechanics*, vol. 258, pp. 10–21, 2018.

[84] F. Durst, R. Haas, and W. Interthal, "The nature of flows through porous media," *Journal of Non-Newtonian Fluid Mechanics*, vol. 22, no. 2, pp. 169–189, 1987.

[85] I. F. Macdonald, M. S. El-Sayed, K. Mow, and F. A. L. Dullien, "Flow through porous media-the Ergun equation revisited," *Industrial & Engineering Chemistry Fundamentals*, vol. 18, no. 3, pp. 199–208, 1979.

[86] T. Sochi, "Non-Newtonian flow in porous media," *Polymer*, vol. 51, no. 22, pp. 5007–5023, 2010.

[87] A. Verruijt, *Darcy's Law*, pp. 6–13. London: Macmillan Education UK, 1970.

[88] S. De, J. A. M. Kuipers, E. A. J. F. Peters, and J. T. Padding, "Viscoelastic flow simulations in model porous media," *Phys. Rev. Fluids*, vol. 2, p. 053303, May 2017.